

# **PERIODICA POLYTECHNICA**

## **TRANSPORTATION ENGINEERING**



PB99-129470

**TECHNICAL UNIVERSITY OF BUDAPEST**



**Vol. 25. Nos. 1-2.**  
**1997**

## PERIODICA POLYTECHNICA

A contribution to international technical sciences, published by the Technical University of Budapest  
in six separate series, covering the following sciences:

*Chemical Engineering*

*Civil Engineering*

*Electrical Engineering and Informatics*

*Mechanical Engineering*

*Social and Management Sciences (Earlier: Humanities and Social Sciences)*

*Transportation Engineering*

UNIVERSITY LEADERS:

**Á. DETREKÖI**, Rector Magnificus

**J. GINSZTLER**, Vice Rector for International Relations

**GY. HORVAI**, Vice Rector for Research Activities

**F. VÖRÖS**, Vice Rector for Education

**B. PETRÓ**, Dean of the Faculty of Architecture

**M. KUBINYI**, Dean of the Faculty of Chemical Engineering

**GY. FARKAS**, Dean of the Faculty of Civil Engineering

**J. KÖVESI**, Dean of the Faculty of Economic and Social Sciences

**L. PAP**, Dean of the Faculty of Electrical Engineering and Informatics

**K. MOLNÁR**, Dean of the Faculty of Mechanical Engineering

**T. KESZTHELYI**, Dean of the Faculty of Natural Sciences

**É. KÖVES-GILICZE**, Dean of the Faculty of Transportation Engineering

GENERAL EDITOR OF PERIODICA POLYTECHNICA:

**F. WETTL**

Technical editor of Periodica Polytechnica:

**M. Tarján-Fábry**

## TRANSPORTATION ENGINEERING SERIES

Published twice a year

SCIENTIFIC ADVISORY BOARD OF THE FACULTY OF TRANSPORTATION ENGINEERING

Chairman: **J. ROHÁCS**, Vice Dean for Scientific Research

Members: **Mrs. KÖVES É. GILICZE, J. BOKOR, J. MÁRIALIGETI,**  
**A. PRISTYÁK, J. TAKÁCS**

EXECUTIVE EDITORIAL BOARD:

Head: **J. MÁRIALIGETI**

Members: **L. KATKÓ, L. NARDAI, K. RÁCZ, E. ZIBOLEN**

Contributions in transportation engineering should be sent to the address of the journal:

TECHNICAL UNIVERSITY OF BUDAPEST

Periodica Polytechnica

Transportation Engineering

H-1521 Budapest, HUNGARY

Telefax: + 36 1 463-3041

For subscriptions please contact "Andreas Hess" Ltd. (Mail: P.O.B. 290, Budapest III, H-1300;  
Telefax: +36 1 250-2188) or its representatives abroad.

Exchange copies should be requested from the International Exchange Department of the Central  
Library of the Technical University of Budapest  
(H-1111 Budapest, Budafoki út 4.; Telefax: + 36 1 463-2440).

Published by the Technical University of Budapest, Hungary, with the financial help of the foundation  
"Ipar a korszerű mérnökképzésért" (Industry for Modern Education in Engineering) and  
"Ipar Műszaki Fejlesztésért" (Foundation for Industry).

# **PERIODICA POLYTECHNICA**

TRANSPORTATION ENGINEERING

Vol. 25 \* Nos. 1-2 \* 1997

TECHNICAL UNIVERSITY  
BUDAPEST

PRINTED IN HUNGARY  
LIGATURA LTD - ÁFÉSZ PRESS, VÁC

## TRACK-VEHICLE IN-PLANE DYNAMICAL MODEL CONSISTING OF A BEAM AND LUMPED PARAMETER COMPONENTS

István ZOBORY and Vilmos ZOLLER

Department of Railway Vehicles  
Technical University of Budapest  
H-1521 Budapest, Hungary

### Abstract

This paper deals with the exact mathematical description of a simple in-plane track-vehicle dynamical system model. The railway track is modelled by a beam on damped linear foundation, while the two-axle railway vehicle is modelled by a lumped parameter linear dynamical system. The interaction between the track and the vehicle in vertical plane is described by the Hertzian spring and damper, belonging to the linearized vertical contact force transfer. Formulation of the mathematical models, as well as the closed form solutions for the excitation-free system are presented.

*Keywords:* track/vehicle dynamical system, hybrid systems of differential equations.

### 1. The Track-Vehicle System Model

The system model is shown in *Fig. 1*. The in-plane dynamical model is a typical *hybrid* one, as it consists of a continuum subsystem, i.e. the track, treated as an Euler-Bernoulli beam on damped Winkler foundation, and a lumped parameter vehicle subsystem describing the two-axle railway vehicle. The connection of the two subsystems mentioned is realized by the contact springs/dampers.

The track model parameters are the following: rail density  $\rho$ , cross section area of the two rails  $A$ , moment of inertia of the two rails  $I$ , Young modulus of the rail  $E$ , foundation stiffness  $s$  and foundation damping  $k$ . The vertical position of the rails is described by bivariate function  $z(x, t)$ , the so called rail deflection function. Here  $x$  stands for the longitudinal coordinate of the track.

The vehicle parameters are as follows: wheelset masses  $m_1$  and  $m_2$ , carbody mass  $m$ , carbody moment of inertia  $\Theta$ , vertical wheelset suspension stiffnesses  $s_1$  and  $s_2$ , vertical wheelset suspension dampings  $k_1$  and  $k_2$ , axlebase  $L = l_1 + l_2$ , coefficient  $a$  of the velocity-square dependent air drag and the vertical distance  $h$  between the action line of the air drag and the mass centre of the carbody. There are four free coordinates describing the positions of the masses in the vehicle subsystem: vertical displacement of

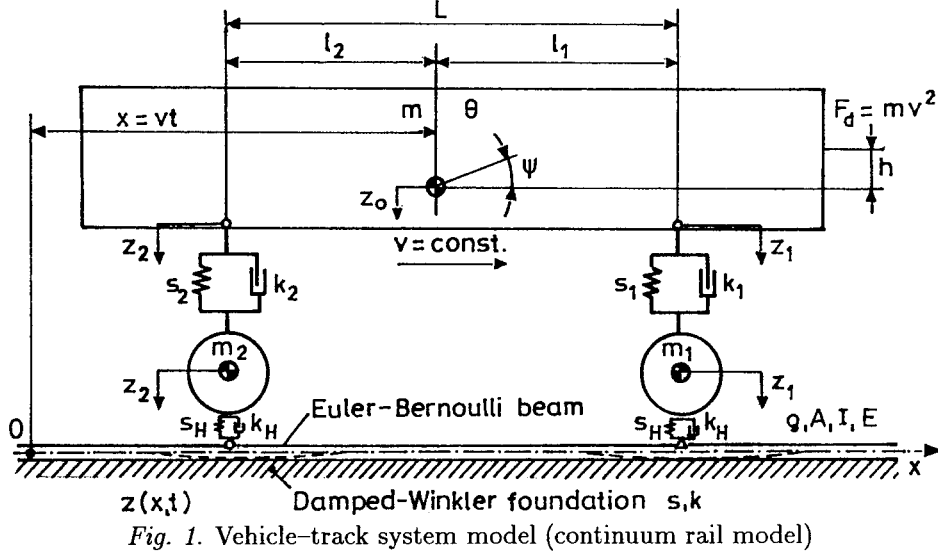


Fig. 1. Vehicle-track system model (continuum rail model)

the carbody  $z_0$ , angular displacement of the carbody  $\psi$ , and vertical displacements of the wheelsets  $Z_1$  and  $Z_2$ . Two further vertical displacements are important on the carbody to determine the motion-state dependent vertical forces transmitted through the suspension springs and dampers. The points on the carbody located over the wheelsets are indicated in Fig. 1 and their displacements can be expressed by using  $z_0$  and  $\psi$  in the following way:  $z_1 = z_0 - l_1\psi$  and  $z_2 = z_0 + l_2\psi$ .

The interaction of the track and the vehicle is realized through the Hertzian springs and dampers of linearized stiffness  $s_H$  and damping factor  $k_H$ . The actual operation condition of the vehicle is reflected in the constant velocity  $v$  of the carbody mass centre. The longitudinal position of the latter under this condition is given by product  $vt$ . So, the longitudinal coordinates of the wheelset/track contact points are  $x_1 = vt + l_1$  and  $x_2 = vt - l_2$ .

Thus, the track-vehicle dynamical system can be characterized by parameter vector  $\mathbf{p}$  of dimension 21. Its form is

$$\mathbf{p} = [\rho, A, I, E, s, k; l_1, l_2, h, m_1, m_2, m, \Theta, s_1, s_2, k_1, k_2, a; s_H, k_H; v]^T.$$

The motion conditions can be studied by seeking for the function  $z(x, t)$  of the track deflection, and the free coordinates  $z_0(t)$ ,  $\psi(t)$ ,  $Z_1(t)$  and  $Z_2(t)$  characterizing the vehicle subsystem. The governing set of motion equations are established in the next chapter.

## 2. Mathematical Description of the System Model

The equations of motion are determined by using Newton's 2nd law for the rigid body components of the vehicle subsystem, and the known equation of the Euler-Bernoulli beam on elastic/damped foundation in the presence of forces describing the vertical interaction between the track and the wheels. The equations of motion of the wheelsets are the following:

$$F_i(\ddot{Z}_i, \dot{Z}_i, Z_i, \dot{z}_i, z_i) = s_i(z_i - Z_i) + k_i(\dot{z}_i - \dot{Z}_i) + m_i g - m_i \ddot{Z}_i = s_H(Z_i - z(vt + L_i, t)) + k_H(\dot{Z}_i - \frac{d}{dt}z(vt + L_i, t)), \quad i = 1, 2, \quad (1)$$

where  $L_i = (-1)^{i+1}l_i$ ,  $i = 1, 2$  stand for oriented lengths.

The vertical translatory motion of the carbody is governed by the following equation:

$$\sum_{i=1}^2 [-s_i(z_i - Z_i) - k_i(\dot{z}_i - \dot{Z}_i)] + mg - m \ddot{z}_0 = 0. \quad (2)$$

The pitching motion equation has the following form:

$$\sum_{i=1}^2 [s_i(z_i - Z_i) + k_i(\dot{z}_i - \dot{Z}_i)]L_i + hav^2 - \Theta \ddot{\psi} = 0. \quad (3)$$

The track deflection is described by the following fourth order linear partial differential equation:

$$IE \frac{\partial^4 z}{\partial x^4} + \rho A \frac{\partial^2 z}{\partial t^2} + k \frac{\partial z}{\partial t} + sz = \sum_{i=1}^2 \delta(x - (vt + L_i)) F_i(\ddot{Z}_i, \dot{Z}_i, Z_i, \dot{z}_i, z_i). \quad (4)$$

Together with Eqs. (1-4) also relationships

$$z_0 = z_1 + l_1 \psi = z_2 - l_2 \psi \quad (5)$$

are in force.

We are able to eliminate  $z_0$  and  $\psi$  from Eqs. (2-3) by expressing

$$\psi = \frac{z_2 - z_1}{L} \text{ and } z_0 = \frac{l_1 z_2 + l_2 z_1}{L}.$$

This way our original system can be simplified from the point of view of the mathematical treatment as follows.

Let us introduce functions

$$g_i(t) = F_i(\ddot{Z}_i(t), \dot{Z}_i(t), Z_i(t), \dot{z}_i(t), z_i(t)) + m_i(\ddot{Z}_i - g)$$

for  $i = 1, 2$ .

Then our differential equations can be written into the form

$$IE \frac{\partial^4 z}{\partial x^4} + \rho A \frac{\partial^2 z}{\partial t^2} + k \frac{\partial z}{\partial t} + sz = \sum_{i=1}^2 \delta(x - (vt + L_i))(g_i(t) - m_i(\ddot{Z}_i - g)), \quad (6)$$

$$g_i(t) = \sum_{j=1}^2 a_{ij} \ddot{z}_j + b_i = s_i(z_i - Z_i) + k_i(\dot{z}_i - \dot{Z}_i) =$$

$$s_H(Z_i - z(vt + L_i, t)) + k_H(\dot{Z}_i - \frac{d}{dt}z(vt + L_i, t)) + m_i(\ddot{Z}_i - g) \quad (7)$$

for  $i = 1, 2$  with

$$a_{ij} = \frac{(-1)^{i+j+1}}{L^2} \left( \frac{mL_1^2 L_2^2}{L_i L_j} + \Theta \right), \quad b_i = \frac{(-1)^i}{L} \left( \frac{mL_1 L_2 g}{L_1} + hav^2 \right).$$

The solution has to satisfy boundary condition

$$\lim_{x \rightarrow \pm\infty} z(x, t) = 0 \quad (8)$$

and initial conditions

$$z_i(0) = z_{i0}, \quad \dot{z}_i(0) = v_{i0}, \quad Z_i(0) = Z_{i0}, \quad \dot{Z}_i(0) = V_{i0} \quad (9)$$

for  $i = 1, 2$ .

### 3. Solution to the Boundary Value Problem

We are looking for the solution  $[z, z_1, z_2, Z_1, Z_2]^T$  of system (6–9) in the form

$$z(x, t) = \sum_{k=0}^8 A_k(\xi) e^{w_k t},$$

$$z_i(t) = \sum_{k=0}^8 \xi_{ik} e^{w_k t}, \quad Z_i(t) = \sum_{k=0}^8 \zeta_{ik} e^{w_k t}, \quad i = 1, 2,$$

where  $\xi = x - vt$ ,  $w_0 = 0$ , while the  $w_k$ 's for  $k = 1, 2, \dots, 8$  are the *complex frequencies* of the system and  $\xi_{ik}$ ,  $\zeta_{ik}$  are appropriate constants, all of them are to be determined later on.

Substituting our expected solution into the right-hand side of Eq. (6), the partial differential equation will have the form

$$IE \frac{\partial^4 z}{\partial x^4} + \rho A \frac{\partial^2 z}{\partial t^2} + k \frac{\partial z}{\partial t} + sz = \sum_{i=1}^2 \sum_{k=0}^8 \delta(\xi - L_i) c_{ik} e^{w_k t}$$



with  $c_{i0} = b_i + m_i g$  and

$$c_{ik} = \left( \sum_{j=1}^2 a_{ij} \xi_{jk} - m_i \zeta_{ik} \right) w_k^2 \text{ for } k = 1, 2, \dots, 8. \quad (10)$$

Then applying the theory of such partial differential equations [1–5], we can use formulae of [7] to compute  $A_k(\xi)$  as

$$A_k(\xi) = \sum_{i=1}^2 c_{ik} B(\xi - L_i, w_k),$$

$$B(\eta, w) = H(\eta) \left( \frac{e^{\lambda_1 \eta}}{P'(\lambda_1)} + \frac{e^{\lambda_2 \eta}}{P'(\lambda_2)} \right) - H(-\eta) \left( \frac{e^{\lambda_3 \eta}}{P'(\lambda_3)} + \frac{e^{\lambda_4 \eta}}{P'(\lambda_4)} \right),$$

where the characteristic polynomial

$$P(\lambda) = IE\lambda^4 + \rho A v^2 \lambda^2 - v(k + 2\rho A w)\lambda + (s + kw + \rho A w^2)$$

has neither imaginary nor multiple roots (necessary and sufficient conditions are given in [7]),  $\lambda_1$  and  $\lambda_2$  are the roots of polynomial  $P$  with negative real parts,  $P'$  is the derivative of  $P$ , while  $H$  is Heaviside's unit jump function. (The formula for the multiple root case is given in [7].)

#### 4. Determination of Complex Frequencies

Substituting the expected solutions into *Eqs. (7)*, by comparing coefficients we obtain the system of equations

$$s_H(\xi_{i0} - A_0(L_i)) - m_i g = s_i(\xi_{i0} - \zeta_{i0}) = b_i, \quad (11)$$

$$w_k^2 \sum_{j=1}^2 a_{ij} \xi_{jk} = (s_i + k_i w_k)(\xi_{ik} - \zeta_{ik}) = (s_H + k_H w_k)(\xi_{ik} - A_k(L_i)) + m_i w_k^2 \zeta_{ik} \quad (12)$$

for  $i = 1, 2$  and  $k = 1, 2, \dots, 8$ . System (12) contains unknowns  $w_k$ ,  $\xi_{ik}$  and  $\zeta_{ik}$ . In order to obtain the complex frequencies  $w_k$ ,  $k = 1, 2, \dots, 8$  the latter unknowns can be eliminated. This procedure results in nonlinear equation

$$\det(\mathbf{C}(w)) = 0, \quad (13)$$

where  $\mathbf{C}(w)$  is a  $w$ -dependent  $2 \times 2$  matrix with entries

$$c_{ij}(w) = a_{ij} w^2 - (s_H + k_H w) \left\{ \delta_{ij} - \frac{w^2 a_{ij}}{s_i + k_i w} + \right.$$

$$\sum_{n=1}^2 \left( -a_{nj} + m_n \delta_{nj} - \frac{m_n w^2 a_{nj}}{s_n + k_n w} \right) w^2 B(L_i - L_n, w) \Big\} - m_i w^2 \delta_{ij} + \frac{m_i w^4 a_{ij}}{s_i + k_i w}.$$

In the above expression  $\delta_{ij}$  stands for Kronecker's symbol. The solutions  $w_1, w_2, \dots, w_8$  are the complex frequencies of system (6–9). With the knowledge of these frequencies  $w_k$  one can easily determine constants  $\xi_{ik}$  and  $\zeta_{ik}$  by solving linear equation system (11–12) together with initial conditions (9).

## 5. Conclusions

In this paper a new mathematical treatment has been elaborated for the solution of a set of equations describing the joint problem of the combined motions of the continuous track and the vehicle modelled as a lumped parameter system. The wheelsets of the vehicle are moving at a constant longitudinal velocity on the elastically/dissipatively supported beam at a constant longitudinal velocity. The two subsystems, connected with each other by the Hertzian springs/dampers, are completely characterized through the closed-form expressions based on the complex frequencies obtained from the solution of the auxiliary nonlinear equation.

## References

- [1] BOGACZ, R. – KRZYŹIŃSKI, T. – POPP, K.: On the Generalization of Mathews' Problem of the Vibrations of a Beam on Elastic Foundation, *ZAMM*, Vol. 69, pp. 243–252 (1989).
- [2] DE PATER, A. D.: Inleidend onderzoek naar het dynamisch gedrag van spoorstaven, Thesis, Waltman, Delft, 1948.
- [3] FILIPPOV, A. P.: Vibrations of Deformable Systems (in Russian), Mashinostroenie, Moscow, 1970.
- [4] KENNEY, J. T.: Steady-State Vibrations of Beam on Elastic Foundation for Moving Load, *J. Appl. Mech.*, Vol. 21, pp. 359–364 (1954).
- [5] MATHEWS, P. M.: Vibrations of a Beam on Elastic Foundation I–II, *ZAMM*, Vol. 38, pp. 105–115 (1958), Vol. 39, pp. 13–19 (1959).
- [6] ZOBORY, I.: The Track-Vehicle System from the Point of View of the Vehicle Engineer, *4th International Conference on the Track-Vehicle System* (in Hungarian), Velem, pp. 19–41 (1991).
- [7] ZOBORY, I. – ZOLLER, V. – ZIBOLEN, E.: Theoretical Investigations into the Dynamical Properties of Railway Tracks Using a Continuous Beam Model on Elastic Foundation, *Periodica Polytechnica, Ser. Transp. Eng.*, Vol. 22, pp. 35–54 (1994).

## AN INVERTED PENDULUM TOOL FOR TEACHING LINEAR OPTIMAL AND MODEL BASED CONTROL

Alexandros SOUMELIDIS\*, Péter GÁSPÁR\*\* and József BOKOR\*\*

\*Computer and Automation Research Institute  
Hungarian Academy of Sciences  
H-1111 Budapest, Kende u. 13-17, Hungary  
Fax: +36 1 166-7503  
Phone: +36 1 366-7483

\*\* Department of Control and Transport Automation  
Technical University of Budapest  
H-1521 Budapest, Hungary  
Fax: +36 1 463-3087  
Phone: + 36 1 463-1013

### Abstract

The use of the inverted pendulum experiment in teaching control theory and practice is now widely accepted in the area of control education. This paper describes an environment built upon an operating inverted pendulum suitable to design and test several linear controllers by using the well known MATLAB and its toolboxes. The environment has been designed to maximally fit to MATLAB procedures and interfaces. A significant part of the environment is a support for identification and model based control, which provides a MATLAB compatible mode to acquire data of the relevant variables and to generate disturbances with predesigned characteristics. Some didactic examples – mainly from the field of model based control – are described. As the examples present, the inverted pendulum experiment is suitable to use it in teaching – beyond the conventional ones – the more contemporary topics of the control science.

*Keywords:* education, optimal control, linear identification.

### 1. Introduction

Teaching control theory and practice has got great significance in the recent years in several areas of the undergraduate and graduate level technical education. For many years the researchers of the System and Control Laboratory of the Computer and Automation Research Institute are involved in teaching control science within the educational program of the Department of Control and Transport Automation of the Technical University of Budapest. As the background which the transportation engineering students possess differs from that of e.g. control engineering students, a significant point in teaching control science must be the good interpretation of theoretical results. Computer simulations are not sufficient, really operating

devices are preferable for the purpose of understanding the objectives, requirements, means and methods of control actions. Therefore the attention has been oriented to some real experiments which represent the control actions in descriptive enough manner. The inverted pendulum experiment has found to be optimal for the purposes stated:

- The effect of the control actions is obvious – without control, the rod of the inverted pendulum falls down.
- As being a basically mechanical system, it fits to the way of thinking of students of mechanical or transportation engineering.
- The structure of the inverted pendulum device is quite simple, it can easily be modeled – by applying the most fundamental rules of physics.
- The quality requirements to set up for the controlled system can easily be expressed on the basis of common sense considerations, e.g. small deviations of the rod, fast return to the original position at a disturbance, indifference to disturbances, etc.

The System and Control Laboratory in collaboration with the Department of Control and Transport Automation of the Technical University of Budapest has built multiple inverted pendulum devices for classroom usage. The main design criterion has been the simplicity, therefore moving the cart has been solved with a DC servo motor driven by a power amplifier, cart position and rod angle measurements have been implemented by using potmeters (see Fig. 1), i.e. the inverted pendulum is totally analog device. Direct digital control can be realized by means of a computer complemented with analog to digital and digital to analog converters. IBM compatible personal computers can be used based upon Intel processors, preferably 486 or Pentium ones. Several types of AD/DA cards can be used including e.g. data acquisition products of National Instruments.

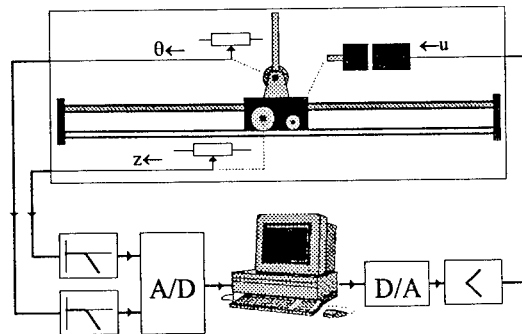


Fig. 1. Schematic diagram of inverted pendulum

The control program – it can be considered as a control environment – has been developed by the Systems and Control Laboratory. It has been written on the basis of LabWindows/CVI for Windows<sup>TM</sup> environment,

product of the National Instruments (Austin, TX), which has provided excellent user interface and means of graphical representation.

The control environment will be described in the Section 2. Then a brief outline of the modeling issues and the design of a nominal controller will be given Section 3. Section 4 contains some didactic examples from the field of the model based control design, providing evidence for the strength of the system realized.

## 2. The Control Environment

The inverted pendulum control environment developed by the authors has been realized as a Microsoft Windows<sup>TM</sup> application. The program assumes some type of AD/DA card – several installable versions are available for different platforms.

The control environment represents not only a control algorithm, but consists of several features which supports a higher level control design such as iterative identification based design schemes.

The basic features of the environment are enumerated as follows.

The control environment provides a discrete real-time direct control facility with configurable timing characteristics. The control algorithm can be downloaded to the environment. The downloadable form is a MATLAB compatible file (namely MAT), which contains the state-space form of any discrete linear controller, i.e. a series of four matrices,  $A_{n \times n}$ ,  $B_{n \times n}$ ,  $C_{2 \times n}$  and  $D_{2 \times 1}$ , respectively, where  $n$  is a user selectable order of the controller. This form enables the user to design any linear controller he/she wants, including optimal and robust controllers.

In regular undergraduate education the principles and methods of the classical control theory are applied, hence the method of pole-placement and simplified optimal LQ design has been introduced as laboratory experiments. In these schemes the connection between the performance properties of the designed closed loop system and the methods or design parameters (values of weighting factors, location of poles, etc.) can be indirectly observable. At graduate level courses the linear quadratic and Gaussian (LQG) controller design, the Kalman filtering based observer design (ANDERSON & MOORE, 1989). The higher level courses can deal with the model based control design, which encloses the identification of the structure and of the model parameters, as well as the estimation of the plant uncertainties. In this way students can comprehend the fundamental principles of the robust (postmodern) control theory (MACIEJOWSKY, 1989). Later in this paper some examples for model based control design from the graduate course will be illustrated.

Besides the real-time control the environment contains an inverted pendulum simulator which is aimed to serve as a preliminary test of the new

algorithms to avoid damages of the hardware. There is a built-in nonlinear simulator as well as possibility to download any type of linear simulator of MATLAB form.

The control environment offers a menu-driven mode to configure the system for a given inverted pendulum hardware, to test and calibrate the configuration, as well as gives possibility to look graphically the time-functions of the significant system variables in history-like manner with configurable extent. A sample screen of the environment with an operating simulation can be seen in *Fig. 2*.

Beyond the basic ones the control environment provides several advanced features, these are outlined as follows.

The control environment support identification and iterative control design schemes. There are two built-in facilities to support them: data acquisition on the most significant system variables and application of disturbances on them.

Data acquisition is based upon the history mentioned above. The user has the possibility to store a selected part of the history (of course after a successful operation of the inverted pendulum control) in a MATLAB compatible form. These records can be used in any identification procedure implemented in MATLAB.

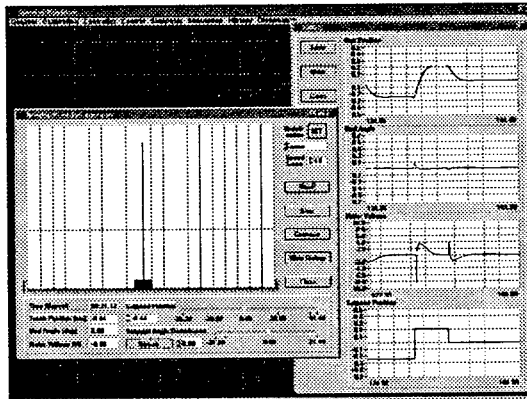


*Fig. 2.* A sample screen of the environment

The disturbance facility is also based upon MATLAB. The user can design several disturbances (deterministic or stochastic signals, e.g. sine wave, Gaussian noise process, etc.) to be applied on system variables in additive manner. The disturbances can be downloaded to the control environment, and assign them to several system variables as well as to switch on or off depending upon the test experiment to be performed. The environment also has local capabilities to generate simple disturbances. The use of iden-

tification and disturbances will be introduced in detail in section 4 of the paper.

### 3. Modeling and Control

First step of the control design must be the construction of a nominal model of the inverted pendulum. In the stated framework this can be a linear state-space model. The starting point of the model construction can be the Newtonian laws of mechanics.

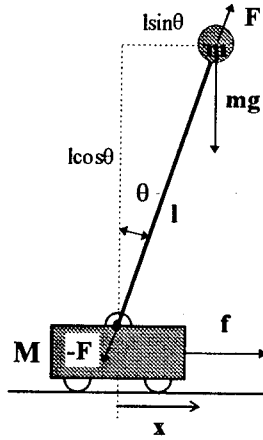


Fig. 3. Modeling the inverted pendulum

By applying them on the schematic view of system seen in Fig. 3, we obtain the nonlinear equations as follows (see for detailed derivation e.g. (OGATA, 1990)):

$$\begin{aligned} (M + m)\ddot{x} - ml\dot{\theta}^2 \sin \theta + ml\ddot{\theta} \cos \theta &= f, \\ m\ddot{x} \cos \theta + ml\ddot{\theta} &= mg \sin \theta. \end{aligned}$$

After applying  $\sin \theta \cong \theta$ ,  $\cos \theta \cong 1$  for small angles and  $\dot{\theta}^2 \cong 0$  for the uppermost position of the mass  $m$ , we obtain linear differential equations, which with the  $x_1 = x$ ,  $x_2 = \dot{x}$ ,  $x_3 = \vartheta$ ,  $x_4 = \dot{\vartheta}$  selection of the state-variables can be expressed in the state-space form as follows:

$$\begin{aligned} \dot{x}_1 &= x_2, & y_1 &= x_1, \\ \dot{x}_2 &= -\frac{m}{M}gx_3 + \frac{1}{M}f, & y_2 &= x_3, \\ \dot{x}_3 &= x_4, \\ \dot{x}_4 &= \frac{M+m}{Ml}gx_3 - \frac{1}{Ml}f. \end{aligned}$$

The input of the model is force  $f$  influencing the cart which must be substituted with the input voltage of the DC servo motor (see *Fig. 1*). A modified form of the equations can be derived by applying the torque/revolution and torque/current characteristics of the DC servo motor (see e.g. the product catalogue of MAXON motors (MAXON, 1992, p. 123)) supposed to be linear ones, as well as the mechanical relations between the rotational and linear motion. The modified state-space equations can be seen as follows:

$$\begin{bmatrix} \dot{x}_1 \\ \dot{x}_2 \\ \dot{x}_3 \\ \dot{x}_4 \end{bmatrix} = \begin{bmatrix} 0 & 1 & 0 & 0 \\ 0 & -\frac{R_m}{M} \left( \frac{K_m K_g}{R_m r} \right)^2 & -\frac{m}{M} g & 0 \\ 0 & 0 & 0 & 1 \\ 0 & -\frac{R_m}{Ml} \left( \frac{K_m K_g}{R_m r} \right)^2 & \frac{M+m}{Ml} g & 0 \end{bmatrix} \begin{bmatrix} x_1 \\ x_2 \\ x_3 \\ x_4 \end{bmatrix} + \begin{bmatrix} 0 \\ \frac{1}{M} \frac{K_m K_g}{R_m r} \\ 0 \\ -\frac{1}{Ml} \frac{K_m K_g}{R_m r} \end{bmatrix} u$$

$$\begin{bmatrix} y_1 \\ y_2 \end{bmatrix} = \begin{bmatrix} 1 & 0 & 0 & 0 \\ 0 & 0 & 1 & 0 \end{bmatrix} \begin{bmatrix} x_1 \\ x_2 \\ x_3 \\ x_4 \end{bmatrix},$$

where  $u$  is the input voltage of the DC servo,  $R_m$  is the armature resistance,  $K_m$  is the torque constant,  $K_g$  is the mechanical attenuation of the rotational motion,  $r$  is the radius of the wheel transforming the rotation into linear motion. The dynamics of the motor armature, the mechanical uncertainty of the coupled mechanical elements, as well as any friction is neglected in this simplified description.

The system represented by the model – as it can easily be shown – is unstable, however, it is controllable. A bit difficulty occurs in the control design by the fact that it is not a minimum phase system.

A nominal controller, which can be served as a starting point of applying any iterative scheme for model based control, can simply be designed on the basis of optimal linear quadratic control. As the state of the system is not fully measured a state observer must be established. The design of an optimal linear quadratic controller can be realized with the procedures of the Control Toolbox of MATLAB. The output of the MATLAB procedure is the discretized state-space form of the controller, which can directly be loaded into the inverted pendulum control environment.

The transfer characteristics of the nominal controller designed on the basis of the nominal model can be seen in *Fig. 4* (step response of the closed loop). An LQ optimal full state observer has been realized with covariance matrices with diagonal elements  $\langle 0.01, 0.1, 0.05, 0.5 \rangle$  for process noise and  $\langle 0.01, 0.01 \rangle$  for measurements noise, respectively. The weighting matrix used for LQ feedback gain computation has also been diagonal with elements  $\langle 0.25, 0.01, 4.0, 0.01 \rangle$  and input weighting has been 0.0003. The design procedure has resulted in quite good closed loop characteristics, sufficiently fast settling and small deviations around the desired state.



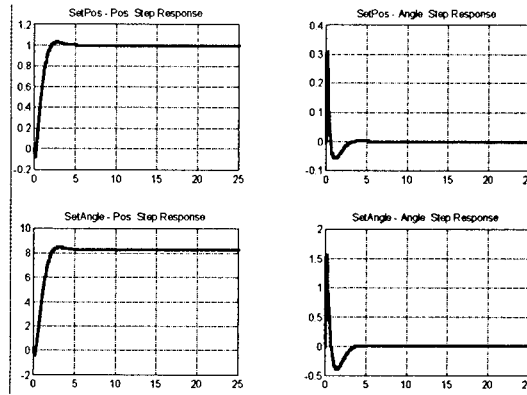


Fig. 4. Step response characteristics of control

#### 4. Didactic Examples

The inverted pendulum experiment seems to be an excellent means to illustrate and test principles and methods of the postmodern control theory, and can be served as a good basis for the use in teaching. In this section some examples will be presented – selected from the field of model based control – to illustrate the strength of this approach.

While the inverted pendulum is an unstable system so the identification has to be performed in closed loop, namely applying data collected in closed loop on the plant while an initialized and known controller operates. The closed loop identification can be performed on the one hand in classical way using direct or indirect method (SÖDERSTRÖM & STOICA, 1989) and on the other hand applying modern methods, which take the feedback connection among signals into account, e.g. two stage method, coprime factorization method or dual Youla parametrization method (VAN DEN HOF & SCHRAMA, 1994).

In Fig. 5 the magnitude and phase frequency response of two kinds of identified transfer function between the motor input voltage and the cart position are demonstrated. Figures of the left hand side show the result of the direct method, while figures of the right hand side illustrate the result of two stage method. The orders of the autoregressive and input operators are selected as 4. The solid lines show the plots of the identified model, while the dashed lines show the theoretical plots.

Although this example illustrates an identification of a single-input single-output (SISO) system in the laboratory experiments there is the possibility to investigate the identification of the multi-input multi-output (MIMO) system.

Based on the identified model a state feedback gain matrix and an estimator (or filter) gain matrix are designed, then the combined linear

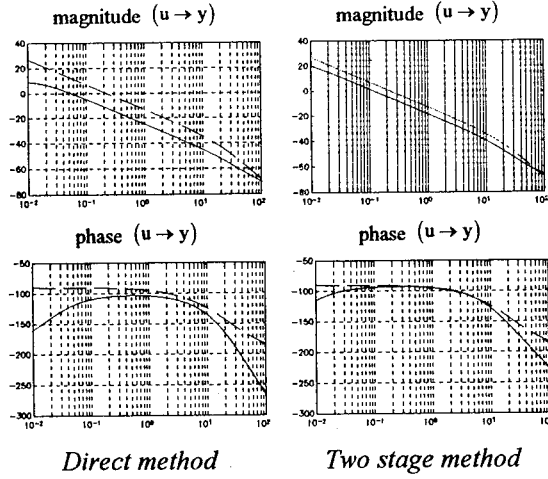


Fig. 5. Bode plots of the identified models

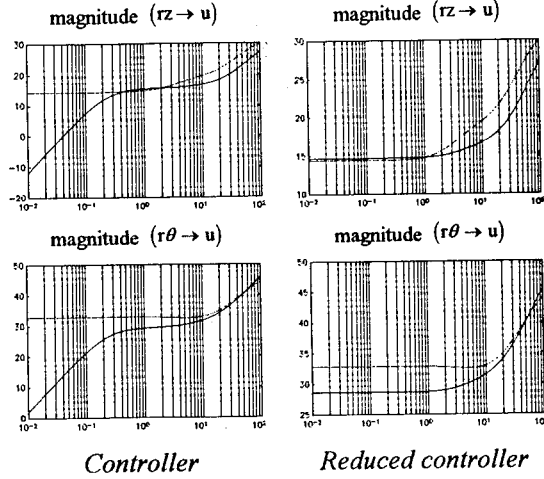


Fig. 6. Magnitude plots of the controller

quadratic and Gaussian (LQG) controller is formed. On the left hand side of Fig. 6 the solid lines represent the magnitude plots of the designed controller and the dashed lines show the plots of the optimal controller based on the theoretical model. In the laboratorial experiments there is the possibility to examine the effect of changing the weighting factors and to compare the different designed controller in the sense of performance characteristic of the closed loop system. In this example the dimension of the designed controller is 12, which can be reduced as follows.

The well known model reduction methods can be applied for controller reduction, e.g. balanced realization or minimal realization, but those meth-

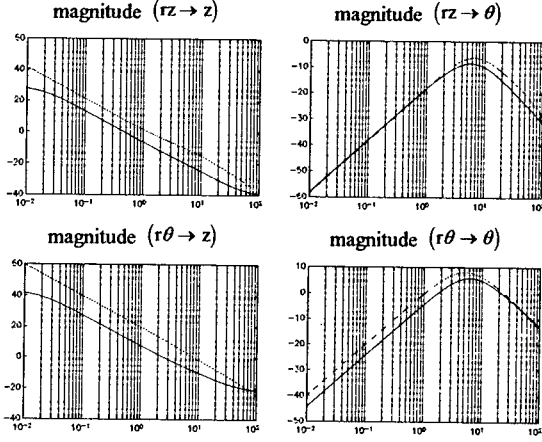


Fig. 7. Bode plots of the open loop system

ods can be also used which were developed for controller reduction purpose, e.g. closed loop balanced reduction, coprime factorization reduction, etc., (LIU & ANDERSON, 1990). These latter methods perform the dimension reduction taking the performance criterion of the closed loop into account. In this example the controller reduction has been performed by frequency weighted balanced truncation method. The order of the reduced controller is 8. The magnitude plots of the reduced controller can be found on the right hand side of Fig. 6.

The magnitude plots of the open loop can be seen in Fig. 7. The solid line represents the designed open loop based on the identified model, while the dashed line illustrates the nominal open loop. It can be seen, that the designed frequency functions are close to the nominal functions in the whole frequency domain.

The following two examples illustrate the behavior of the designed controller in the actual loop. The displacement and the angle of the pendulum measured in 30 sec time domain can be seen in Fig. 8. In this case additive extra disturbances of displacement and of the angle are not introduced to the system. In the last example a reference signal has been introduced

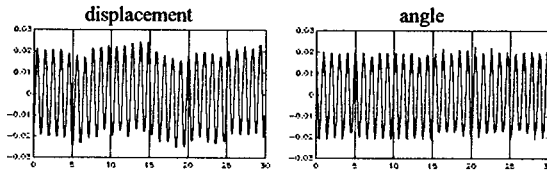


Fig. 8. Examination of LQG controller

for the displacement while the angle is disturbed by a random signal. In

Fig. 9 it can be seen that the output displacement signal slowly follows the reference signal. Of course, it is possible to investigate other solutions for reference signal tracking, e.g. the augmentation of the LQG controller by an integrator term or the solution of a proper prefilter design.

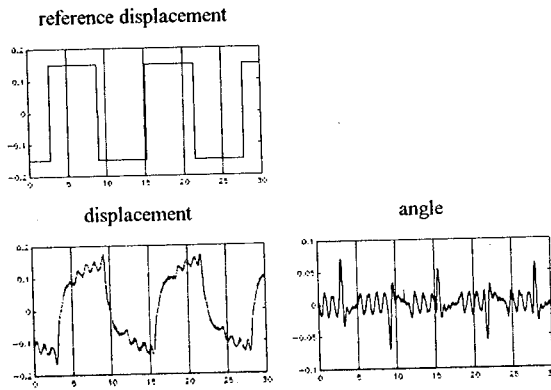


Fig. 9. Examination of reference signal tracking

## 5. Conclusion

As the didactic examples presented, the inverted pendulum experiment is suitable to use in teaching – beyond the conventional ones – the more contemporary topics of the control science, e.g. robust and model based control. Laboratory experiments are based upon MATLAB environment and its toolboxes, which are well known by most of the undergraduate and graduate students. The control environment developed by the authors results in a compact solution to the whole experiment, including hardware handling, real-time control, identification, and design of control algorithms.

## Acknowledgements

The authors would like to express their thanks to Károly Kurutz and Sándor Sárközi, Professors of the Department of Control and Transport Automation of the Technical University of Budapest, for their cooperation in producing inverted pendulum devices and introducing this field in the educational program. This project has been supported by the Hungarian National Science Foundation through grant. no. T-016418.

## References

- [1] OGATA, K. (1990): Modern Control Engineering, Prentice-Hall International, Inc., 2nd edition, pp. 104–107.
- [2] MAXON (1993): MAXON Motor Catalogue, Interelectric AG, Switzerland, Edition 1993/94, pp. 122–125.
- [3] ANDERSON, B. D. O. – MOORE, J. B. (1989): Optimal Control, Linear Quadratic Methods, Prentice Hall, Englewood Cliffs, New Jersey.
- [4] MACIEJOWSKY, X. (1989): Multivariable Feedback Design, Addison Wesley, New York.
- [5] ANDERSON, B. D. O. – LIU, Y. (1989): Controller Reduction: Concepts and Approaches, *IEEE Trans. Automatic Control*, Vol. 34, No. 8, pp. 802–812.
- [6] SÖDERSTRÖM, T. – STOICA, P. (1989): System Identification, Prentice Hall, Englewood Cliffs, New Jersey.
- [7] VAN DEN HOF, P. M. J. – SCHRAMA, R. J. P. (1994): Identification and Control – Closed Loop Issues, *Proceedings of the 10th IFAC Symposium on System Identification*, Copenhagen, pp. 1–14.



## QUASI-RECURRENT WEYL SPACES

Elif Özkara CANFES and S. Aynur UYSAL

Istanbul Technical University  
Faculty of Science and Letters  
80626 Maslak, Istanbul  
Turkey

### Abstract

In this work we define Quasi-Recurrent Weyl spaces and examine the hypersurfaces of them.

*Keywords:* Weyl spaces, Quasi-Recurrent Weyl Spaces.

### 1. Introduction

An  $n$ -dimensional manifold  $W_n$  is said to be a Weyl space if it has a conformal metric tensor  $g_{ij}$  and a symmetric connection  $\nabla_k$  satisfying the compatibility condition given by the equation

$$\nabla_k g_{ij} - 2T_k g_{ij} = 0, \quad (1)$$

where  $T_k$  denotes a covariant vector field and  $\nabla_k g_{ij}$  denotes the usual covariant derivative.

Under renormalization of the fundamental tensor of the form

$$\check{g}_{ij} = \lambda^2 g_{ij} \quad (2)$$

the complementary vector  $T_k$  is transformed by the law

$$\check{T}_i = T_i + \partial_i \ln \lambda, \quad (3)$$

where  $\lambda$  is a function.

Writing (1) out in full, we have

$$\partial_k g_{ij} - g_{hj} \Gamma_{ik}^h - g_{ih} \Gamma_{jk}^h - 2T_k g_{ij} = 0,$$

where  $\Gamma_{kl}^i$  are the connection coefficients of the form

$$\Gamma_{kl}^i = \left\{ \begin{matrix} i \\ kl \end{matrix} \right\} - g^{im} (g_{mk} T_l + g_{ml} T_k - g_{kl} T_m). \quad (4)$$

A quantity  $A$  is called a satellite with weight  $\{p\}$  of the tensor  $g_{ij}$ , if it admits a transformation of the form

$$\check{A} = \lambda^p A$$

under the renormalization (2) of the metric tensor  $g_{ij}$ .

The prolonged covariant derivative of a satellite  $A$  of the tensor  $g_{ij}$  with weight  $\{p\}$  is defined by [1]

$$\dot{\nabla}_k A = \nabla_k A - p T_k A. \quad (5)$$

REMARK 1 The prolonged covariant derivative preserves the weight.

The curvature tensor  $R_{jkl}^i$  of the Weyl connection is defined by

$$R_{jkl}^i = \frac{\partial}{\partial x^k} \Gamma_{jl}^i - \frac{\partial}{\partial x^l} \Gamma_{jk}^i + \Gamma_{hk}^i \Gamma_{jl}^h - \Gamma_{hl}^i \Gamma_{jk}^h \quad (6)$$

and the Ricci tensor  $R_{ij}$  of the Weyl connection is

$$R_{ij} = R_{ijm}^m. \quad (7)$$

Since the Weyl connection is not metric, the Ricci tensor  $R_{ij}$  is not necessarily symmetric. In fact,  $R_{[ij]} = n \nabla_{[i} T_{j]}$ . We remark that if  $T_j$  is a gradient, then the space is Riemannian.

It is easy to see that the covariant curvature tensor  $R_{lij}^k$  is a satellite of  $g_{ij}$  with weight  $\{2\}$ .

The Bianchi identity for the Weyl space is, by [2]

$$\dot{\nabla}_l R_{ijk}^h + \dot{\nabla}_k R_{ilj}^h + \dot{\nabla}_j R_{ikl}^h = 0. \quad (8)$$

## 2. Quasi-Recurrent Weyl Spaces

A non-flat Weyl space  $W_n(g_{ij}, T_k)$  will be called quasi-recurrent  $((QRW)_n$  in short) if the curvature tensor satisfies the following condition for some non-zero covariant vector field  $\phi_k$  ( $\neq T_k$ )

$$\dot{\nabla}_s R_{ijkl} = 2\phi_s R_{ijkl} + \phi_i R_{sjkl} + \phi_j R_{iskl} + \phi_k R_{ijsl} + \phi_l R_{ijks}. \quad (9)$$

A  $(QRW)_n$  manifold can be Weyl recurrent, i.e. it can, beside (9), satisfy

$$\dot{\nabla}_s R_{ijhk} = \phi'_s R_{ijhk}. \quad (10)$$

We examine the spaces satisfying (9) but not satisfying (10). Recurrent Weyl spaces have been examined in [2]. We note that  $\phi_k$  is a satellite of  $g_{ij}$



with weight  $\{0\}$ . By multiplying (9) by  $g^{il}$  and summing up with respect to  $i$  and  $l$  we get

$$\dot{\nabla}_s R_{jk} = 2\phi_s R_{jk} + \phi_j R_{sk} + \phi_k R_{js} + \phi_i (R_{sjk}^i + R_{jks}^i). \quad (11)$$

Similarly transvecting (11) by  $g^{jk}$  we obtain

$$\dot{\nabla}_s R = 2\phi_s R + \phi_k (R_{s.}^k + R_{.s}^k + R_{si..}^{ik} + R_{..is}^{ki}), \quad (12)$$

where  $R_{s.}^k = R_{sj} g^{kj}$  and  $R_{.s}^k = R_{js} g^{jk}$ .

Hence the scalar curvature of the  $(QRW)_n$  satisfies (12).

By changing the indices  $j$  and  $k$  in (11) and subtracting the resulting equation from the one obtained therefrom we obtain

$$\dot{\nabla}_s F_{jk} = \frac{2(n+1)}{n} \phi_s F_{jk} + \phi_k F_{js} + \phi_j F_{sk}, \quad (13)$$

where  $F_{jk} = R_{[jk]}$ .

In fact this is the relation between the complementary vector  $T_k$  and the recurrent vector  $\phi_k$ .

### 3. Hypersurfaces of Quasi-Recurrent Weyl Spaces

Let  $W_n(g_{ij}, T_k)$  be a hypersurface, with coordinates  $u^i$  ( $i = 1, 2, \dots, n$ ) of a Weyl space  $W_{n+1}(g_{ab}, T_c)$  with coordinates  $x^a$  ( $a = 1, 2, \dots, n+1$ ). The metrics of  $W_n$  and  $W_{n+1}$  are connected by the relations

$$g_{ij} = g_{ab} x_i^a x_j^b \quad (i, j = 1, 2, \dots, n; \quad a, b = 1, 2, \dots, n+1), \quad (14)$$

where  $x_i^a$  denotes the covariant derivative of  $x^a$  with respect to  $u^i$ .

It is easy to see that the prolonged covariant derivative of a satellite  $A$ , relative to  $W_n$  and  $W_{n+1}$ , are related by

$$\dot{\nabla}_k A = x_k^c \dot{\nabla}_c A \quad (k = 1, 2, \dots, n; \quad c = 1, 2, \dots, n+1). \quad (15)$$

Let  $n^a$  be the contravariant components of the vector field of  $W_{n+1}$  normal to  $W_n$  which is normalized by the condition

$$g_{ab} n^a n^b = 1. \quad (16)$$

The moving frame  $\{x_a^i, n_a\}$  in  $W_n$ , reciprocal to the moving frame  $\{x_i^a, n^a\}$  is defined by the relations

$$n_a x_i^a = 0, \quad n^a x_a^i = 0, \quad x_i^a x_a^j = \delta_i^j. \quad (17)$$

Remembering that the weight of  $x_i^a$  is  $\{0\}$ , the prolonged covariant derivative of  $x_i^a$  with respect to  $u^k$  is found as

$$\dot{\nabla}_k x_i^a = \nabla_k x_i^a = \omega_{ik} n^a, \quad (18)$$

where  $\omega_{ik}$  is the second fundamental form. It can be shown that  $\omega_{ik}$  is a satellite of  $g_{ij}$  with weight  $\{1\}$ .

The following two relations, which are respectively the generalization of Gauss and Mainardi-Codazzi equations, are obtained in [2]

$$R_{pijk} = \Omega_{pijk} + \bar{R}_{dbce} x_p^d x_i^b x_j^c x_k^e, \quad (19)$$

$$\dot{\nabla}_k \omega_{ij} - \dot{\nabla}_j \omega_{ik} + \bar{R}_{dbce} x_i^b x_j^c x_k^e n^d = 0, \quad (20)$$

where  $\bar{R}_{dbce}$  is the covariant curvature tensor of  $W_{n+1}$  and  $\Omega_{pijk}$  is the Sylvesterian of  $\omega_{ij}$  defined by  $\Omega_{pijk} = \omega_{pj} \omega_{ik} - \omega_{pk} \omega_{ij}$ .

**THEOREM 1** A hypersurface  $W_n$  of  $(QRW)_{n+1}$  satisfies the following.

$$\begin{aligned} \dot{\nabla}_s R_{ijkl} - \dot{\nabla}_s \Omega_{ijkl} &= 2\phi_s(R_{ijkl} - \Omega_{ijkl}) + \phi_i(R_{sjkl} - \Omega_{sjkl}) + \\ &+ \phi_j(R_{iskl} - \Omega_{iskl}) + \phi_k(R_{ijsl} - \Omega_{ijsl}) + \\ &+ \phi_l(R_{ijks} - \Omega_{ijks}) + \bar{R}_{abcd} \dot{\nabla}_s(x_i^a x_j^b x_k^c x_l^d). \end{aligned} \quad (21)$$

*Proof 1* By taking the prolonged covariant derivative of (19) we have

$$\dot{\nabla}_s R_{ijkl} = \dot{\nabla}_s \Omega_{ijkl} + \dot{\nabla}_s(\bar{R}_{abcd} x_i^a x_j^b x_k^c x_l^d) + \bar{R}_{abcd} \dot{\nabla}_s(x_i^a x_j^b x_k^c x_l^d).$$

Moreover,

$$\dot{\nabla}_s R_{ijkl} = \dot{\nabla}_s \Omega_{ijkl} + \dot{\nabla}_e(\bar{R}_{abcd} x_i^a x_j^b x_k^c x_l^d x_s^e) + \bar{R}_{abcd} \dot{\nabla}_s(x_i^a x_j^b x_k^c x_l^d).$$

By using (9), Mainardi-Codazzi equations and (15), we obtain the result.

**THEOREM 2** A simply connected hypersurface of  $(QRW)_{n+1}$  is Riemannian.

*Proof 2* If we change the indices  $k, l, s$  cyclically in (21), we obtain two more equations. Namely

$$\begin{aligned} \dot{\nabla}_k R_{ijls} - \dot{\nabla}_k \Omega_{ijls} &= 2\phi_k(R_{ijls} - \Omega_{ijls}) + \phi_i(R_{kjls} - \Omega_{kjls}) + \\ &+ \phi_j(R_{ikls} - \Omega_{ikls}) + \phi_l(R_{ijks} - \Omega_{ijks}) + \\ &+ \phi_s(R_{ijlk} - \Omega_{ijlk}) + \bar{R}_{abcd} \dot{\nabla}_k(x_i^a x_j^b x_l^c x_s^d), \end{aligned} \quad (22)$$

$$\begin{aligned} \dot{\nabla}_l R_{ijsk} - \dot{\nabla}_l \Omega_{ijsk} &= 2\phi_l(R_{ijsk} - \Omega_{ijsk}) + \phi_i(R_{ljks} - \Omega_{ljks}) + \\ &+ \phi_j(R_{ilks} - \Omega_{ilks}) + \phi_s(R_{ijlk} - \Omega_{ijlk}) + \\ &+ \phi_k(R_{ijsl} - \Omega_{ijsl}) + \bar{R}_{abcd} \dot{\nabla}_l(x_i^a x_j^b x_s^c x_k^d). \end{aligned} \quad (23)$$

Adding these three equations and using Mainardi-Codazzi equations and Bianchi identities, we find

$$\phi_i(R_{ljsk} + R_{kjl s} + R_{sjkl}) = 0. \quad (24)$$

Since  $\phi_i \neq 0$  we have

$$R_{ljsk} + R_{kjl s} + R_{sjkl} = 0. \quad (25)$$

From the first Bianchi identity we get

$$R_{(lj)sk} + R_{(kj)ls} + R_{(sj)kl} = 0. \quad (26)$$

Hence, the result follows from the fact that  $R_{(ij)sk} = 2g_{ij}T_{[s,k]}$ .

A hypersurface  $W_n$  of  $W_{n+1}$  is called totally geodesic if  $\omega_{ij} = 0$ . Therefore we have the following theorem.

**THEOREM 3** If the simply connected hypersurface of  $(QRW)_{n+1}$  is totally geodesic, then the hypersurface is Riemannian quasi-recurrent.

*Proof 3* Follows from (21) and the Theorem 2.

### References

- [1] HLAVATY, V. (1949): Théorie d'immersion d'une  $W_m$  dans  $W_n$ , *Ann. Soc. Polon. Math.*, Vol. 21, pp. 196–206.
- [2] CANFES, Ö. E. – ÖZDEĞER, A.: Some Applications of Prolonged Covariant Differentiation in Weyl Geometry, (to appear in *Journal of Geometry*).



## ON THE TRANSIENT BEHAVIOUR OF CONTROLLED PROPULSION PLANTS

Gábor PAP

Department of Aircraft and Ships  
Technical University of Budapest  
H-1521 Budapest, Hungary

Received: 15 Apr. 1996

### Abstract

This paper makes known the results of the investigations carried out into the transient behaviour of closed control loops of a ship propulsion plant. Transient characteristics of various speed governors as well as their applicability are compared. Comparison is made on the basis of transient characteristics gained by computer simulation, and represented in figures.

*Keywords:* transient characteristics, speed governors, propulsion plant.

### 1. Introduction

A series of computer simulations has been carried out at our department, in order to gain information on the transient behaviour of a ship's propulsion plant in waves.

Closed control loops, containing the following speed governors, have been compared:

- a direct acting mechanical one,
- a PI-type hydraulic one, equipped with a compensating vanishing feedback,
- two versions of a two-pulse electronic speed governor, co-operating with a constant-pressure fuel injection system.

The following characteristics as well as decisive phenomena of the closed control loops have been calculated and compared: momentary speed variation, time constants, frequency response, stability, optimum setting of compensation, influence of the fuel injection system, the effect on the system dynamics of the deteriorating conditions of the fuel pumps.

## 2. Models of the System Components

### 2.1. Basic Attributes

The applied mathematical models of the engine and of the speed governors are linearized and quasi-stationary. The matching point, i. e. the basis of linearization is defined by 67% fuelling and 90% engine speed, with reference to the nominal values. In order to gain better-conditioned models, relative variables are applied, instead of physical characteristics. Having been divided by the matching point value, the change, referring to the matching point, of a variable yields its relative value.

The investigations have been carried out by means of state-space models written in MATLAB supported by its own 'Control Toolbox'.

The excitation function has been considered sinusoidal, deterministic function of two variables. The wave pattern has been presumed to be regular. The ship's advancing has been considered perpendicular to the crests. In most cases the angular frequency and the relative amplitude of the excitation have been  $\omega_g = 1.08$  [rad/s] and  $\alpha_e = 0.325$ , respectively.

In the course of our investigations friction forces on the moving parts of the speed governors as well as that of the fuel injection system have been assumed to be proportional to the relative velocity of the moving parts, applying a wide range of  $\vartheta$  coefficient of proportionality. This approximation is based upon the vibrations of the lubricated moving parts.

The model accuracy in steady state condition, on the base of the test bench diagrams of the engine, proved to be sufficient for system dynamics application, while its correct transient properties have been justified by sea trials.

### 2.2. Models of a Supercharged Marine Diesel Engine

A four-stroke, medium-speed, supercharged marine diesel engine 6NVD48A-2U type of SKL has been chosen, as the physical basis of the mathematical model.

Two different state-space models of the engine, for different applications, have been set up, applying two different methods [1]. The applied setting-up methods of the state-space models are founded on the transfer function form of the mathematical model of a supercharged diesel engine developed by KRUTOV [2]. The layout and the block diagrams in transfer function representation of the model are shown in *Fig. 1* and *2*, respectively. According to these figures,  $\kappa$  relative displacement of the fuel rack and  $\alpha_e$  relative load are the input signals, while  $\varphi$  relative speed of the engine is the output signal of the model. Most of the system components are of first-order proportional type.

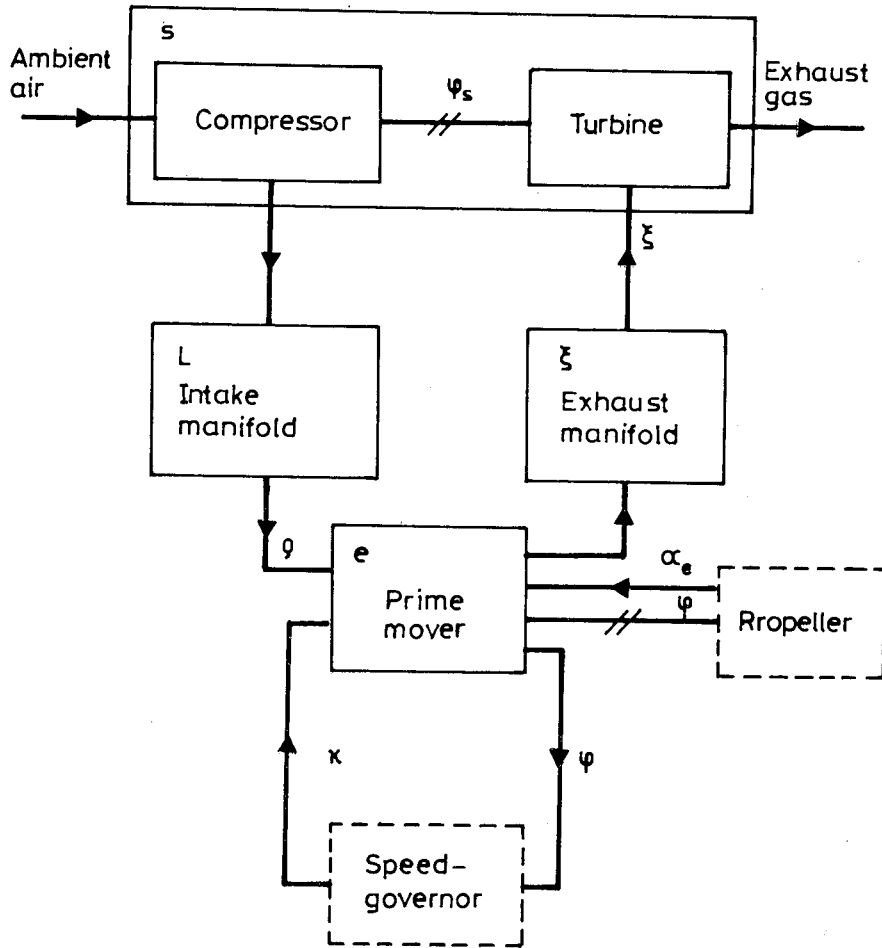


Fig. 1. Layout of the model of a supercharged diesel engine

### 2.3. Model of a Direct-acting PT2-type Mechanical Speed Governor

The model is represented by its partial transfer functions connected in parallel

$$Y_g^\varphi(p) = \frac{1}{d_g(p)} = \frac{1}{T_g^2 p^2 + T_d p + \delta_z} \quad (1)$$

of  $\varphi$  as one of the input signals, and

$$Y_g^\alpha(p) = -\frac{\Theta_g}{d_g(p)} = -\frac{\Theta_g}{T_g^2 p^2 + T_d p + \delta_z} \quad (2)$$

of the  $\alpha_g$  relative tensioning of the flyweight springs considered the second input signal. The output signal of the model is  $\eta$  relative displacement of

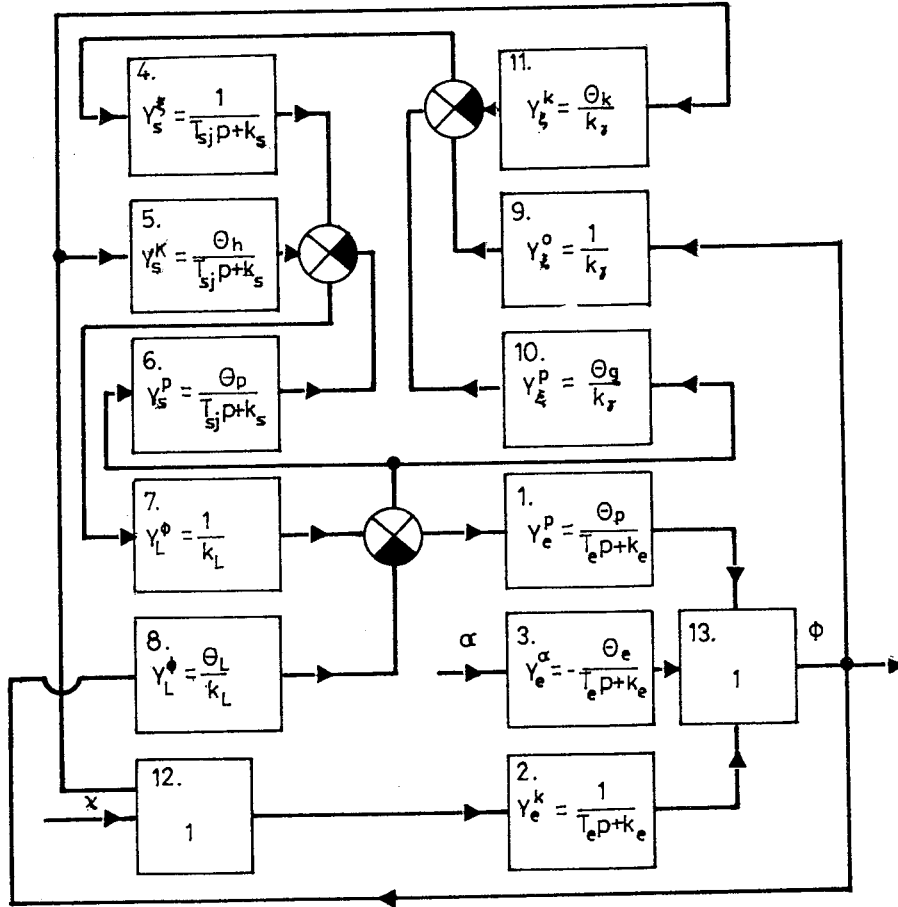


Fig. 2. Block diagram of the model of a supercharged diesel engine

the flyweight sleeve.

Both transfer functions (1) and (2) are of second-order proportional type. The state-space model of the governor has been set up on the basis of the above transfer function representation, by means of converting commands in MATLAB.

#### 2.4. Model of a PI-type Hydraulic Speed Governor

This model is based upon the WOODWARD UG proportional plus integral type hydraulic universal speed governor equipped with a vanishing type compensating feedback.



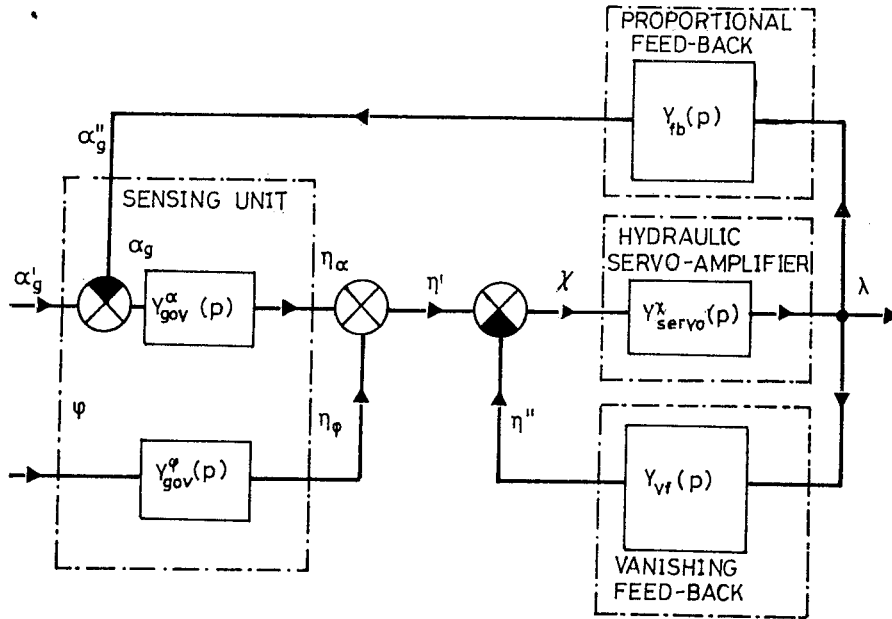


Fig. 3. Block diagram of a PI-type hydraulic universal speed governor

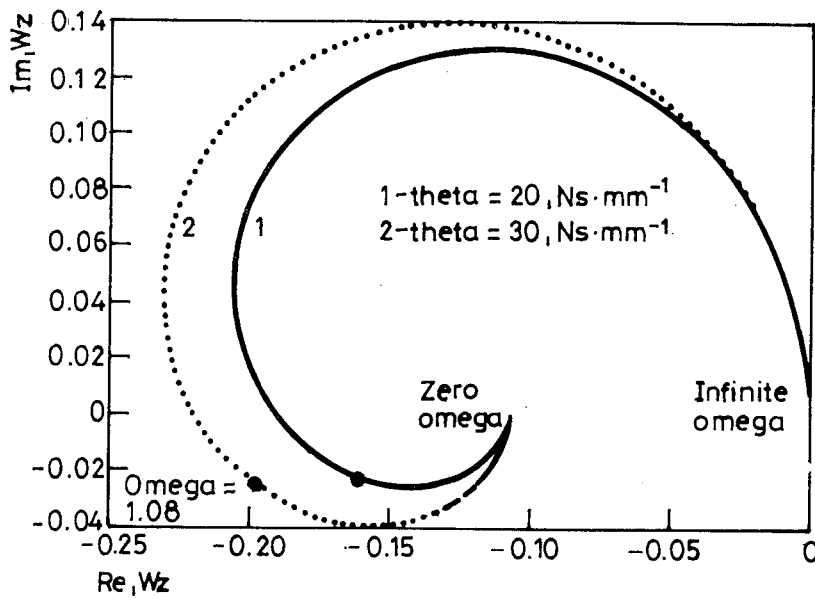


Fig. 4. Nyquist diagram of the controlled variable

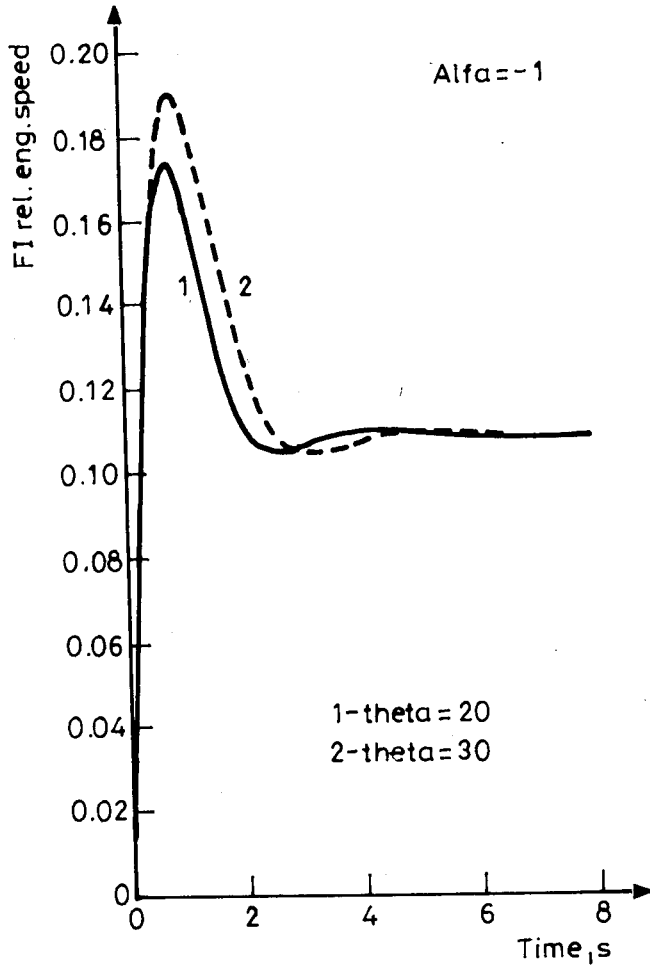


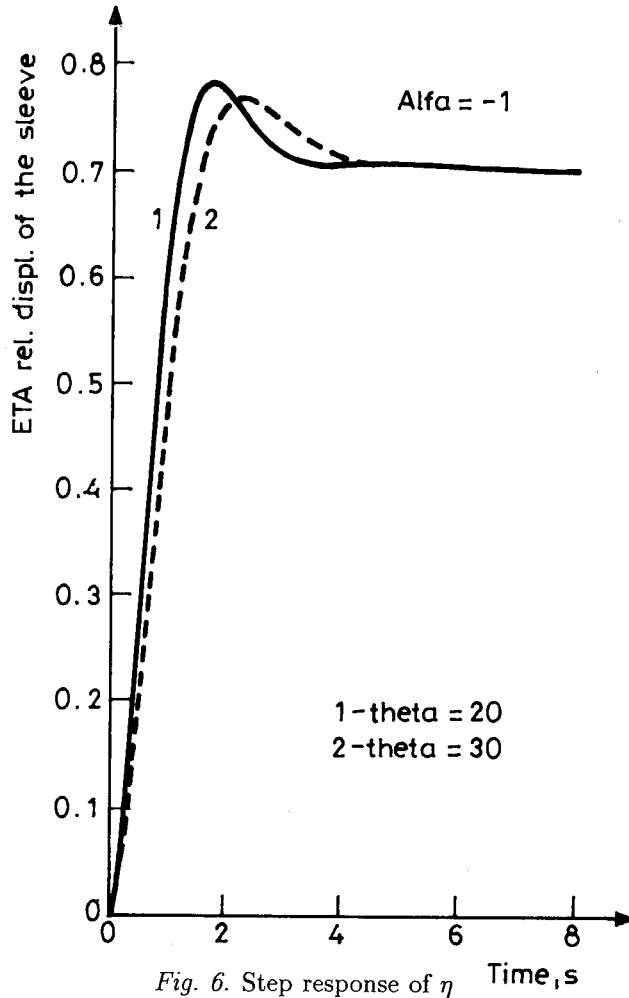
Fig. 5. Step response of the controlled variable

According to its layout in transfer function representation (*Fig. 3*),  $\varphi$  and  $\alpha'_g$  partial relative tensioning of the flyweight springs are the input signals, while  $\lambda$  relative displacement of the servo-piston is the output signal of the model.

The transfer functions and the input-output signals of the subsystems in *Fig. 3* are as follows:

- The integral type transfer function related to  $\chi$  relative displacement of the pilot valve, as the input signal of the hydraulic servo-amplifier unit, is

$$Y_{servo}^{\chi}(p) = \frac{1}{T_{servo} p}. \quad (3)$$

Fig. 6. Step response of  $\eta$ 

The output signal of the subsystem is  $\lambda$ , the very output of the model.

- The second-order proportional type partial transfer functions, connected in parallel, of the sensing unit subsystem are

$$Y_{gov}^{\alpha}(p) = \frac{\Theta_{gov}}{T_g^2 p^2 + T_d p + \delta_z} \quad (4)$$

of  $\alpha_g$  as one of the input signals, and

$$Y_{gov}^{\varphi}(p) = \frac{1}{T_g^2 p^2 + T_d p + \delta_z} \quad (5)$$

of  $\varphi$  considered the second input signal. The output signal of the subsystem is  $\eta'$  partial relative displacement of the flyweight sleeve.

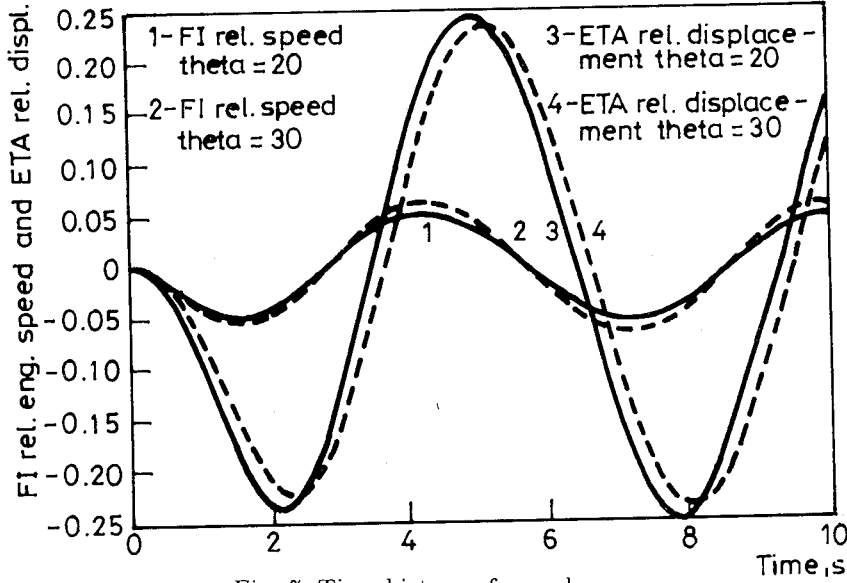


Fig. 7. Time history of  $\varphi$  and  $\eta$

- The proportional type transfer function of the inner proportional feedback is

$$Y_{fb}(p) = \Theta_{fb}. \quad (6)$$

$\lambda$  is the input signal, and  $\alpha_g''$  partial relative tensioning of the flyweight springs is the inner feedback signal, as the output one of the subsystem.

- The first-order derivative type transfer function of the compensating vanishing feedback

$$Y_{vf}(p) = u\beta_{PI} \frac{T_{PI} \cdot p}{1 + T_{PI} \cdot p} \quad (7)$$

has  $\lambda$  input signal and  $\eta''$  partial relative displacement of the flyweight sleeve, where  $T_{PI}$  and  $u$  are the time constant and the rate of the compensation, respectively.

The state-space model of the governor has been developed by simple conversion in MATLAB. Detailed information on the models of the speed governors is available in [3], [4].

### 2.5. Models of a Two-pulse Bing-bang Type Electronic Speed Governor

The operating method of this governor is supposed to be similar to that of the mechanical speed governors, operating on two-stroke, low-speed marine

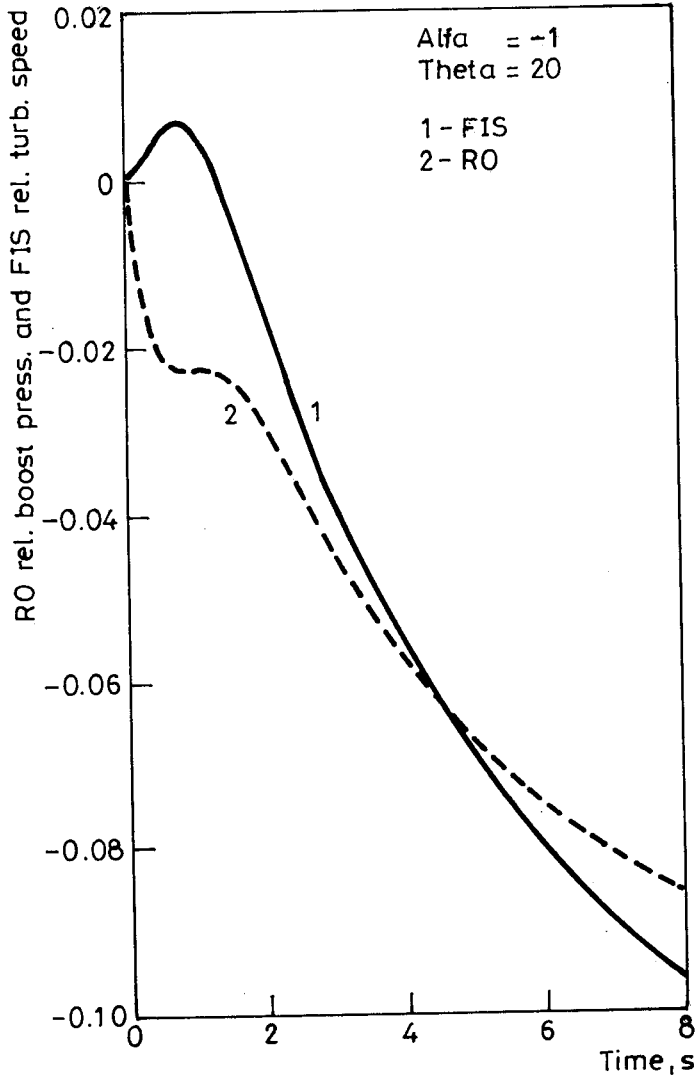


Fig. 8. Step response of  $\varphi_s$  and  $\rho$

diesel engines. Thus, value of the controlled propeller speed is maintained by the governor between upper and lower limits, applying successive cut-out of injection or successive reduction in amount of the injected fuel.

Two models of this kind were developed, both of them have been written in form of M-files in MATLAB, by using logical variables. The only difference between these models refers to the rate of fuelling during the cut-out periods, one of them cuts out injection in these periods completely.

Speed governors of this type have been supposed to be co-operating

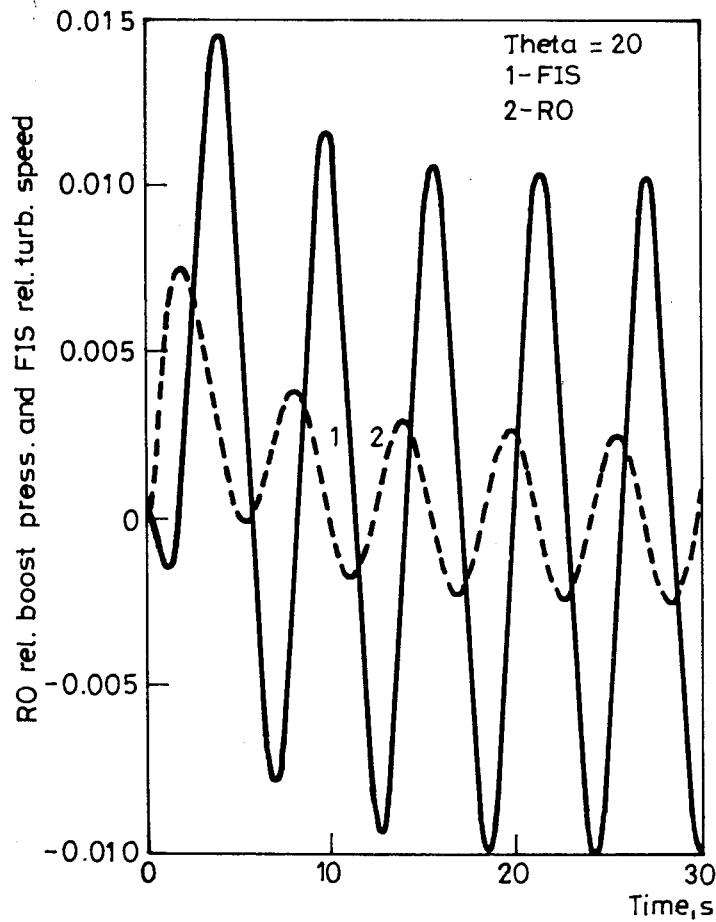


Fig. 9. Time history of  $\varphi_s$  and  $\rho$

with electronically controlled constant-pressure injection systems [5]. Time lag represented by the applied electro-hydraulic injector valves has been neglected.

### 3. Results of the Investigations

#### 3.1. Closed Control Loop, Comprising a Direct-acting PT2-type Mechanical Speed Governor

Figs 4-7 represent the influence of the  $\vartheta$  coefficient of proportionality, i.e. the effect of the changing condition of the fuel injection system, on

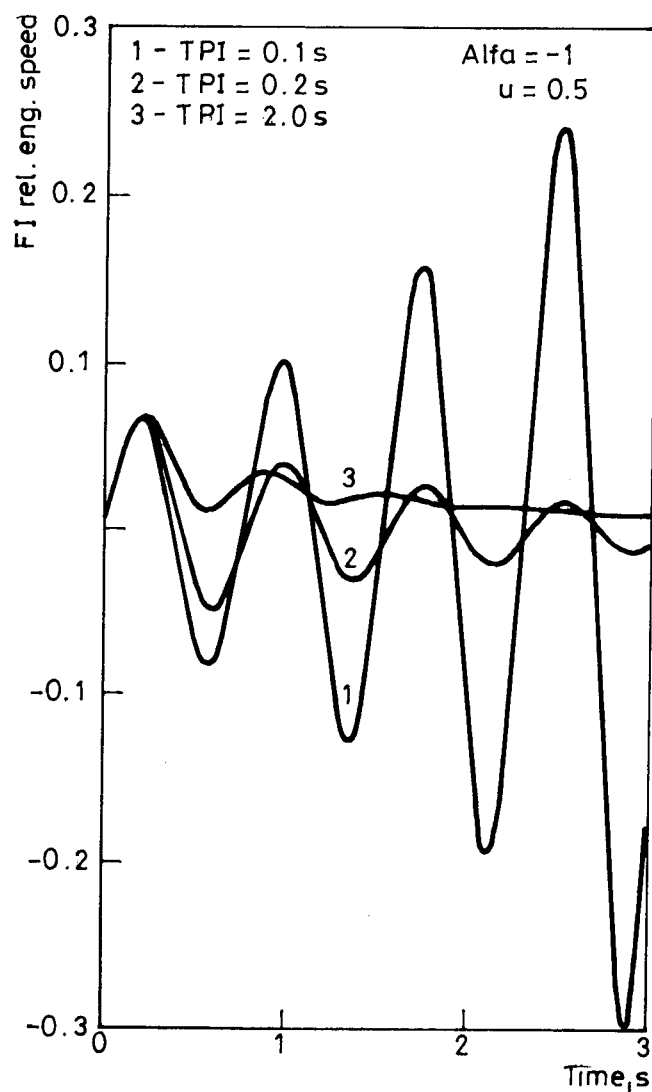


Fig. 10. Step responses at various pairs of  $u$  and  $T_{PI}$

- the Nyquist gain-phase characteristics of the closed control loop (Fig. 4),
- the step response of  $\varphi$  controlled variable at  $\alpha_e = -1$  sudden load rejection (Fig. 5),
- the step response of  $\eta$  relative displacement of the flyweight sleeve at  $\alpha_e = -1$  (Fig. 6),
- the time history of  $\varphi$  and  $\eta$  at sinusoidal excitation of  $\omega_g = 1.08 \text{ [rad/s]}$  angular frequency (Fig. 7).

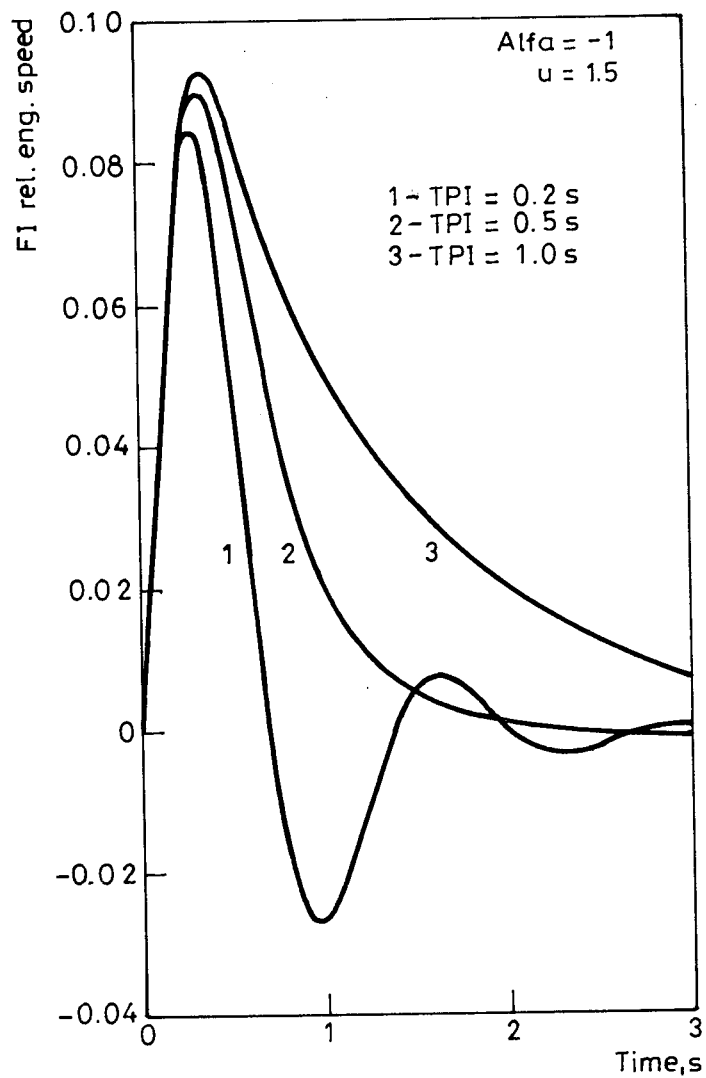


Fig. 11. Step responses at various pairs of  $u$  and  $T_{PI}$

Figs 8 and 9 comprise the step response and the time history, at  $\omega_g = 1.08$  [rad/s] sinusoidal excitation, of  $\rho$  relative boost pressure and  $\varphi_s$  relative speed of the supercharger.



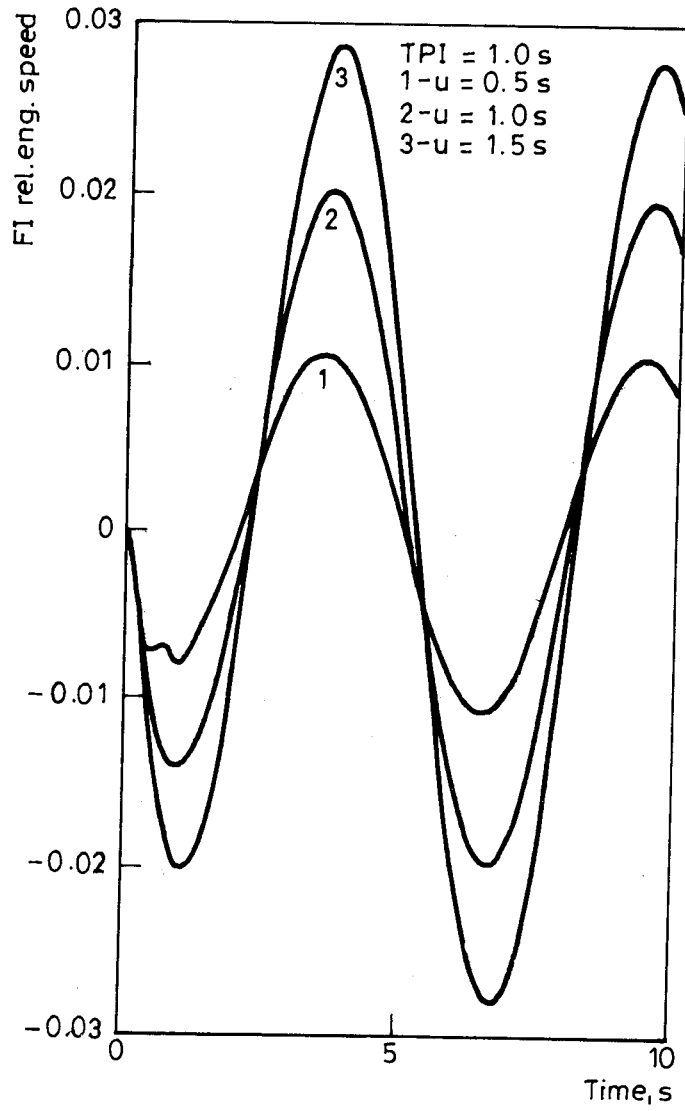


Fig. 12. Time history of  $\varphi$  at various pairs of  $u$  and  $T_{PI}$

### 3.2. Closed Control Loop, Comprising a PI-type Hydraulic Speed Governor

Figs 10–12 represent the influence of the varying  $u$ ,  $T_{PI}$  pairs on the step-response (Figs 10 and 11) as well as on the time history at  $\omega_g = 1.08$  [rad/s] sinusoidal excitation, of controlled variable  $\varphi$  (Fig. 12).

Fig. 13 shows the time history of  $\lambda$  relative displacement of the servopiston, at  $\omega_g = 1.08$  [rad/s] sinusoidal excitation.

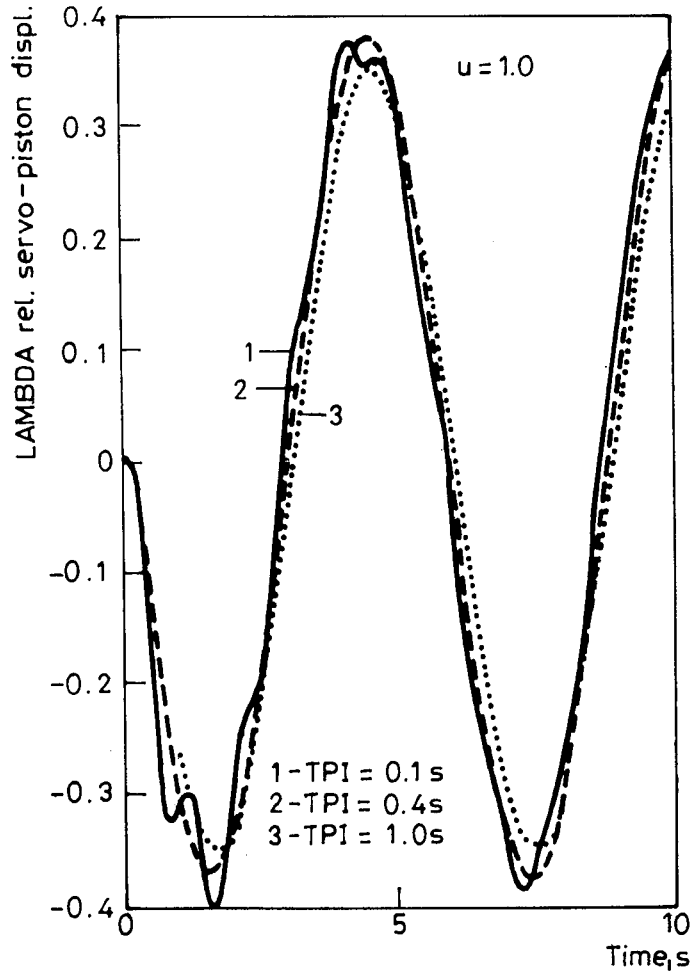


Fig. 13. Time history of  $\lambda$  at various pairs of  $u$  and  $T_{PI}$

In Fig. 10 curves 2 and 3 relate to stable settings, while curve 1 to an instable setting of the compensating system. Optimal compensation provides quick response of the system, without hunting or surging of the prime mover. In Fig. 11 curve 1 corresponds to an undercompensated, curve 3 to an overcompensated, while curve 2 to the optimally compensated settings of the system, whereas all these settings yield stable operation. In Fig. 12 on the curve 1, likewise on the curve 1 in Fig. 13, small wavelets have been superposed to the sine-shaped output signal. This phenomenon demonstrates hunting of the prime mover due to an undercompensated setting of  $T_{PI}$  and  $u$ .

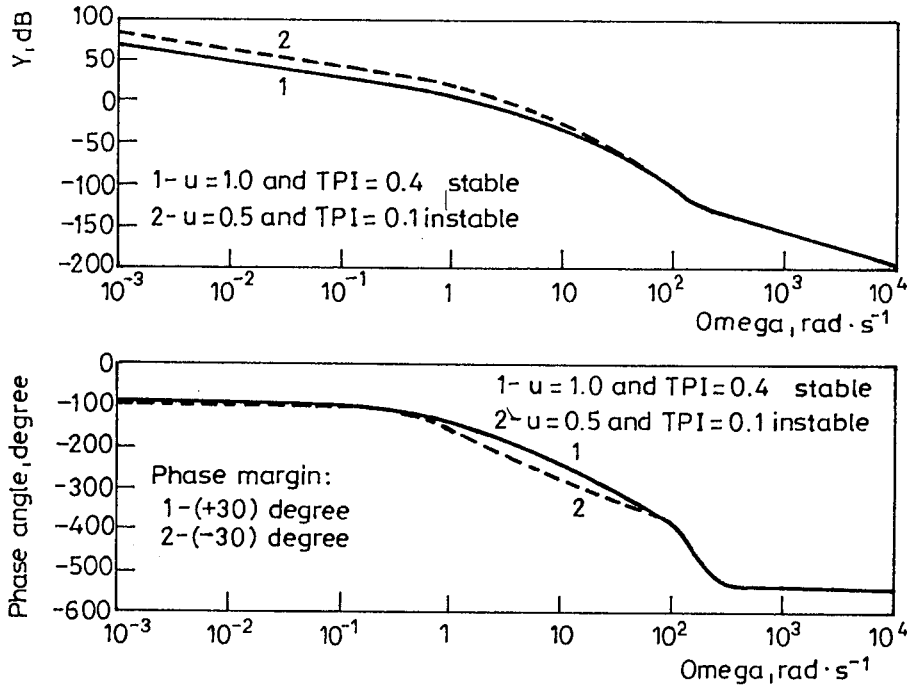


Fig. 14. Bode diagram of the open control loop

Fig. 14 contains the Bode logarithmic plots of the open control loop. These plots have been calculated at a stable, as well as at an instable pair of  $u$  and  $T_{PI}$  variables of the compensating vanishing feed back.

Figs 10-14 have been plotted assuming new condition of the fuel injection system, such as the fuel rack, linkage and the constant-stroke, edge-controlled fuel pumps.

### 3.3. Closed Control Loop, Comprising a Two-pulse Bing-bang Type Electronic Speed Governor

Figs 15 and 16 represent the time history of  $\varphi$  controlled variable and that of  $\kappa$  relative displacement of the fuel rack, at  $\omega_g = 1.08$  [rad/s] sinusoidal excitation. Pre-set lower  $\kappa$  limit has been  $\kappa = -1$  in Fig. 15, while  $\kappa = -0.325$  in Fig. 16.

Comparing the time history of the  $\varphi$  controlled variable in Fig. 15 to that in Fig. 16, the latter shows better control performance. By applying smaller gap between the upper and lower fuelling limits result fluctuation at lower frequency of the  $\varphi$  relative engine speed.

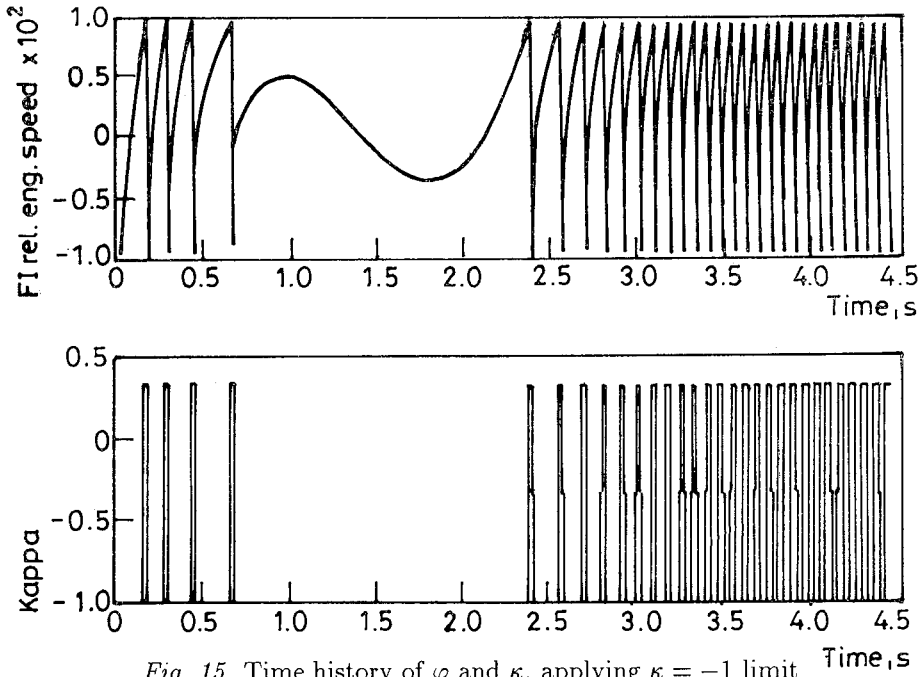


Fig. 15. Time history of  $\varphi$  and  $\kappa$ , applying  $\kappa = -1$  limit

#### 4. Concluding Remarks

On the basis of our investigations the following conclusions can be drawn:

- Applying a direct-acting mechanical speed governor, amplitude ratio of  $\varphi$  controlled variable, at regular sinusoidal waves as an excitation, is basically determined by the fuel injection system. Assuming deteriorated conditions of the fuel rack, linkage and of the fuel pumps,  $\xi_\varphi$  damping factor of the second-order system, representing the speed governor, is far from being optimum, even at robust dimensions of the governor. Application of constant-stroke, edge-controlled fuel pumps results considerable drawbacks, constant-pressure fuel injection systems are favourable in this regard. However, on the other hand, this governor is less influenced by the varying excitation frequency (*Figs 4–7*).
- Regarding direct-acting mechanical speed governors, at a sudden change in load, e.g. due to lost propeller, controlled variable probably cannot be maintained below 120% of its nominal value prescribed as a limit by the rules of registers, thus application of an independent overspeed protection is necessary. Applying a governor of this type, influence of the speed and torque fluctuations due to waves, concerning noise and vibration, cannot be disregarded (*Figs 5 and 6*).

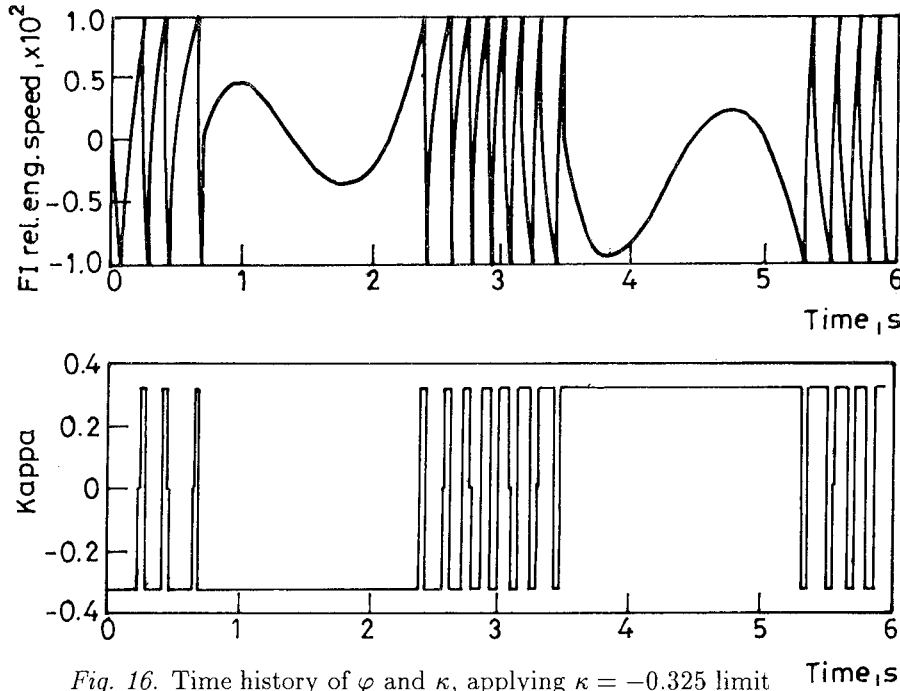


Fig. 16. Time history of  $\varphi$  and  $\kappa$ , applying  $\kappa = -0.325$  limit

- Transient behaviour and stability of a closed control loop, containing a PI-type hydraulic speed governor, is highly influenced by the excitation frequency. Optimum setting of  $u$  and  $T_{PI}$  is basically frequency dependent. The momentary speed variation, the length of the transient process, surging and stability are sharply influenced by the pair of  $u$  and  $T_{PI}$  (Figs 10–16).
- Two-pulse speed governors are less sensitive to the excitation frequency and to the deteriorated conditions of the fuelling system. However, the scope of application for the two-pulse speed governors is limited by the torsional vibration of the shafting. Their application in propulsion plants, containing reverse-reduction gears or flexible couplings, is conditional (Figs 15 and 16).
- Surging in the angular velocity of the turbo-supercharger impeller proved to be negligible in this engine category, applying even the less favourable type of the investigated speed governors at a sudden load change (Figs 8 and 9).

### References

- [1] HARANGOZÓ, É. – PAP, G. (1995): Linearized Model in MATLAB of a Supercharged Diesel Engine. *Járművek, Építőipari és Mezőgazdasági Gépek*, No. 10 pp. 349–354 (in Hungarian).
- [2] KRUTOV, V. I. (1987): Automatic Control of Internal Combustion Engines. Mir Publisher, Moscow.
- [3] PAP, G. (1995): Investigations into the Transient Process in Waves of a Marine Propulsion Plant Equipped with Different Kinds of Speed Governors. Dissertation at the Technical University of Budapest (in Hungarian).
- [4] PAP, G.: Investigations into the Transient Process in Waves of a Marine Propulsion Plant Equipped with Different Kinds of Speed Governors (*Proc. of the 5th Mini Conference on Vehicle System Dynamics*, Budapest, 1996).
- [5] PARKER, S. (1994): Development Driven by Emissions Legislation. *The Motor Ship*, No. 3, pp. 25–28.

## ON SIMULATION OF OPERATION CONDITIONS OF RUNNING GEARS IN THE PERIOD OF DESIGN<sup>1</sup>

István ZOBORY and Elemér BÉKEFI

Department of Railway Vehicles  
Technical University of Budapest  
H-1521 Budapest, Hungary

Received: September 20, 1995

### Abstract

When designing new vehicles, the reliable prediction of the future operation conditions of running gears based on quantitative statistics is very important both for the strength dimensioning and for ensuring the required riding comfort. This study introduces the analysis of the vertical dynamics of a vehicle under design, based on real-time simulation using the data of the traction and trailer units of the train and those of the railway line in question, especially the spectral density function of the vertical track irregularities. The combined numerical treatment of the train operation process and the vertical vehicle vibrations, as well as the predicted load statistics are illustrated for the running gear and suspension system of a four-axle bogie vehicle in suburban traffic.

*Keywords:* railway vehicle system dynamics, stochastic vibrations, load statistics.

### 1. Introduction

The loading conditions of a complete railway vehicle and its running gear are typically of stochastic character, if the regular operation process of the vehicle is considered in a long time interval [1]. The mentioned stochasticity is caused by the random length of the sequential speed-timing cycles, by the random effects due to driver's activity in the tractive and braking force exertion determining the train motion, as well as by the changing and in stochastic sequentionality realizing track-resistance forces. On the other hand, railway vehicles and also the trains are complicated vibratory systems, so in the operation of running gears one should reckon with dynamical excess loads caused by stochastic vibration processes excited by the irregularities in the track [2,3,4]. In this study the application of the general real-time loading-state simulation method developed at the Department of Railway Vehicles of the Technical University of Budapest will be introduced to determine the future vertical load statistics of a vehicle *being designed for operation under given train track and time schedule conditions*. When

---

<sup>1</sup>This research was supported by the Hungarian Ministry of Culture and Education, Grant No. 82/94

applying the simulation method, the train should be led along the specified railway line(s), by giving appropriate controls from the computer keyboard. In the course of the train motion simulation the time functions of the vertical track irregularities belonging to each wheelset are determined, based on the known spectral density function(s) of the irregularities. The mentioned time functions are used as excitation functions of the vertical in-plane dynamical model of the vehicle considered. The set of equations of the model is solved numerically and the statistics of the motion and force processes realizing in the connection elements of the model are determined. The load statistics ensure exact predictions for the operational and strength dimensioning of the running and suspension gear components.

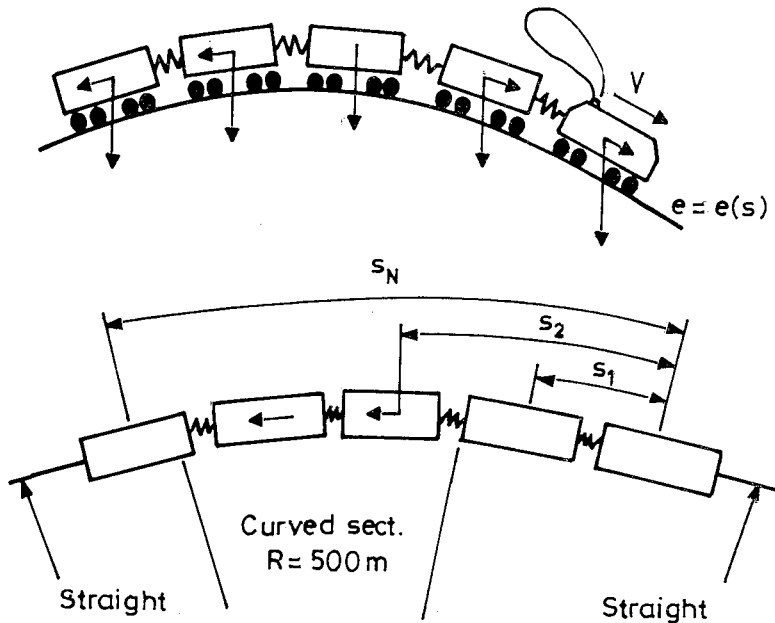


Fig. 1. Side and top views of the lumped parameter train model on the track

## 2. Real Time Simulation of the Train Motion

For the simulation of the train motion the complex longitudinal dynamical model and the program system described in [4] were used. This longitudinal dynamical model takes into consideration one loco at the front end of the train and maximum 30 cars. In the train model the vehicles are represented by lumped masses as it is indicated for a train in Fig. 1.

To specify the model, the geometrical and vertical characteristics of the vehicles, as well as the longitudinal stiffness and damping values of the intervehicle connections should be fixed, see Fig. 2.



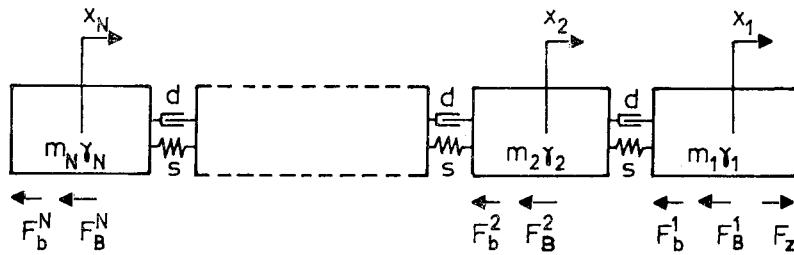


Fig. 2. The train as a longitudinal vibratory system

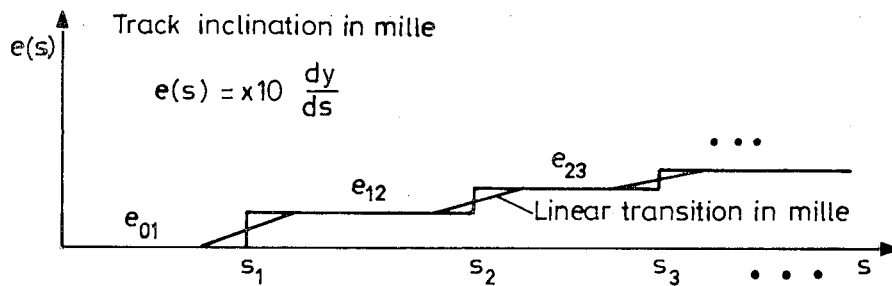


Fig. 3. Track inclination function vs. track arc length

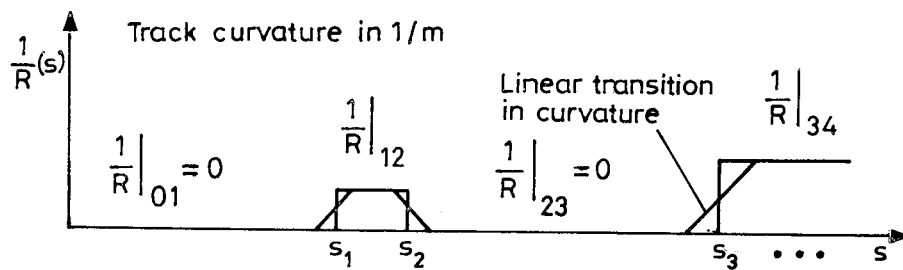


Fig. 4. Track curvature function vs. track arc length

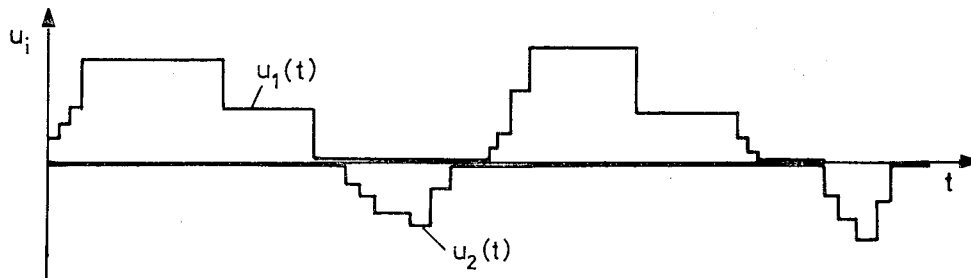


Fig. 5. Drive and brake control functions vs. time

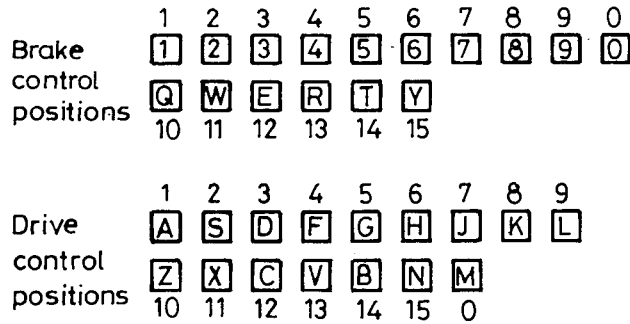


Fig. 6. Partition of the keyboard positions

Also the coefficients of the specific basic traction resistances, the brake cylinder diameters, the mechanical advantages of the brake rigging, as well as the velocity and brake-block pressure dependent friction coefficients of the friction wheel brake should be specified for each vehicle in the train. The adhesion limit is considered as a velocity independent constant. The tractive-effort performance curves of the traction unit should be specified as a bivariate function of the velocity and the drive control. The maximum number of the tractive-effort control positions is 15, and the same is the number of the loco driver's brake valve handle positions. The railway track is specified by two track arc-length dependent piecewise linear functions, namely by the *inclination conditions* and the *curvature conditions*. The track inclination conditions are characterized by the mille values. In case of constant inclination angles the mille values are also constants, while in case of the vertical rounding circles the variation of the mille values is approximated by a linear law (see Fig. 3).

The *curvature conditions* are characterized by the numerical values of the track curvatures, see Fig. 4.

In straight sections the curvature takes zero values, in circular sections it takes constant values, while in transition curves it is a linear function of the arc length, reflecting the *clotoid geometry*.

By using appropriate integer valued  $u_1(t) \leq 0$  drive, and  $u_2(t) \leq 0$  brake controls given from the computer keyboard and the real-time numerical solution of the equations of motion of the train model, the train can be led along the railway line (or lines) specified by the customer railway company. A typical control function pair is shown in Fig. 5.

The partition of the set of keyboard positions for initiation the required brake and drive control integers is shown in Fig. 6.

Thus, the speed - timing diagram  $v = f(t)$ , or the speed - distance covered diagram  $v = f(x)$  can be determined using an integration time step of length 0.01 s for each vehicle in the train. For example a set of time-dependent diagrams appearing on the computer screen is visualized in Fig. 7.

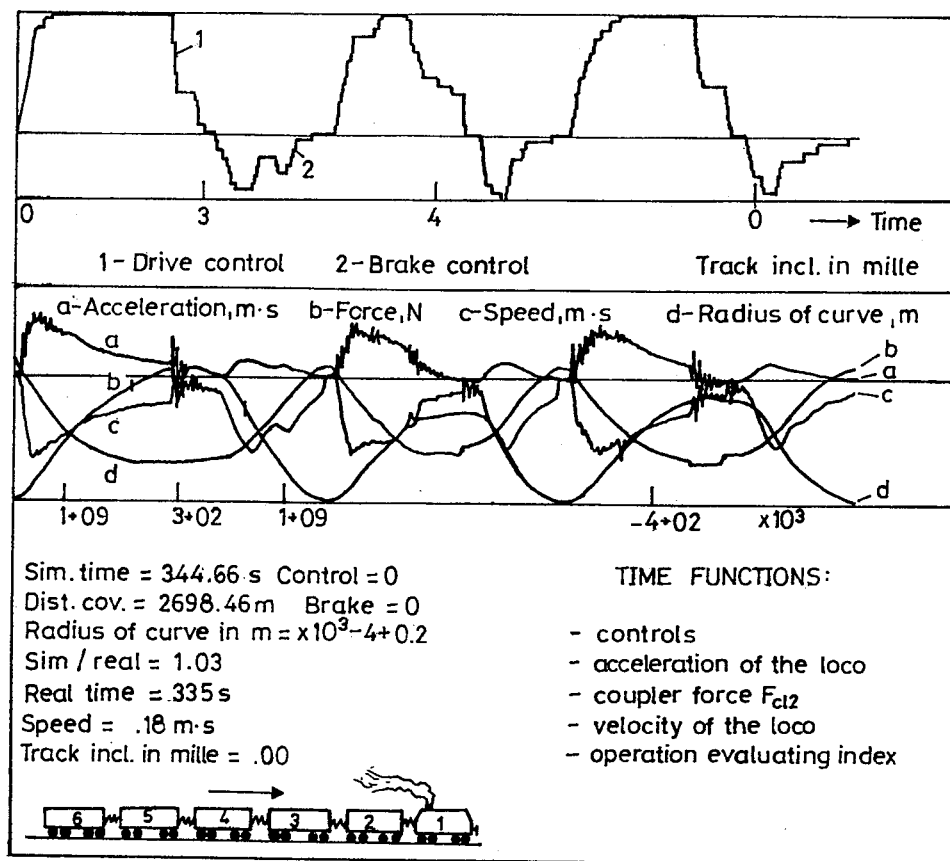


Fig. 7. Graphical and numerical information appearing on the screen

Similarly, the distances covered by the gravity points of the wheelsets become known for any vehicle in the train, also on a time sequence of pace 0.01 s.

### 3. Generation of Track Irregularities

The vertical irregularities of the railway track are approximated by the realization of a track length parameter weakly stationary stochastic process. It can be assumed that the spectral density function globally characterizing the vertical irregularities of the railway line has been specified by the customer railway company. It is known [1,2,3], that the realization function of a weakly stationary track irregularity process  $u(x)$  having spectral density

function  $S(\Omega)$  can be obtained in the following form:

$$u(x) = c_0 + \sum_k 2c_k \cos(\Omega_k x + \psi_k) .$$

In the formula,  $\Omega_0, \Omega_1, \dots, \Omega_N$  stand for the given spatial angular frequency points, at which spectral density ordinates  $S(\Omega_0), S(\Omega_1), \dots, S(\Omega_N)$  are specified. Sequence  $c_0, c_1, \dots, c_N$ , consists of *normally distributed independent random variables of zero expectation and prescribed variances*:

$$\sigma^2(c_k) = S(\Omega_k) \Delta\Omega, \quad k = 0, 1, 2, \dots, N$$

Here  $\Delta\Omega$  stands for the distance between the midpoints of the partition intervals generated by points  $\Omega_k$ . Sequence  $\{\psi_k\}$  consists of *independent random phase-angles, uniformly distributed over  $[-\pi, \pi]$* . In the simulation procedure the required random variables are represented by properly generated pseudo-random numbers.

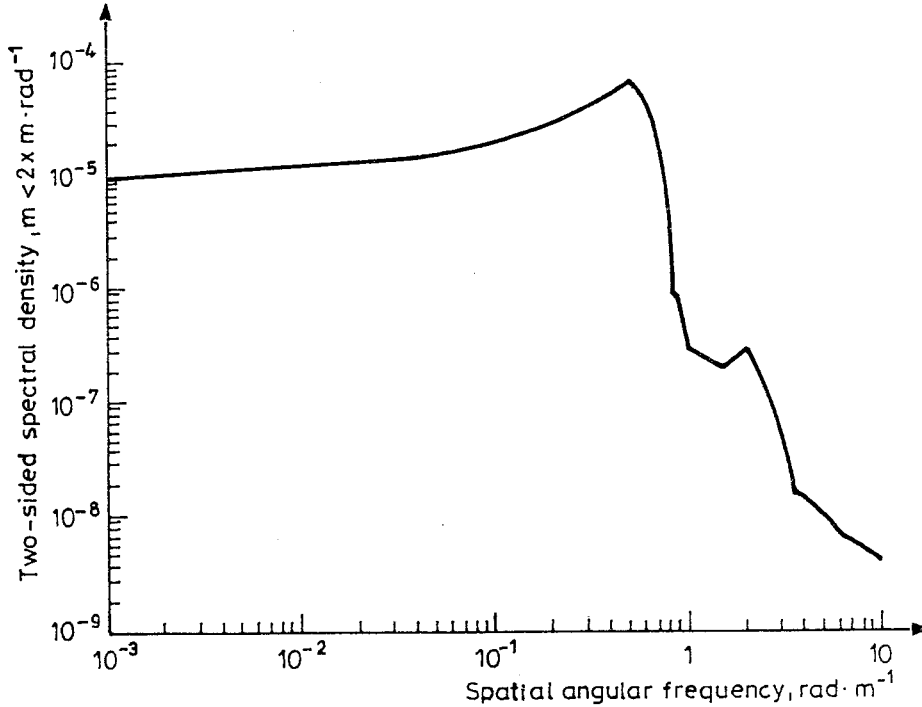


Fig. 8. Two-sided spectral density function of the vertical track irregularities

In Fig. 8 the spectral density function of a weakly maintained track is shown, while in Fig. 9 the realization function generated on the basis of the spectral density introduced is visualized.

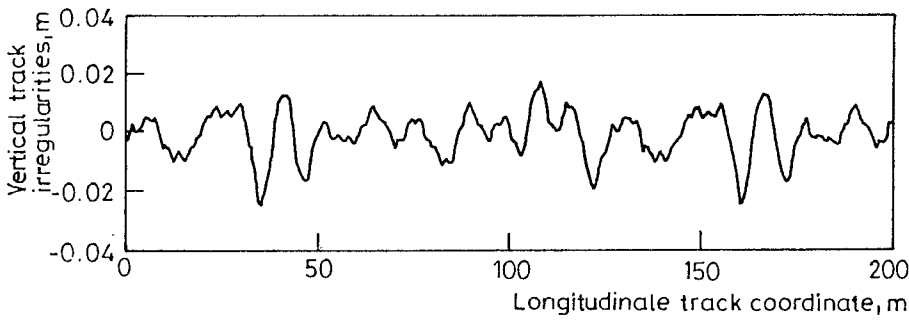


Fig. 9. Realization function of vertical track irregularities generated from spectral density function shown in Fig. 8

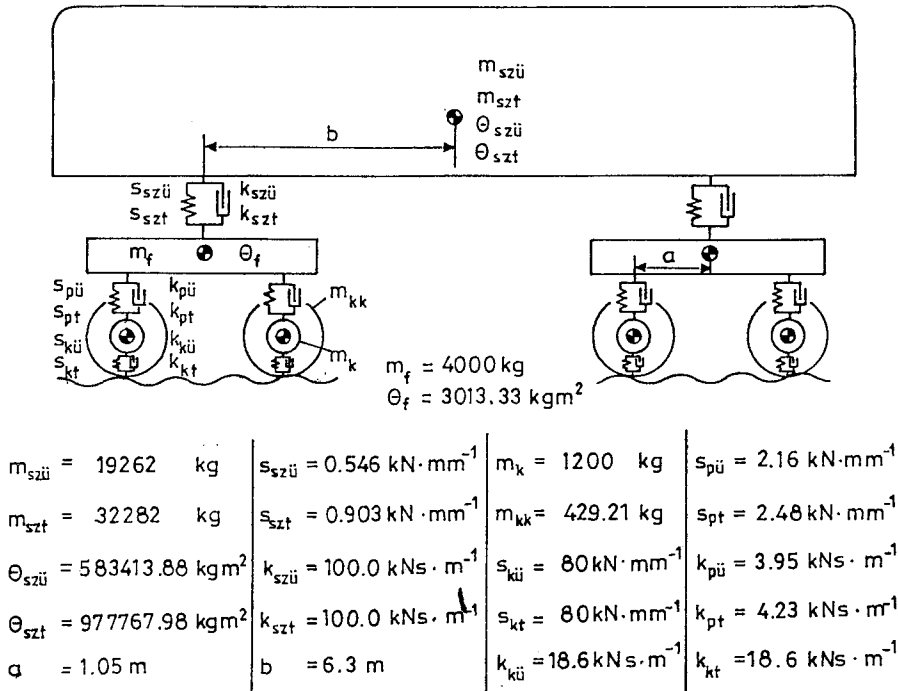


Fig. 10. Lumped parameter vertical in-plane dynamical model of the vehicle

In this way the track irregularities under each wheelset of the vehicle can be computed for each time step of pace 0.01 s when the train passes through

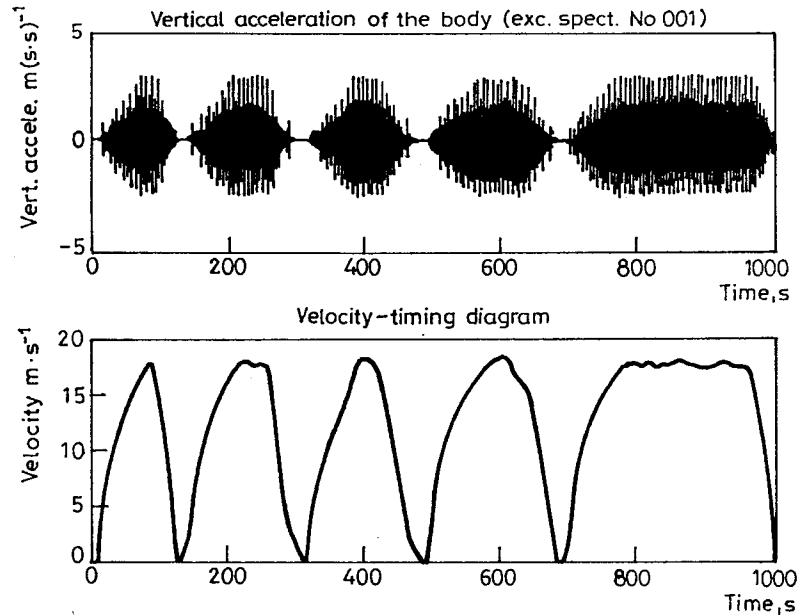


Fig. 11. Time history of the carbody acceleration belonging to the velocity – timing diagram shown in the lower part

a line section. The continuous vertical track irregularity excitation function  $u_1(t), u_2(t), \dots, u_4(t)$  can be obtained for the analysis of the vertical dynamics of the vehicle by using  $C_2$  spline interpolation on the discrete (sampled) track irregularity values obtained from the simulation of the train motion.

#### 4. Simulation of the Forced Vertical Vibrations of the Railway Vehicle

For the simplified analysis of the excited stochastic vertical vibrations of traditional four-axle railway vehicles a dynamical model of 10 degrees of freedom was constructed. As free coordinates the vertical displacement of the vehicle body, the bogies and the wheelsets, as well as the pitching angular displacements of the vehicle body and bogies were selected (see Fig. 10).

The time-dependent excitation effect of the vertical track irregularities is represented by vertical displacement excitations  $u_1(t), u_2(t), u_3(t), u_4(t)$  prescribed for the wheel treads. The set of motion equations describing the vertical and pitching vibrations are treated in the framework of the state-space method. The resulted first order set of differential equations is solved numerically in the time domain. In Fig. 11 the vertical acceleration function

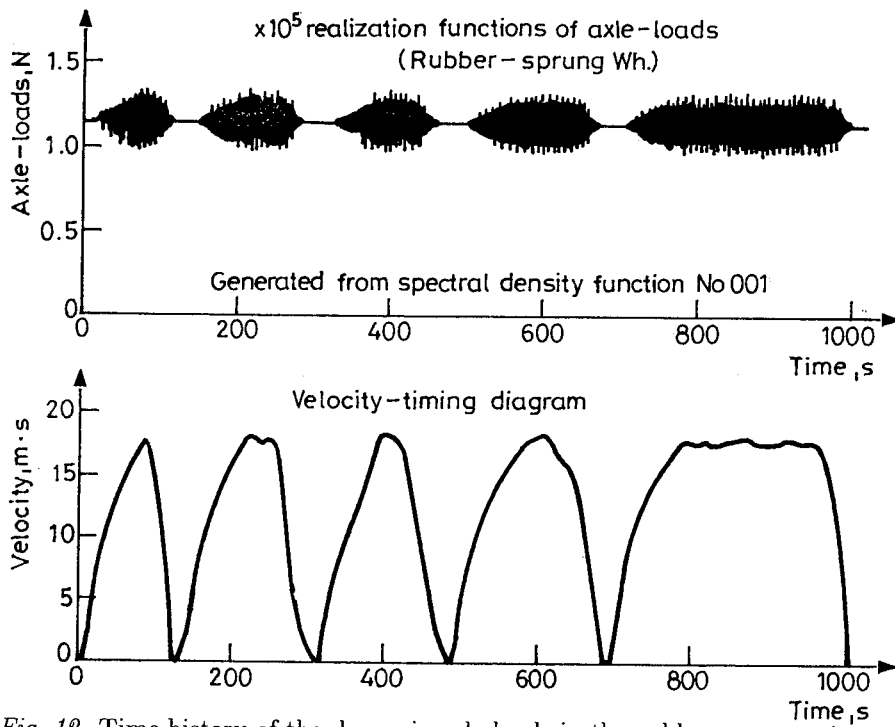


Fig. 12. Time history of the dynamic axle loads in the rubber sprung wheelsets

of the carbody gravity point is shown belonging to the irregularity function in Fig. 9, together with the speed - timing diagram characterizing the actual train motion considered.

The solution functions received for the velocities and displacements of the bodies in the model are substituted into formulae determining the connection forces arising in the linkages in the running gear and the suspension system. The time history of the vertical forces arising in the rubber-sprung wheelsets between the hubs and the sprung rings of the wheels is represented in Fig. 12.

In Fig. 14 the time history of the vertical forces transmitted by the secondary suspension system is shown.

In Fig. 13 the time history of the vertical forces transmitted by the primary pension system is visualized.

Based on the latter force - time functions the predicted load statistics of the running gear and the suspension system can be determined.

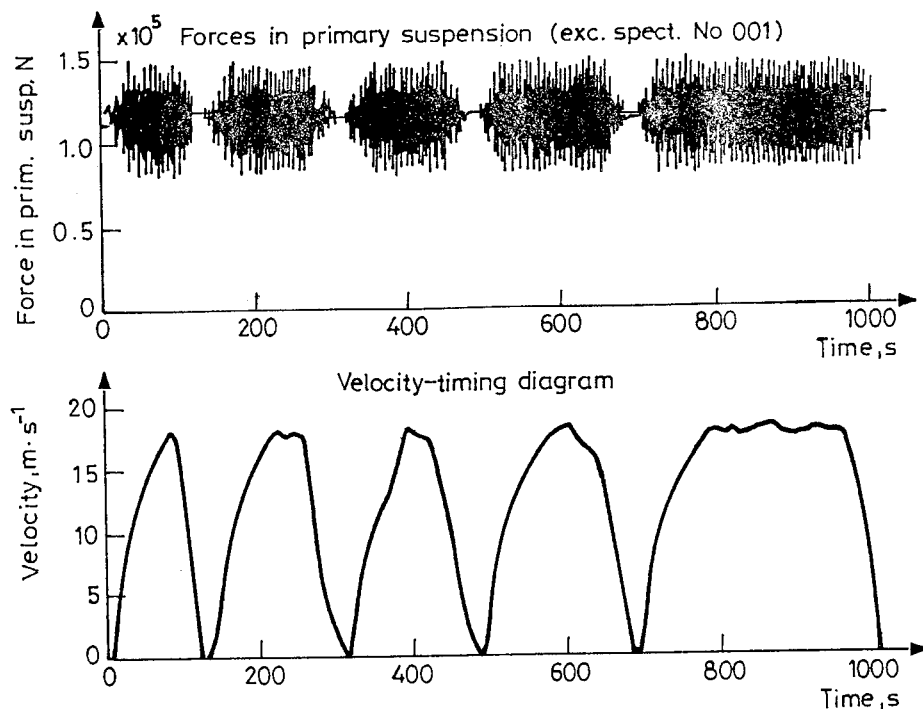


Fig. 13. Time history of vertical forces transmitted by the primary suspension system

### 5. Load Statistics

The operation-loading conditions are characterized by means of probability distribution approximating relative frequency histograms evaluated from the time history functions mentioned. The software elaborated for the automatic evaluation makes it possible either to illustrate on the screen, or to make printed documents. Also the mean values and empirical standard deviations are determined ensuring a proper description of the predicted future motion and loading conditions. The Gaussian probability density functions generated on the basis of the arithmetical mean and the empirical standard deviation computed from the time histories are included in the diagrams to ensure a preliminary (visual) normality test.

In Fig. 5 the relative frequency density histogram belonging to the computer-generated track irregularities plotted in Fig. 8 is shown.

In Fig. 16 the relative frequency density histograms of the vertical accelerations of the carbody over the front and rear king-pin linkages are plotted. The two diagrams are constructed by taking into consideration the



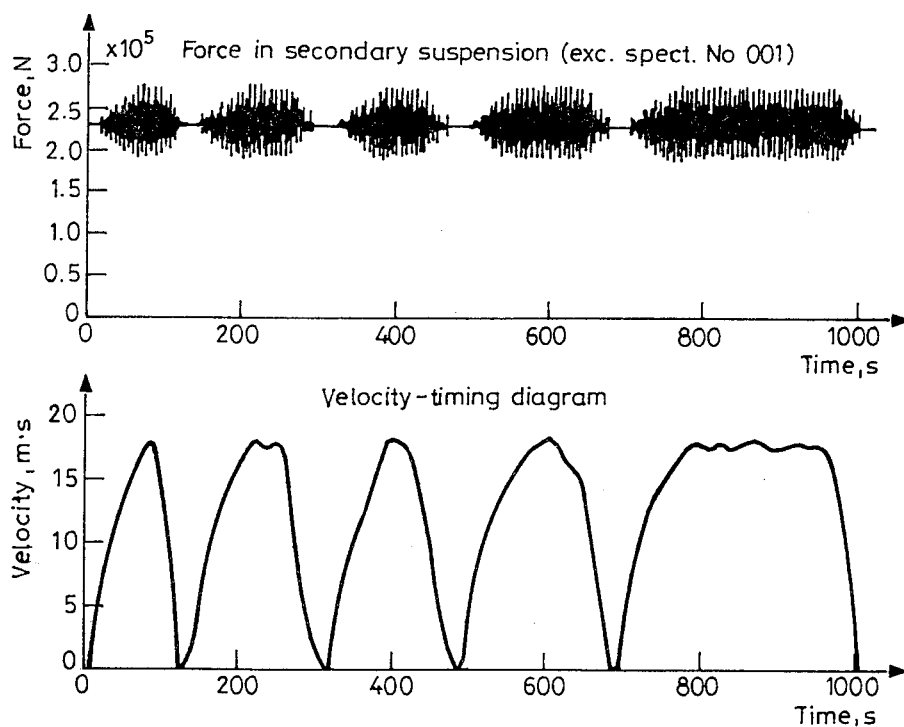


Fig. 14. Time history of vertical forces transmitted by the secondary suspension system

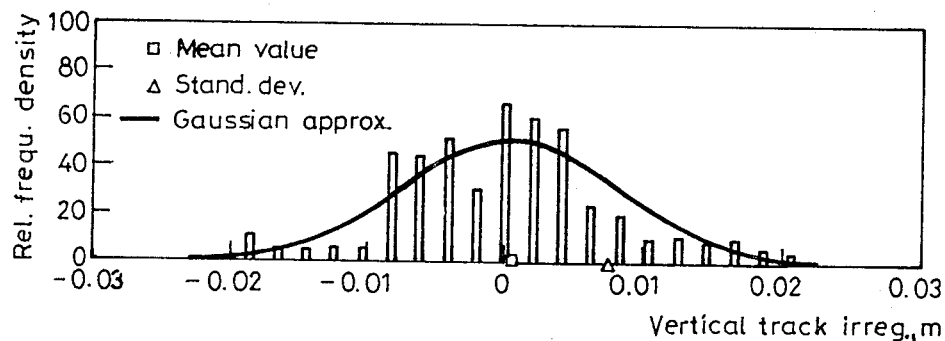


Fig. 15. Relative frequency density histogram of the vertical track irregularities

time history of the vertical acceleration of the carbody's gravity point and also the angular acceleration of the pitching vibrations of the carbody.

In Fig. 17 the four relative frequency density histograms of the vertical axle loads transmitted through the rubber springs (and the parallelly connected viscous dampers representing the internal energy dissipation in

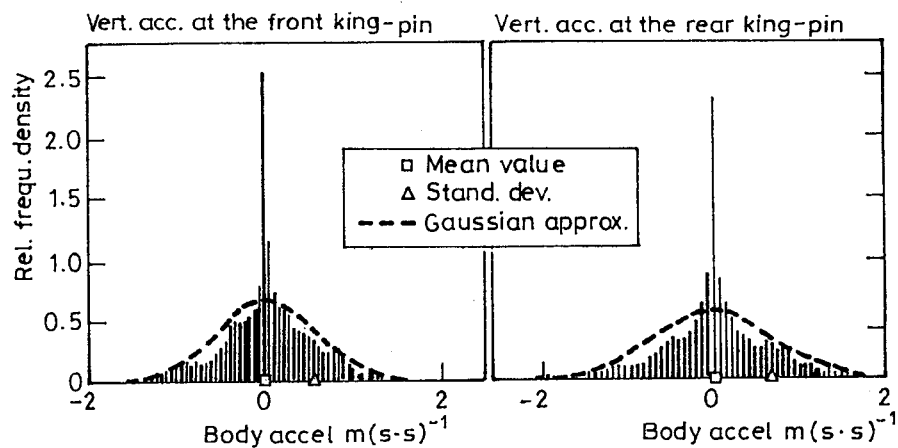


Fig. 16. Vertical accelerations on the carbody

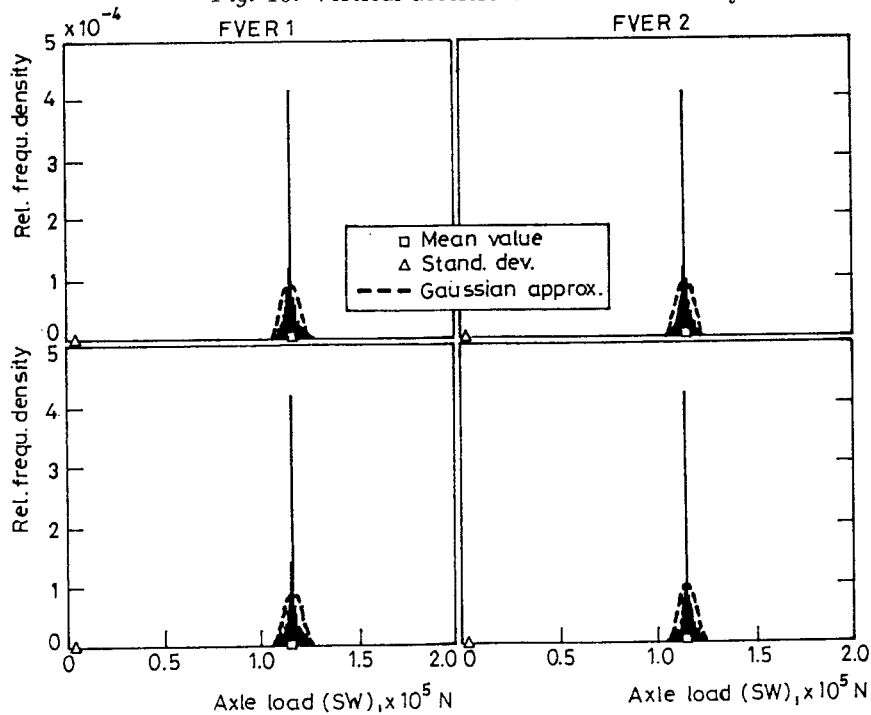


Fig. 17. Relative frequency density histograms of the vertical axle loads transmitted through the rubber springs

the rubber springs) built into the wheelsets are shown.

In Fig. 18 the four relative frequency density histograms of the vertical

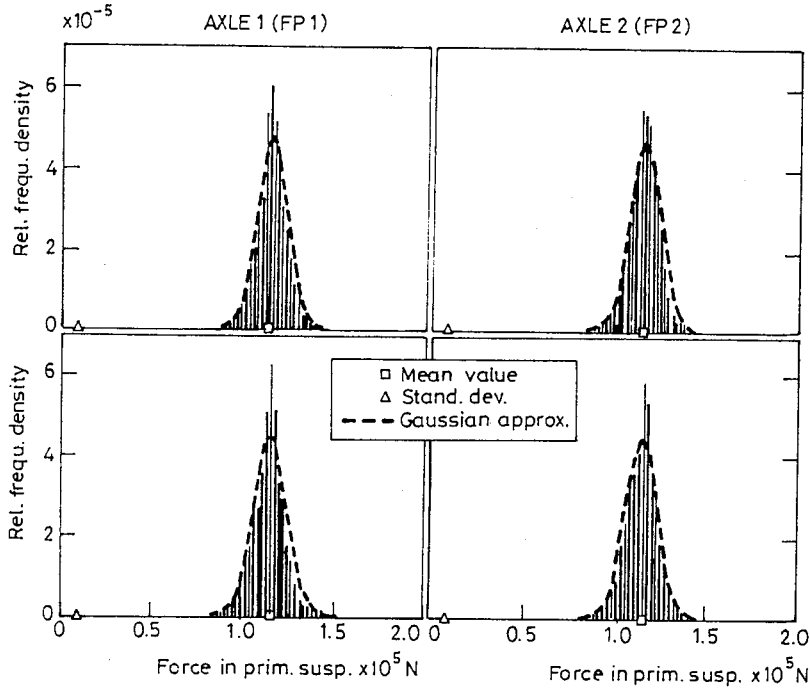


Fig. 18. Relative frequency density histograms of the vertical forces transmitted through the primary suspension system

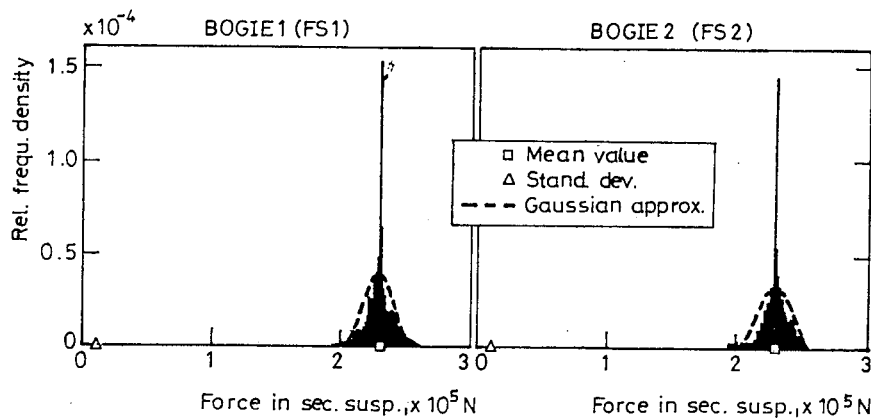


Fig. 19. Relative frequency density histograms of the vertical forces transmitted through the secondary suspension systems

forces transmitted through the primary suspension elements are plotted.

In Fig. 19 the two relative frequency density histograms of the vertical forces transmitted through the secondary suspension elements are shown.

Of course, further statistical characteristics, such as correlation functions, spectral densities, etc. of the load process can be determined.

## 6. Conclusions

- The elaborated simulation method makes it possible to analyze the dynamic loading conditions realizing in the components of the running and suspension gears of a railway vehicle planned for a specified railway line (railway network) *already in the period of designing*.
- The basic condition of the application of the method is to have accurate data about the inclination and curvature conditions of the railway line considered, and about the lengths of the transition curves and the radii of the circular arcs interconnecting the adjacent inclined sections in the vertical plane.
- It is also necessary to know the *spectral density function* globally characterizing the stochastic irregularities of the railway track in the framework of a weakly stationary model or the spectral density functions belonging to the individual sections of the track.
- The computation procedure gives the *elastic and dissipative forces arising in the structural connections of the running and suspension gears* ensuring a solid basis for the exact stress dimensioning by taking into account the expected loading conditions on the railway line or network considered.
- The elaborated computation method makes it possible *to optimize the system parameters of a vehicle* planned for operation on a given railway line or network by maximizing the objective functions formulated for the running comfort and safety under appropriate constraint conditions.

## References

- [1] ZOBORY, I.: Stochasticity in Vehicle Dynamics. *Proceedings of the 1st Mini Conference on Vehicle System Dynamics, Identification and Anomalies*, held at the TU of Budapest, 14–16 November, 1988, pp. 8–10.
- [2] ZOBORY, I.: Prediction of Operational Loading Conditions of Powered Bogies. *Vehicles, Agricultural Machines*, 1990, Vol. 37, Issue 10, pp. 373–376. (In Hungarian).
- [3] MICHELBERGER, P. – ZOBORY, I.: Operation Loading Conditions of Ground Vehicles – Analysis of Load History. *Proceedings ASME Winter Annual Meeting*, Dallas, 1990, pp. 175–182.
- [4] ZOBORY, I. – BÉKEFI, E.: On Real-Time Simulation of the Longitudinal Dynamics of Trains on a Specified Railway Line. *Proceedings of the 4th Mini Conference on Vehicle System Dynamics, Identification and Anomalies*, held at the TU of Budapest, 7–9 November, 1994, pp. 88–100.

## SIMULATION STUDY OF THE INFLUENCE OF INVOLUTE TIP RELIEF ON GEAR DYNAMIC BEHAVIOUR

János MÁRIALIGETI

Department of Machine Elements  
Faculty of Transportation Engineering  
Technical University of Budapest  
H-1521 Budapest, Hungary

Received: November 13, 1996

### Abstract

The tooth tip relief, as an intended departure from the normal involute profile is a common technics for the improvement of tooth contact characteristics. It is often used not only for avoiding tip contact, but especially in the case of long relief, to aim at better dynamic behaviour. For studying the dynamic characteristics of gear trains in the case of long relief, comparative computer simulations were carried out for a train with normal toothing and with tooth tip relief. The applied dynamical model and excitation characteristics are discussed. By simulating smooth acceleration processes at different nominal load conditions, resonance curves are generated and analysed in the case of ideal tooth geometry under real mesh conditions, i.e. the mesh irregularities at the beginning and points of contact, due to tooth deflections were taken into account. Dynamic behaviour at low specific load level is studied based on steady state rolling down simulations and resonance characteristics are discussed.

*Keywords:* gear train, tooth tip relief, gear dynamics, non-linear vibration, simulation.

### 1. Introduction

The vehicle transmissions in operation are subjected in general to randomly variable load conditions, characterised by considerable variations even in the load amplitude and in the frequency range. Tooth profile modifications in height direction, as the long tooth relief, see for example in [1], [2], which can improve considerably the tooth dynamic behaviour in a relatively narrow load range, are often used in vehicle transmissions, too. However, the operating load range is normally broader than the region, where the effect of the relief is optimum. Consequently, special care must be taken for the correct choice of the tip relief values and their height.

On *Fig. 1*, four successive positions of the same profile pair are shown on the pressure line for teeth with long relief. The points *A* and *E* are the beginning and end points of contact with normal profiles and  $\overline{AD} = \overline{BE} = \overline{KA_{l2}} = \overline{A_{l1}M} = p_b$ . Point *A<sub>l1</sub>* is the beginning, *A<sub>l2</sub>* is the end point of contact of the normal involute profile of gears 1 (upper) and 2, on the

diameters  $d_{1,2}$  respectively,  $p_b$  is the pitch on the base circle. The upper profile sections with thin line are the eliminated involute sections,  $C_{a1,2}$  are the relief values, respectively.

Considering the pinion and wheel in positions belonging to the normal profile, there is no contact in position at point  $A$ , because of the tip relief on wheel 1, but the foregoing profile pair at point  $D$  is in normal contact. In contact position at point  $K$ , the foregoing profile pair leaves just the contact, consequently on  $\overline{KA_{11}}$ , contact is only possible by rotating back gear 1. At position in point  $A_{11}$ , the original profiles are in contact, as for the gears with normal profile and that remains up to the position in point  $A_{12}$ . Passing  $A_{12}$  because of the relief on gear 2, contact is possible only with rotating back gear 1, being the succeeding profile pair in the interval  $\overline{KA_{11}}$ . In contact at point  $M$ , the succeeding profile pair enters in normal contact. So, on intervals  $\overline{KA_{11}}$  and  $\overline{A_{12}M}$ , contact is possible only with lag of the gear behind its nominal position. In other words, the contact ratio is less than one, introducing kinematic excitation.

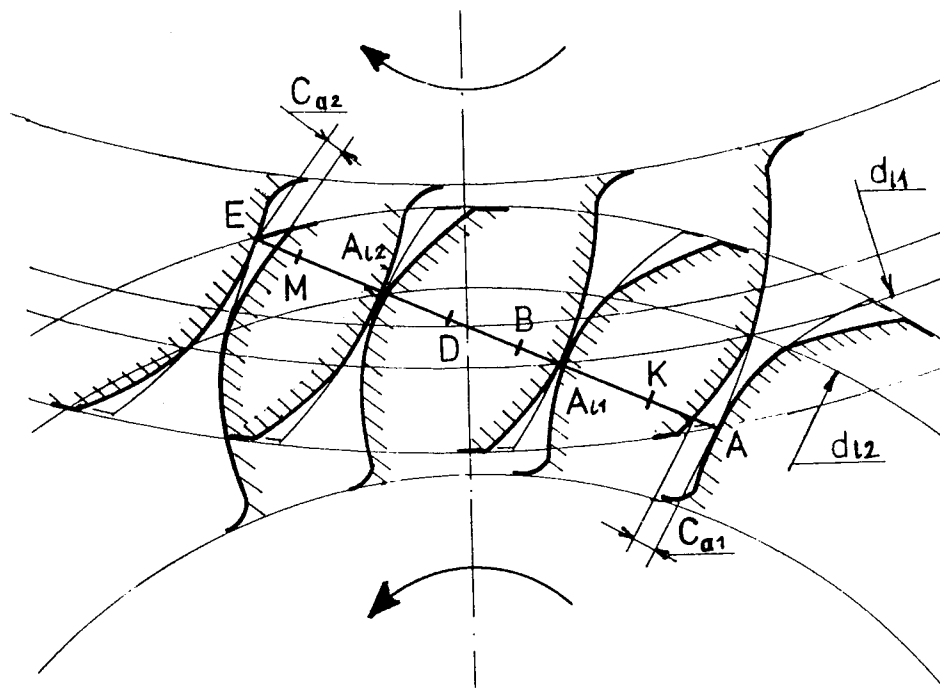


Fig. 1. Tooth contact on the pressure line for teeth with tip relief

## 2. The Dynamic Model

### 2.1. The Kinematic Excitation

For the simulation study a two mass system model is applied, with rotating masses, coupled by a spring system, as it is schematically represented on *Fig. 2*. The details of the spring system, replacing the real tooth contact, are described in detail in [3].

In the system on *Fig. 2*, the cam symbolises the resultant *kinematic excitation*, introduced by the tooth pairs, being in contact at a given contact point. The kinematic excitation is introduced by mesh irregularities due to the tooth deformations on one side, and profile relief and manufacturing errors on the other side. Consequently, for gears with ideal geometry the period of the kinematic excitation  $\Omega = 2\pi/z_1$ , where  $z_1$  is the number of teeth of the pinion. For gears with manufacturing errors,  $\Omega$  is the total rotation angle of the driver, rolling down during the realisation of all possible combinations of the profile pairs of the driver and the driven gear.

The description of the kinematic excitation can be conveniently handled by the *contact function*,  $\delta_j(\varphi_1)$  see e.g. in [3], [4] which gives the travel error of the driven gear, measured in length on the pressure line, at any driver angular position  $\varphi_1$ . The subscript  $j$  refers to the  $j$ th tooth profile pair combination.

*Fig. 3a* shows a series of contact functions for ideal normal gears, whilst on *Fig. 3b* contact functions for profiles with tip relief are represented. The curved parts at the *A* and *E* points symbolise the errors involved by mesh irregularities at entering into and leaving the contact. Taking into consideration the contact process on the pressure line discussed in *Fig. 1* and the fact that for profiles with long relief  $\varepsilon_\alpha < 1$ , the  $\delta(\varphi_1)$  *resultant contact function* has triangular shaped parts, where its value is not zero, see *Fig. 3b*.

### 2.2. Basic Dynamic Behaviour

The differential equations for the two mass system in *Fig. 2* are:

$$\begin{aligned} J_1 \cdot \ddot{\varphi}_1 + \left\{ \sum_{j=1}^n K_j \left( \Delta \dot{\sigma} - \dot{\delta}_j(\varphi_1) \right) \right\} r_{b1} + r_{b1} \cdot \hat{s}(\varphi_1; \Delta \sigma) \cdot \Delta \sigma &= T_1, \\ J_2 \cdot \ddot{\varphi}_2 + \left\{ \sum_{j=1}^n K_j \left( \Delta \dot{\sigma} - \dot{\delta}_j(\varphi_1) \right) \right\} r_{b2} + r_{b2} \cdot \hat{s}(\varphi_1; \Delta \sigma) \cdot \Delta \sigma &= -T_{21}, \quad (1) \end{aligned}$$

where  $\ddot{\varphi}_{1,2}$ ,  $\dot{\varphi}_{1,2}$ ,  $\varphi_{1,2}$ , are the twist angles of the masses and their time derivatives,  $K_j$  is the damping coefficient in the single tooth pair contact.

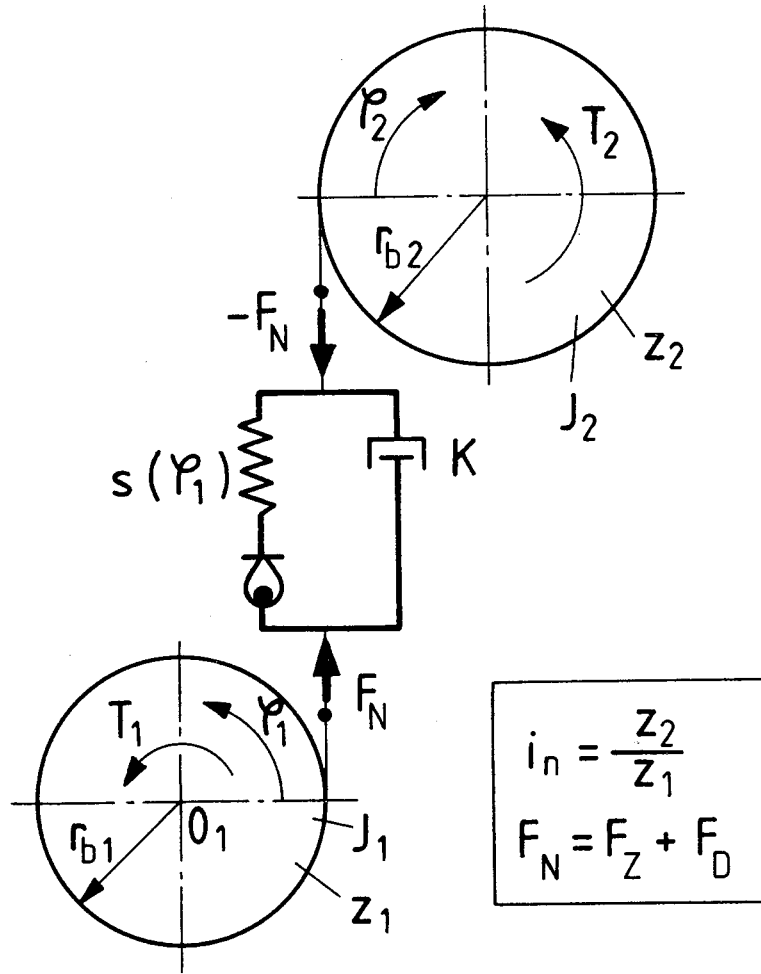


Fig. 2. Schematic two mass model. ( $J_{1,2}$  moments of inertia of the rotating masses,  $z_{1,2}$  number of teeth,  $T_{1,2}$  outer torques,  $\varphi_{1,2}$  twist angles,  $r_{b1,2}$  base circle radii,  $s(\varphi_1)$  tooth contact stiffness function,  $F_N$  resultant contact force on the pressure line,  $F_Z$  and  $F_D$  are the elastic and damping forces in contact,  $K$  damping coefficient.)

$\Delta\sigma = w_j + \delta_j$  is the instantaneous travel error, composed from the  $w_j$  tooth deflection and  $\delta_j$  contact function value for the tooth flanks actually in mesh, and  $\hat{s}(\varphi_1; \Delta\sigma)$  is the *reduced stiffness function* [4]. This latter multiplied with  $\Delta\sigma$  gives the actual elastic force, acting in the mesh. The



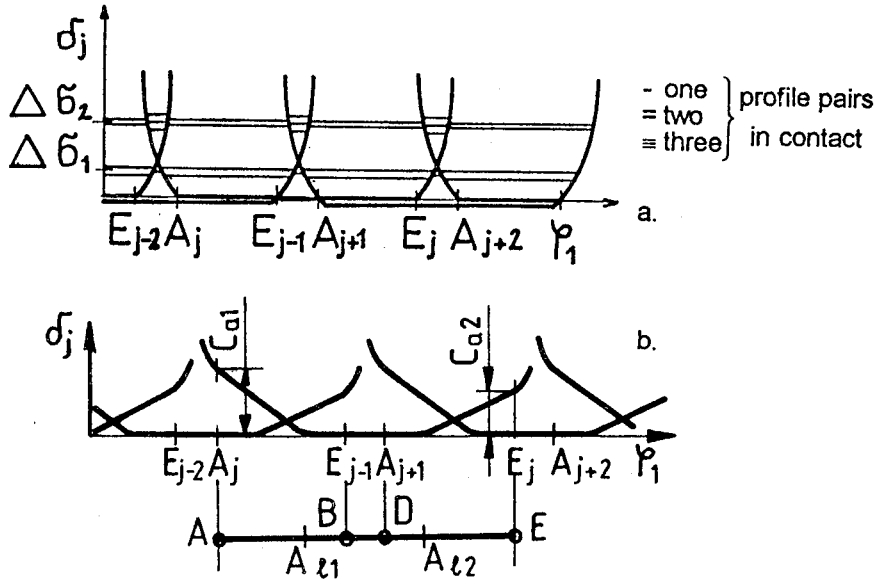


Fig. 3. Contact functions for ideal profiles (a) and with tip relief (b)

reduced stiffness function contains all excitation components, so it can be considered as the parametric excitation term in the system.

In general case, the reduced stiffness function can be written as the sum of its Fourier components  $C_k$ , with the  $C_0$  average value as follows:

$$\hat{s}(\varphi_1; \Delta\sigma) = C_0(\Delta\sigma) + \sum_{k=1}^{\infty} C_k(\Delta\sigma) \cdot \cos\left(\frac{2\pi}{\Omega} \cdot k\varphi_1 + \nu_k\right), \quad (2)$$

where  $\Omega$  is the basic angular period of the reduced stiffness function,  $k$  is the ordering number of the Fourier components, and  $\nu_k$  the phase angle.

One can distinguish the  $\hat{s}(\varphi_1; \Delta\sigma)$  stiffness function, which is the sum of single tooth pair stiffnesses being actually in contact; consequently it differs from the reduced stiffness function. The integral mean value (average) of the stiffness function is called as gear engagement spring stiffness  $c_\gamma$ . In the case of linear single tooth pair stiffness characteristic (i.e. force-deflection curve at a given contact position) at each contact point and ideal tooth geometry, its value is approximately constant. However, in the case of toothings with tip relief or with manufacturing errors or/and with non-linear single tooth pair stiffness characteristic, its value is load (i.e.  $\Delta\sigma$ ) dependent and will be marked as  $\tilde{c}_\gamma$ .

The system of Eq. (1) with the excitation term (2) describes a rheo-nonlinear type vibration [5].

The basic vibration properties of such type of vibrations for one mass system with harmonic excitation can be studied by applying the stability chart, see ex. [5].

Assuming ideal tooth geometry, without manufacturing error, the tooth frequency  $f_z = z_1 \cdot n_1 = z_1 \cdot \omega_1 / 2\pi$ ,  $\varphi_1 = \omega_1 \cdot t$ , where  $\omega_1$  and  $n_1$  are the input angular frequency and rotation speed, respectively, the period of the excitation  $\Omega = 2\pi/z_1$  and the *tooth angular frequency*  $\omega_z = z_1 \cdot \omega_1$ , being the basic excitation angular frequency. The system eigenfrequency,  $\omega_s = \sqrt{c_\gamma/m}$ , see ex. [5], [2] where  $m$  is the reduced mass of the one-mass system. As it is known from the stability chart, unstable, or resonance points develop, if

$$\frac{\omega_s^2}{\omega_z^2} = \left(\frac{\nu}{2}\right)^2, \quad \nu = 1, 2, \dots, \infty. \quad (3)$$

Rearranging Eq. (3), unstable vibration develops, if the excitation frequency,  $\omega_z = 2\omega_s/\nu$ . Fig. 4 shows schematically the resonance curve for such a system with damping, on the tooth angular frequency with the vibration amplitude ratio  $\Delta\sigma_{\max}/\Delta\sigma_{\text{stat}}$  on the vertical axis.

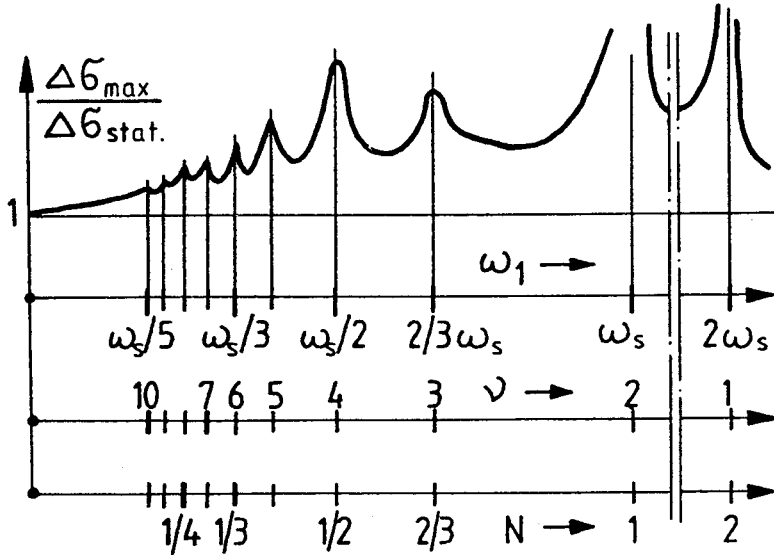


Fig. 4. Schematic resonance curve

Considering a complex excitation function with harmonic components of  $k = 1, 2, \dots, \infty$ , the angular frequency of the  $k$ -th harmonic components will be  $\omega_z \cdot k$ . Replacing this value in Eq. (3) as excitation frequency, rearranging the equation and introducing  $\omega_z(\nu^{(k)})$ , as the tooth frequency at which the  $\nu$ -th order resonance point of the  $k$ th order harmonic excitation component develops, one can write:

$$\omega_z(\nu^{(k)}) = \frac{2\omega_s}{k \cdot \nu}, \quad k = 1, 2, \dots, \infty, \quad \nu = 1, 2, \dots, \infty. \quad (4)$$

From Eq. (4), the following can be concluded:

- since  $k \geq 1, \nu \geq 1$ , unstable points develop only at excitation frequencies equal to or less than  $2\omega_s$ ,
- since  $k$  and  $\nu$  are whole numbers, their product will be whole, and in turn, all whole numbers can be produced as the product of two whole numbers, consequently each whole number can serve as divisor,
- one can find unstable point at each excitation frequency which is  $2\omega_s$  divided with a whole number,
- for all  $\nu^{(k)}k \geq 1, \nu \geq 1$  with  $k \cdot \nu = \text{const.}$ , the resonance points are at the same excitation frequency.

However, in the presence of damping, as it is in practice, the higher order unstable points tend to lose of importance.

In the gearing technics, a dimensionless frequency ratio number  $N$  is introduced [2], for the marking of the different resonance points, as follows:

$$N = \frac{\omega_z}{\omega_s} = \frac{z_1 \cdot \omega_1}{\omega_s} = \frac{2}{\nu}, \quad \nu = 1, 2, \dots, \infty, \quad (5)$$

so unstable resonance points can develop at  $N = 2, 1, 2/3, 1/2, \dots$ . The resonance at  $N = 1$  is called as main resonance point. For cases, in which the average stiffness  $\tilde{c}_\gamma$  is load dependent, the frequency ratio depends on the load, too, so in that case the symbol  $\tilde{N}$  will be applied.

### 3. System Behaviour of Gear Trains with Normal Toothing

For studying the system behaviour, an electric locomotive main drive train is applied, with the following basic parameters:  $z_1 = 53, z_2 = 65, m = 12$ . The pinion and gear are constructed as hub, web and rim, which involves a decrease of the theoretical tooth stiffness, see ex. [6]. Two stiffness variants were applied, one with the theoretical stiffnesses by Weber – Banaschek [2] with linear single tooth pair stiffness function characteristic, coded as WBlin, and the other with taking into consideration the rim influence by [6] and with non-linear single tooth pair stiffness characteristic by [7], coded as WBHKp.

For characterising the system behaviour, continuous rolling down processes by smooth acceleration were simulated and the tooth contact force dynamic factor  $V_\Sigma$  was calculated:

$$V_\Sigma = \max_{\gamma} \{V_\Sigma(\varphi_1)\}; \quad V_\Sigma(\varphi_1) = \frac{\sum_{j=1}^n \frac{F_{N_j}(\varphi_1)}{b}}{\frac{F_N}{b}}, \quad (6)$$

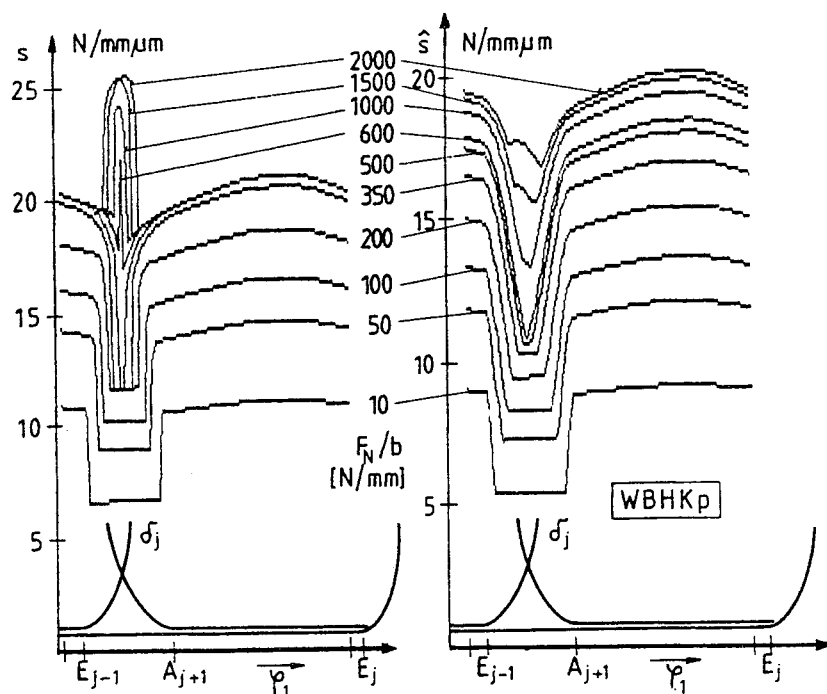


Fig. 5. Stiffness  $s(\varphi_1; \Delta\sigma)$  and reduced stiffness  $\hat{s}(\varphi_1; \Delta\sigma)$  functions for ideal, normal tooth profiles

where  $F_N/b$  is the total nominal specific load in contact, (due to the nominal outer load),  $F_{N_j}/b$  is the real, dynamical load on the  $j$ th profile pair,  $n$  being the number of teeth in contact, and  $\gamma$  is the rotational angle of the pinion, corresponding to one tooth mesh.

On Fig. 5 stiffness and reduced stiffness functions are shown, with the corresponding contact functions for gear train with normal profile. Expressed load dependence is caused by the mesh irregularities and the beginning and end points of contact due to the elastic tooth deflections and by the non-linear single tooth pair stiffness characteristic [7], coded as WBHKp.

Fig. 6 represents the resonance curves for different specific load values. On Fig. 6a, small damping coefficient is applied with backlash  $h$ , allowing the development of the resonance points. For  $N = 1, 1/2, 1/3$  and  $1/4$  the tooth flanks separate (where  $V_\Sigma = 0$ ), and non-linear resonance develops. That is why their location is slightly lower as it is previewed by the marked  $N$  values. On Fig. 6b, c, d normal damping is applied for case WBlin, resulting considerably lower load elevations in the resonance points. However, at  $N = 1$  and  $1/2$ , and at low specific load value, tooth flank separation occurs, involving the decrease of the resonance pick location.

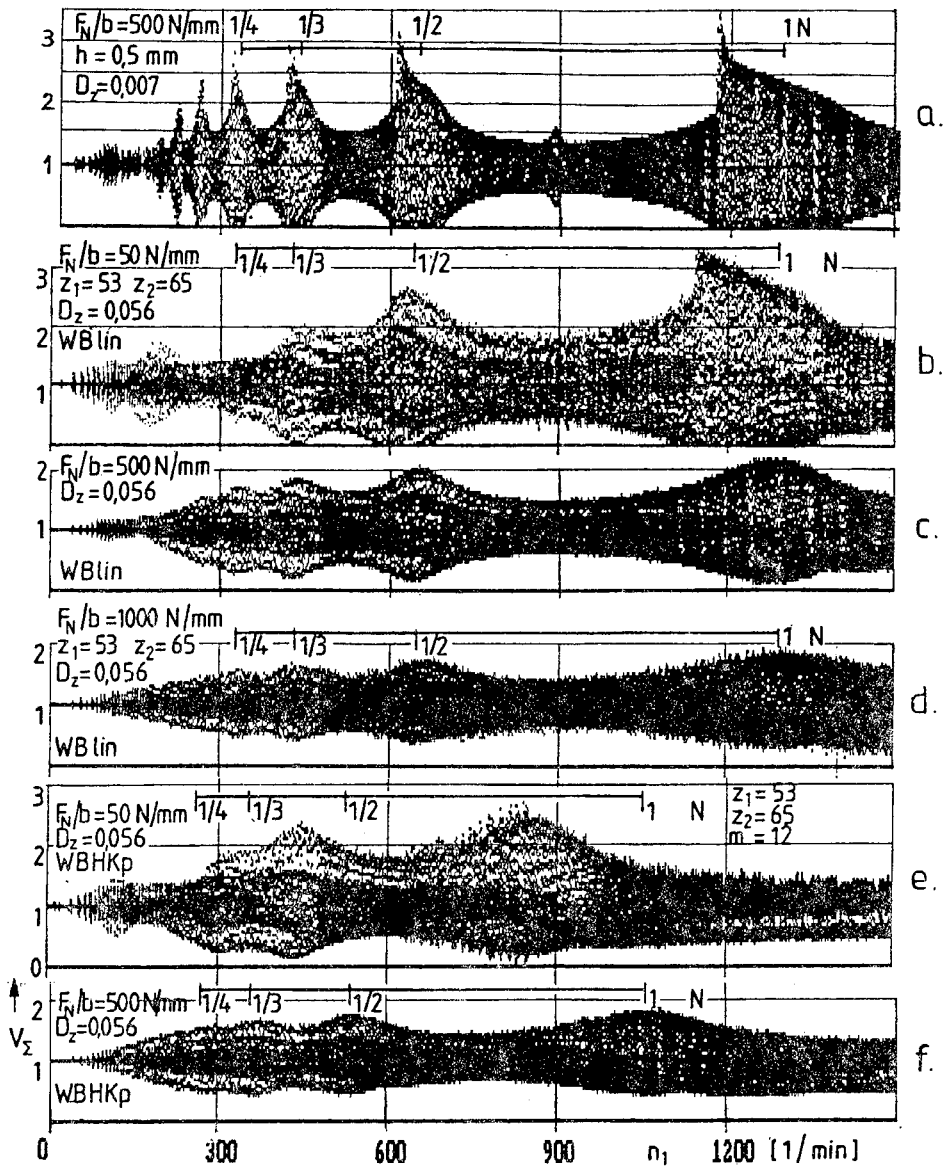


Fig. 6. Resonance curves in the case of ideal, normal tooth profiles

At higher loads regular resonance locations develop, without tooth flank separation. One can state that, at increasing load, the dynamic forces tend to decrease slightly, in agreement with experimental results. The general vibration shape changes only slightly.

On Fig. 6e, f the same system is represented, with lower single tooth

stiffness values and non-linear single tooth pair stiffness characteristic by *Fig. 5*. The general vibration shape remains similar, however, the resonance points move towards the lower input speeds. The reason of that is the smaller average stiffness. The difference between the theoretical  $N$  location and the real one can be explained by the fact that the beginning part of the single tooth pair stiffness function is progressive, with lower stiffnesses [7] and this is not taken into consideration in the calculation of  $N$ , determined with  $c_\gamma$ . Since the single tooth pair stiffness characteristics at fixed contact positions are not linear, expressed load dependence can be found on the resonance curves, see *Fig. 6e* and *f*.

Considering the curves on *Fig. 6*, in the case of linear single tooth pair stiffness characteristic, slight load dependence of the vibration shape and slight dynamic factor variation presents itself at different nominal loads, which is the result of the mesh irregularities at the points  $A$ , i.e. entering into, and  $E$ , i.e. leaving the contact of a given profile pair. For non-linear single tooth pair stiffness function, differences can be found even for vibration shape and dynamic factors.

#### 4. System Behaviour of Gear Trains with Profile Relief

##### 4.1. Contact Properties in the Case of Profiles with Tip Relief

In the case of tip relief, the number of tooth pairs in contact varies not only in the function of contact position, but it depends on the applied load as well. Let us consider the contact applying the contact functions, *Fig. 7*.

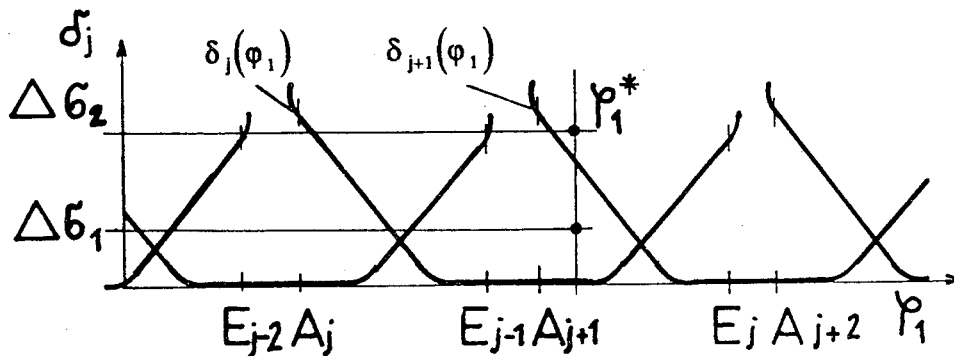


*Fig. 7.* Contact analysis based on contact functions

Assuming a given travel error due to a given load  $\Delta\sigma_1 = \text{const.}$  and  $\Delta\sigma_2 > \Delta\sigma_1$ , one can detect the number of teeth in contact at any position  $\varphi_1$ . At  $\varphi_1^*$  e.g.  $\Delta\sigma_1 > \delta_j(\varphi_1^*)$ , so the profile pair  $j$  is already in contact and profile pair  $j+1$  did not enter into contact, whilst at  $\Delta\sigma_2$ , being

$\Delta\sigma_2 > \delta_j(\varphi_1^*)$ ,  $\Delta\sigma_2 > \delta_{j+1}(\varphi_1^*)$ , both are in contact. The contact ratio, interpreted on geometrical bases, is not applicable for the following of this phenomenon. However, introducing the real, load dependent contact ratio  $\varepsilon_t$ , by the following definition:

$$\varepsilon_t(\Delta\sigma) = \frac{1}{\Phi} \sum_{j=1}^n \int_{\Phi} I_j d\varphi_1 \geq 1, \quad (7)$$

where  $\Phi$  is an arbitrary angular interval on  $\varphi_1$ , and  $I_j$  is an indicator function:

$$I_j(\varphi_1; \Delta\sigma) = \begin{cases} 1 & \text{if } \Delta\sigma > \delta_j(\varphi_1), \\ 0 & \text{if } \Delta\sigma \leq \delta_j(\varphi_1), \end{cases} \quad (8)$$

one can calculate the average number of teeth, being in contact at any  $\Delta\sigma$ , i.e. at any load,  $F_N/b$ .

#### 4.2. Excitation Properties

Since the contact conditions for profile with tip relief are load dependent, it is straightforward, that stiffness functions and reduced stiffness functions, the latter being responsible for the excitation, are load dependent, too. *Fig. 8* represents the stiffness and reduced stiffness functions,  $s(\varphi_1; \Delta\sigma)$  and  $\hat{s}(\varphi_1; \Delta\sigma)$ , respectively, for the case of non-linear single tooth pair stiffness characteristic, WBHKp. For case of WBlin, the curve shapes are similar.

The main Fourier components  $C'_k = C_k/C_0$  of the excitation functions on *Fig. 9* reflect its strong variation. (The continuous lines are applied only for the sake of the better visualisation.)

#### 4.3. Resonance Curves

*Fig. 11* represents the resonance curves for profiles with tip relief in the case of two different single tooth pair stiffness characteristics. One can detect the strong nonlinear behaviour as the nominal load varies and the important differences related to the resonance curves on *Fig. 6*, for normal profiles. The general shape of the curves is similar for both stiffness cases, however, the dynamic load values at individual operation points differ considerably.

Especially for the linear single tooth pair stiffness characteristic case, at specific load  $F_N/b = 200$  N/mm and lower, the tooth flanks separate practically on the whole region. In both cases, the main resonance regions are displaced towards the lower input speed values. At small load levels, the unstable regions belonging to different  $N$  or  $\tilde{N}$  values do not separate in a clear manner.

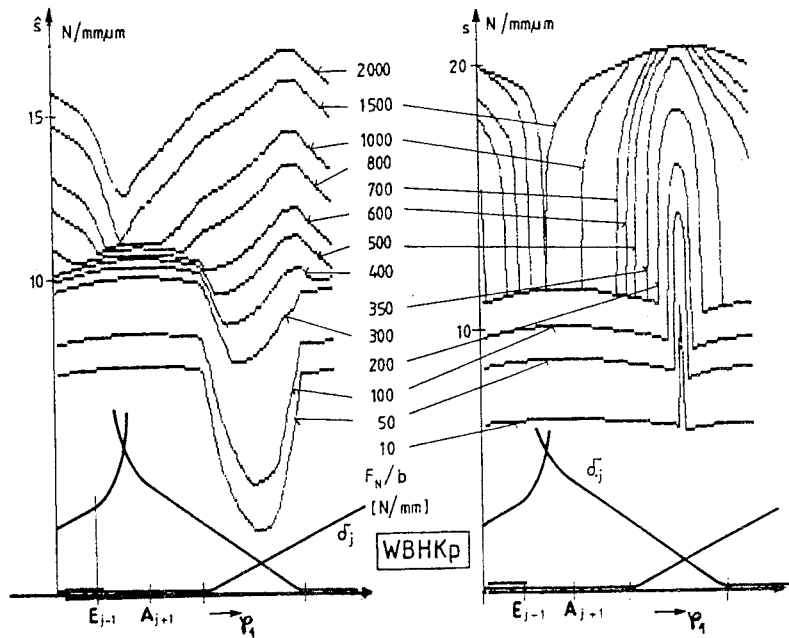


Fig. 8. Stiffness  $s(\varphi_1; \Delta\sigma)$  and reduced stiffness  $\hat{s}(\varphi_1; \Delta\sigma)$  functions for ideal tooth with tip relief

Fig. 10 shows the variation of the load dependent gear engagement spring stiffness values  $\tilde{c}_\gamma$ , and the variation of the real contact ratio  $\varepsilon_t$ . The  $\tilde{N}$  values on Fig. 11 are calculated with these  $\tilde{c}_\gamma$  values, showing strong variations as the load varies.

On the resonance curves of WBlin, two different non-linear resonance characters can be detected. At specific load levels of  $F_N/b = 50, 100, 200$  N/mm, the unstable regions are of nonlinear softening type. As namely the vibration amplitudes increase, the length of the angular intervals without contact (tooth flank separation) increase, too, consequently the average stiffness of the system which develops during the vibration decreases. In spite of that, the main resonance region at  $F_N/b = 350$  N/mm, one can find a non-linear resonance of hardening type. In that case, the increasing vibration amplitudes arrive in greater stiffness regions, and fall down after. In other unstable regions normal curve shapes develop.



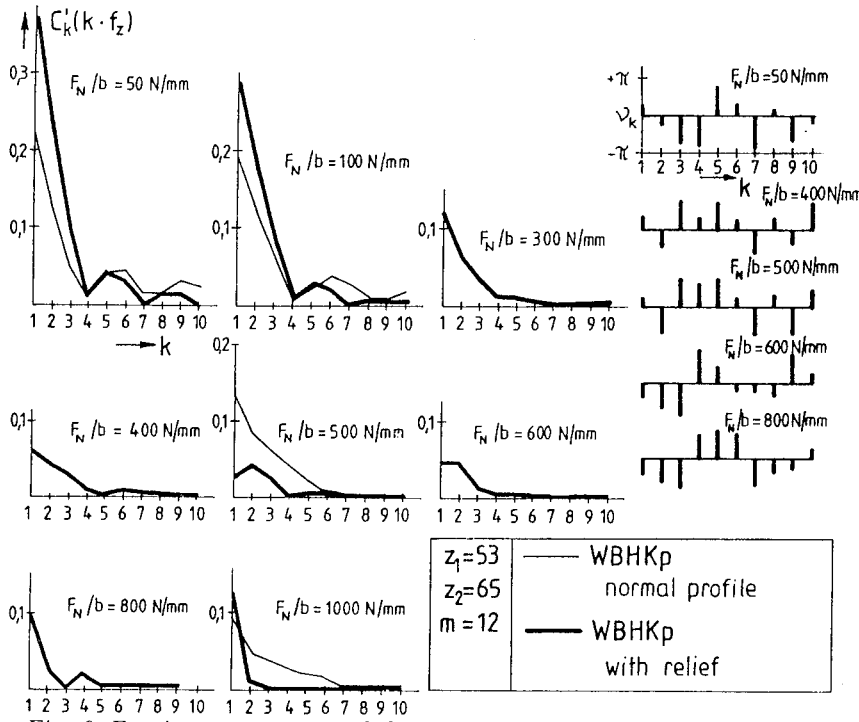


Fig. 9. Fourier components of the reduced stiffness functions of Fig. 8

With increasing specific loads  $F_N/b$ , the vibrations, i.e. the dynamic force elevations tend to smooth, and optimum region can be identified at about  $F_N/b = 700$  N/mm for WBlin, and  $F_N/b = 500$  N/mm for WBHKp. These values are in good agreement with the location of the optimum found with quasi static rolling down [4]. At higher specific loads, only the main resonance at  $\tilde{N} = 1$  becomes important, on other regions the vibrations remain reduced.

Comparing this behaviour to that with normal tooththing, important differences can be stated. At lower specific loads, the dynamic behaviour of gears with relief is strongly unfavourable, whilst at higher loads, optimal load interval can be found.

As consequence, one can resume that the dynamic behaviour of gears with long tooth tip relief differs considerably from that with normal one. Strong non-linear behaviour develops and optimum region can be identified. The influence of the single tooth pair stiffness characteristic has important influence on the dynamic behaviour and the location of the optimal region.

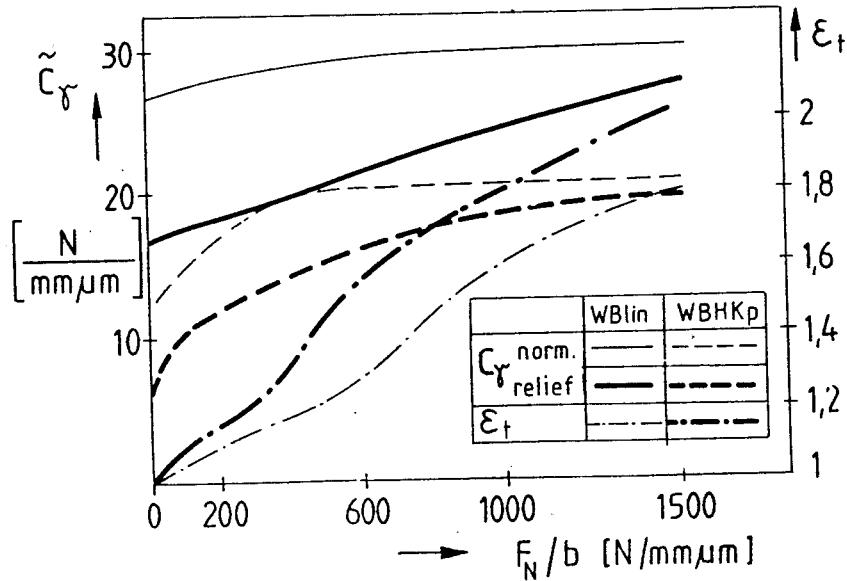


Fig. 10. Variation of real contact ratio and gear engagement stiffness in the function of the specific load

### 5. Analysis of the Vibrations at Lower Specific Load Values

As the resonance curves in Fig. 11 at lower specific load levels indicate, the individual resonance regions fall together, resulting quite important dynamic factors and tooth flank separations on important input speed interval. For the more detailed analysis of these vibrations, real tooth load functions were generated, permitting the study of the contact conditions on the teeth. At some constant input speed value, continuous rolling down was simulated at load level  $F_N/b = 50$  N/mm and tooth contact force dynamic factors by Eq. (6), and single tooth force dynamic factors  $V_F(\varphi_1) = (F_{Nj}/b)/(F_N/b)$  for the individual tooth pairs were generated. On Fig. 12 at each input speed, the upper curve is the total contact force dynamic factor variation during engagement and the curves below are the contact force dynamic factor variations for the single tooth pairs. In some cases only one tooth pair contact develops, consequently one curve is sufficient. The marking on the upper diagrams corresponds to the pitch points.

In all cases, the length of the represented angular interval  $\varphi_1$  is equal to the real vibration period.

Based on the curves WBlin, the following can be concluded:

- at  $n_1 = 180/\text{min}$ , the period of the response vibration is the triple of

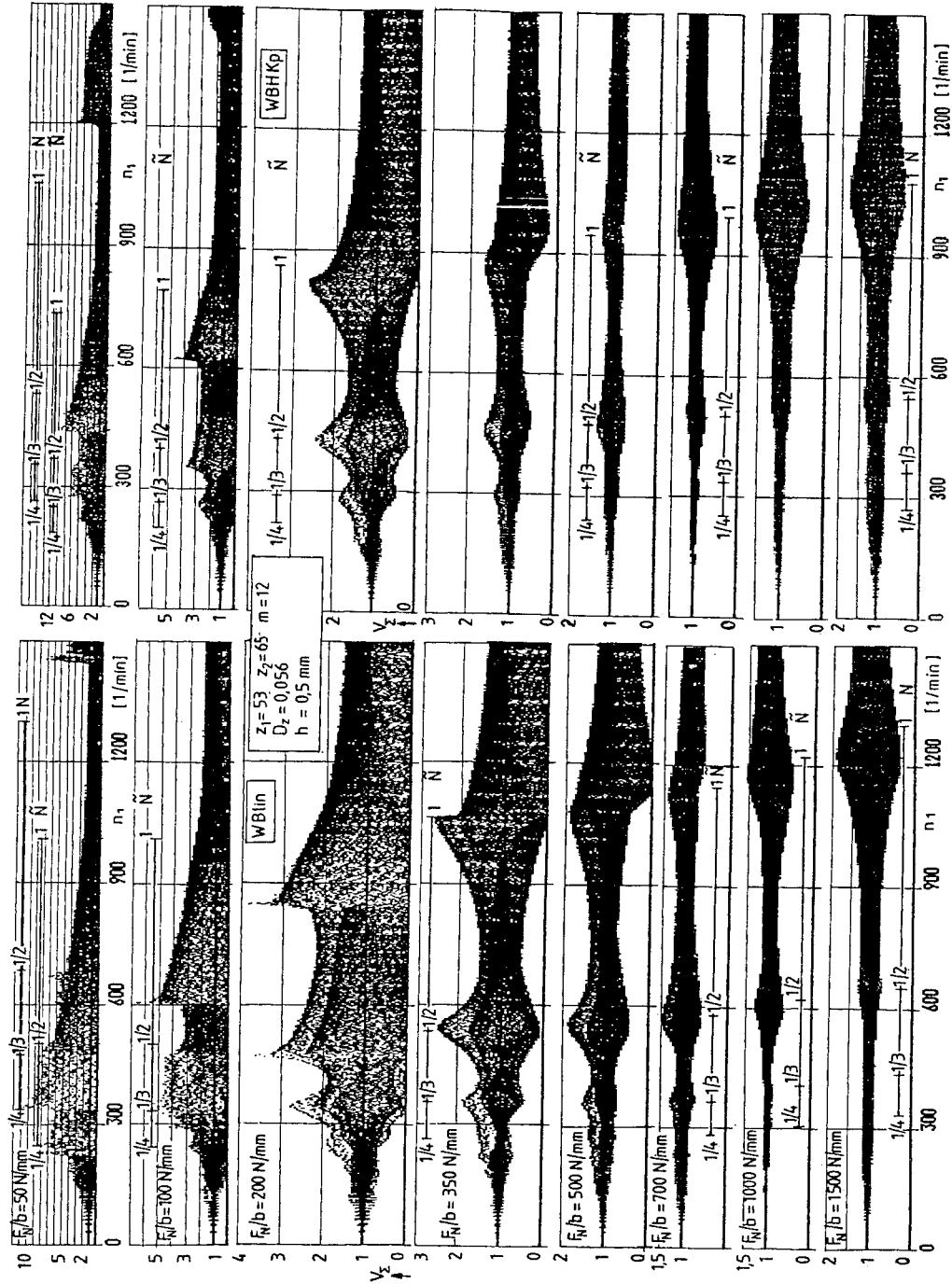


Fig. 11. Resonance curves for profiles with tip relief

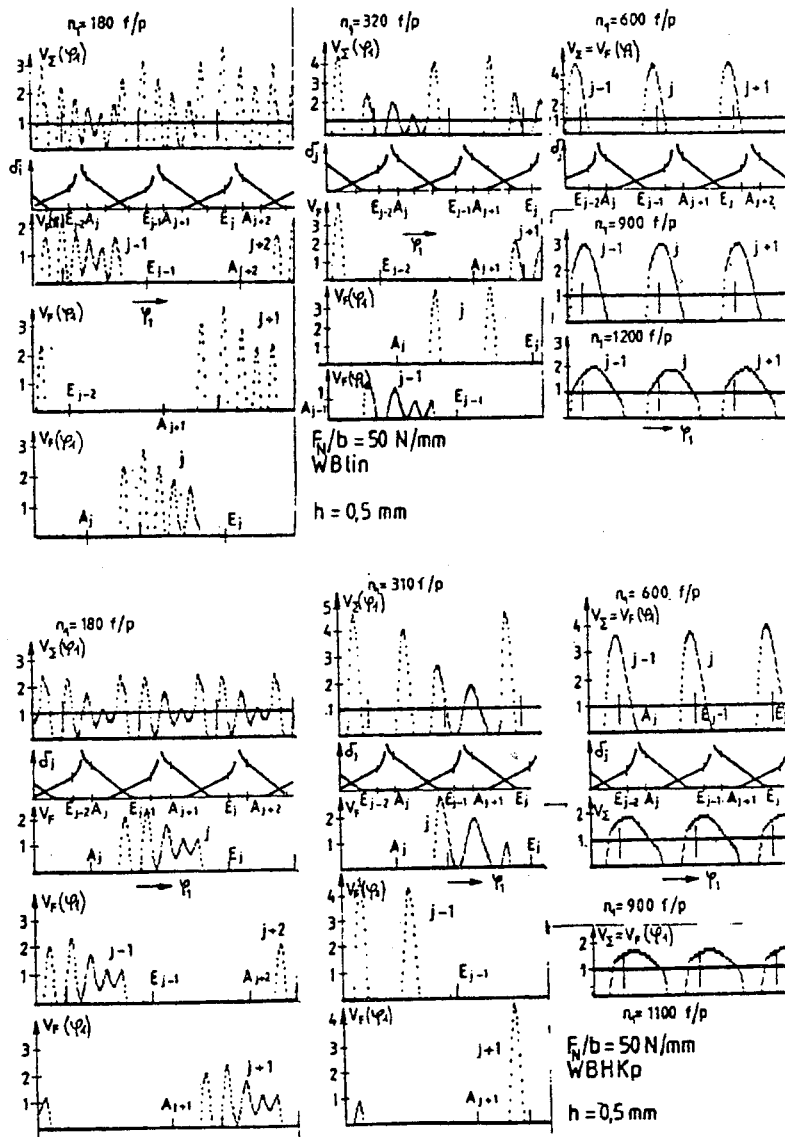


Fig. 12. Contact force and single tooth force dynamic factors at given constant input speeds, for two different single tooth pair stiffness values

the period of the excitation (being equal to the period of one pitch length) and limited tooth flank separation zones develop,

- at  $n_1 = 320/\text{min}$ , one can find a double period response vibration, with important tooth flank separation zones,
- at  $n_1 = 600/\text{min}$ , the period of the vibration equals the period of the excitation and there is only one tooth pair contact, around the pitch circle, so the length of angular intervals with zero force (tooth flank separation) are important,
- at  $n_1 = 900, 1200/\text{min}$ , the basic vibration shape remains similar, with increasing one tooth pair contact zones.

For the non-linear single tooth pair stiffness case, WBHKp, similar response vibrations are found, however, the contact force elevations are considerably reduced.

As it was seen on resonance curves of *Fig. 11* at low load level, the real unstable regions displace to smaller speeds and do not correspond of the theoretical  $\tilde{N}$  values. The reason of that is the development of the tooth flank separations on more or less long angular intervals, leading to the softening of the system, i.e. with 'contact intervals' without contact, so with zero stiffness.

Based on the contact force functions on *Fig. 12*, one can identify the real stiffness values of the system at each contact point, with zero stiffness on the zero load intervals. Determining the integral mean on one vibration period of the 'realised stiffness function', one can find a more softer system, as it should be without tooth flank separations, i.e. with tooth contact during the whole vibration.

*Table 1* contains for the two stiffness cases at the given speeds, the 'real' gear engagement stiffness  $\tilde{c}_\gamma$ , and the input speeds  $\tilde{n}'_{1s}$ , which introduces the excitation involving the main resonance, i.e. the resonance to  $N = 1$ .

*Table 1.* Tooth engagement spring stiffness values and input speeds to  $N = 1$

$n_1$ [1/min]	WBlin		WBHKp	
	$\tilde{c}_\gamma$ [N/mm · μmm]	$\tilde{n}'_{1s}$ [1/min]	$\tilde{n}'_{1s}$ [N/mm · μmm]	$\tilde{n}'_{1s}$ [1/min]
180	11.54	866	8.24	702
310	—	—	5.87	593
320	8.84	727	—	—
600	5.04727	549.4	—	—
900	8.84	727	4.19	500
1100	—	—	7.17	655
1200	11.7	837	—	—

Fig. 13 represents the excitation frequency values corresponding to the resonance at  $N = 1$ , expressed in input speed  $\tilde{n}'_{1s}$ , in the function of the input speed  $n_1$ . On the diagram, there are marked the different  $\nu$ th order resonances to different  $k$ th order Fourier components of the excitation function, which fall together, see chapter 2.2., Eqs (3), (4), (5). The thin line is the line, where  $\tilde{n}'_{1s} = n_1$ . The intersection of this latter with the curves indicates the input speeds, which are just the speeds, involving excitation frequencies to the main resonance, at  $N = 1$ . This permits us to identify approximately the resonance order of the different peak values on the resonance curves, i.e. which  $\tilde{N}$  value can be attributed to them.

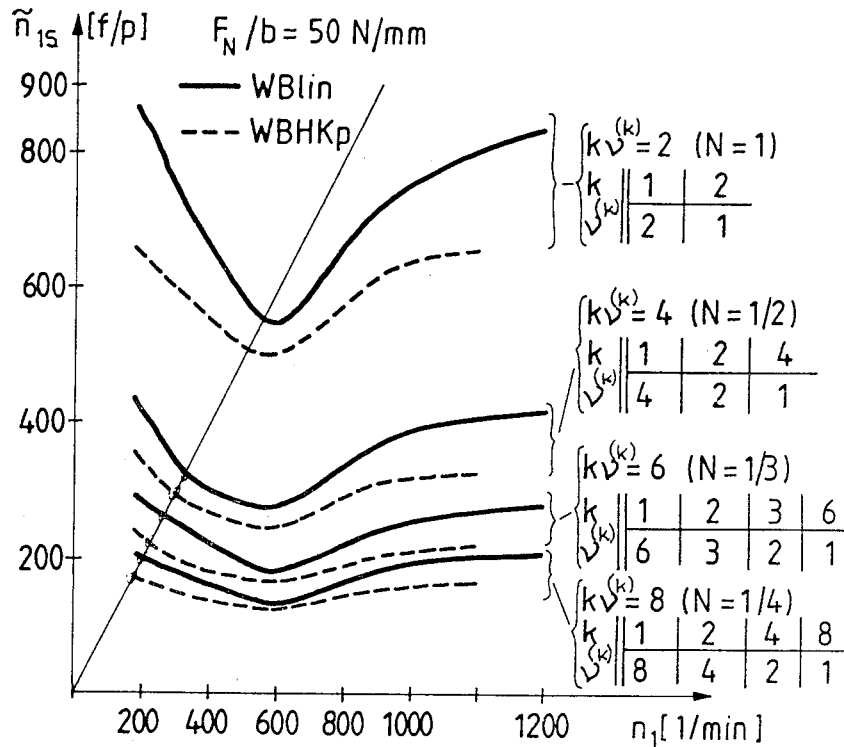


Fig. 13. Resonance frequencies expressed in pinion speed versus pinion speed

Based on Fig. 13 and the resonance curves on Fig. 11,  $F_N/b = 50$  N/mm, the following can be concluded, for the case WBlin:

- at input speed interval  $180/min < n_1 < 320/min$  the resonances corresponding to  $\tilde{N} = 1/4, 1/3$  develop,
- on interval  $320/min < n_1 < 600/min$  the resonances at  $\tilde{N} = 1/2, 1$  are overrun, but the two unstable regions do not separate,
- at speeds  $n_1 > 600/min$  the system is in overcritical region, and the resonance at  $n_1 = 1450/min$  is the overcritical one, with  $\nu^{(1)} = 1$ .

Similar conclusion can be drawn for the case WBHKp.

## 6. Conclusions

The simulation results of gear trains with normal involute profiles and with toothings with tooth tip relief presented in this paper have shown that even in the case of ideal tooth geometry, but with considering real mesh, i.e. taken into consideration of mesh irregularities due to tooth deflections at the beginning and end points of contact, non-linear system behaviour itself, as a result of kinematic excitation. In the case of profiles with tip relief, strong load dependent behaviour was found, with important vibrations at low load levels and tooth flank separations on broad speed intervals. The analysis of the vibrations at low load levels has shown that resonance regions move to lower input speeds and more resonance regions fall together. The results have shown that the single tooth pair stiffness characteristics have important effect on vibration characteristics.

In case of complex gear train dynamic simulations, the real tooth geometry parameters and mesh conditions, as components of the kinematic excitation, and real single tooth pair spring stiffness characteristics are to apply, for arriving to more realistic system response results.

## References

- [1] MUNRO, R. G. – YILDRIM, N. – HALL, D. M.: Optimum Profile Relief and Transmission Error in Spur Gears. *Proceedings of the Inst. of Mechanical Engineers*. Univ. of Cambridge. IMechE 1990. pp. 35–42.
- [2] NIEMANN, G. – WINTER, H.: Machine Elements, Bd. II. Springer Vlg. Berlin, Heidelberg, New-York, 1985. (In German).
- [3] MÁRIALIGETI J. (1995): Computer Simulation Study of the Influence of Tooth Errors on Gear Dynamic Behaviour. *Periodica Polytechnica Ser. Transp. Eng.* Vol. 23., No. 1–2, pp. 89–105.
- [4] MÁRIALIGETI J.: Non-linear Vibrations and Chaos in Gear Train. *2nd European Non-linear Oscillation Conference*, Prague 1996. Vol. 1. pp. 277–280.
- [5] KLOTTER, K.: Vibration Theory. Bd. 1. Springer Vlg. Berlin, Heidelberg, New-York 1980. (In German).
- [6] Calculation of the Load Capacity of Gears. DIN 3990. (In German).
- [7] WINTER, H. – PODLESNIK, B. (1983): Tooth Stiffness Characteristics of Gears. Part 2. *Antriebstechnik*, Vol. 22. No. 5. pp. 51–57. (In German).





## NON-LINEAR SYSTEM AND MODAL ANALYSIS

Dezső SZŐKE

Department of Vehicle and Lightweight Structure Analysis  
Technical University of Budapest  
H-1521 Budapest, Hungary  
E-mail: dezso@kme.bme.hu

Received: Nov 25, 1996

### Abstract

The modal analysis can only be applied for the analysis of linear systems with constant coefficients. Several objects could be practically described by a linear multidegree of freedom mechanical system if there would not be present local, frequently strong nonlinearities. Is it possible to describe the system in the reduced modal subspace if it contains nonlinear elements and if yes how is it?

*Keywords:* nonlinear system, modal analysis, modal reduction, base system, impact study, loading machine.

### 1. Introduction

The modal analysis means the investigation of dynamic systems with the aid of modal co-ordinates. These co-ordinates form the so-called modal subspace. In this space the set of the equations which describes the motion of the system is a set of linearly independent equations. It means that the investigated mechanical object can be assembled from subsystems, i.e. can be synthesised (modal synthesis). The advantage describing the system with the aid of modal co-ordinates is just in this! The motion of a multidegree of freedom system can be approached within a prescribed tolerance with the aid of some well-selected modal co-ordinates (modal reduction).

However, the modal analysis can only be applied for the analysis of linear systems with constant coefficients (time invariant systems). The linearity is necessary for the applicability of the principle of superposition, while time invariancy is the condition for the interpretability of the eigenproblem.

On the field of transportation we can find several objects which could be practically described by a linear multidegree of freedom mechanical system if there would not be present local, frequently strong nonlinearities. In this way, e.g. at the investigation of a loading machine there is the strongly nonlinear buffer (*Fig. 2*). In the case of a vehicle moving on a poor road to take into account the jumping of the wheel requires the investigation of a

nonlinear system. At the same time the shock absorbers are modeled with their nonlinearities (*Fig. 1*).

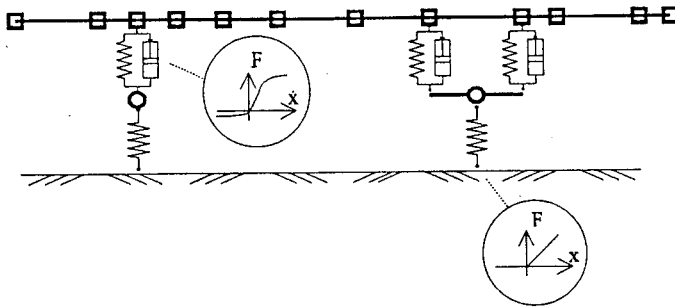


*Fig. 1.* Vehicle model with elastic body

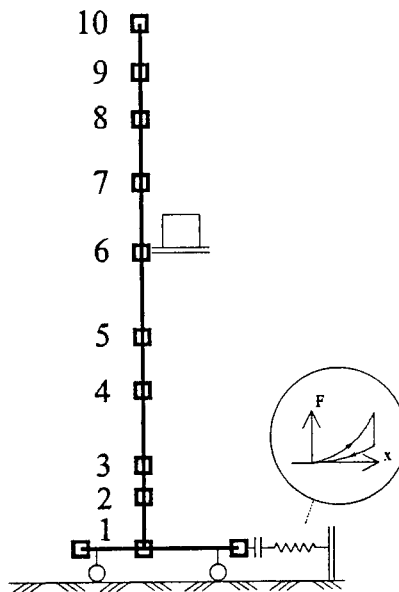


*Fig. 2.* Model of the loading machine

It asks for a vote of confidence: is it possible to describe the system in the reduced modal subspace if it contains nonlinear elements and if yes how is it? As an example we shall investigate the impact of a loading machine.

## 2. Theoretical Considerations

The response function of a nonlinear system is practically always produced by numerical integration. The solver subroutines for differential equations approach the values at the time  $T + \Delta t$  on the basis of finite differences. It means that at the time  $T$  we have a differential equation with constant coefficients. For this equation the modal condensation is applicable.

It is enough to know the modal co-ordinates of only one linear system as a base system. This base system is possible to be arbitrary, but by the experiences it is advantageous to choose a quasi-equivalent linear system to the nonlinear system. We transform the mathematical model of the object that the nonlinear force functions contain only the nonlinear differences with respect to the base system and they present on the right hand side of the equation as force excitation.

$$\begin{aligned} M\ddot{\mathbf{x}} &= \mathbf{F}(\mathbf{x}, \dot{\mathbf{x}}, t), \\ M\ddot{\mathbf{x}} + K\dot{\mathbf{x}} + S\mathbf{x} &= \mathbf{F}_b(\mathbf{x}, \dot{\mathbf{x}}, t)_{t=T}. \end{aligned} \quad (1)$$

At the numerical solution of the Eq. (1) for the time  $\Delta t$  the excitation force is constant. By this reason it is possible to transform the equation of motion into the modal subspace of the base system.

$$E\ddot{\mathbf{q}} + \Delta\dot{\mathbf{q}} + \Lambda\mathbf{q} = \mathbf{T}^*\mathbf{F}_b(\mathbf{x}, \dot{\mathbf{x}}, t)_{t=T} = \Phi_{t=T}. \quad (2)$$

And for the Eq. (2) the modal condensation is applicable! The values of the  $n$  elements of the displacement field at the time  $T + \Delta t$  can be estimate approach by the back transformation of the values at time  $T + \Delta t$  of some subspace co-ordinates. We can estimate the number of the subspace co-ordinates that we need to take into account on the basis of the type of the object, the investigated response sign, of the trend of the excitation.

## 3. Investigation of the Impact of the Loading Machine

The finite element model of the loading machine is simplified for the dynamic calculations. We take into consideration only some specific nodes on the column (static condensation). The dynamic model contains only the horizontal displacements and the number of the degrees is 10. The internal damping of the system is modeled proportional to the stiffness. By this way the model is a linear, time invariant system. But the force at the impact is nonlinear, because

- it is proportional to the square of the relative shortening;
- it depends on the direction of the change on the compressive range (hysteresis)

- it can apply an effect on the structure only in a restricted range (separation)

At the analysis of the impact process out of the direct solution of the equation of motion two 2 degree of freedom modal systems with different base systems were investigated. In one case the base system is the model of the loading machine moving freely on the rails. In the second case there is a flexible support with linear spring.

The 'time photo' of the impact is recorded with a time window of  $\Delta t = 0.01$  [s] (Fig. 3). The record starts when the loading machine as a rigid body with constant speed touches the buffer moving from the left to the right.

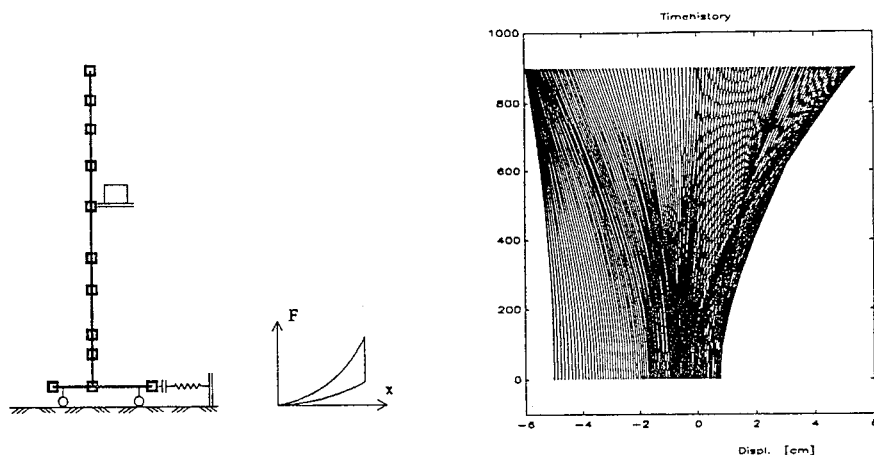


Fig. 3. Loading machine impact study (displacement of the beam, time photo)

The Fig. 4 presents together the impact force and the displacement of the particle in contact to the buffer.

It can be concluded that

- the change of the force is practically independent of the structure of the model
- the motion of the particle only at the fixed base system differs to practically identical characteristics of the other two systems only over the separation.

The reliability of the applied synthesis is characterised by the deviation functions of the displacements with respect to the direct response signs.

If we choose a free system for base system then the motion of the loading machine can be approached within 1 mm precision (1.5% relative precision) taking into consideration the first two bending modes.

The fixed base system shows a bigger difference.

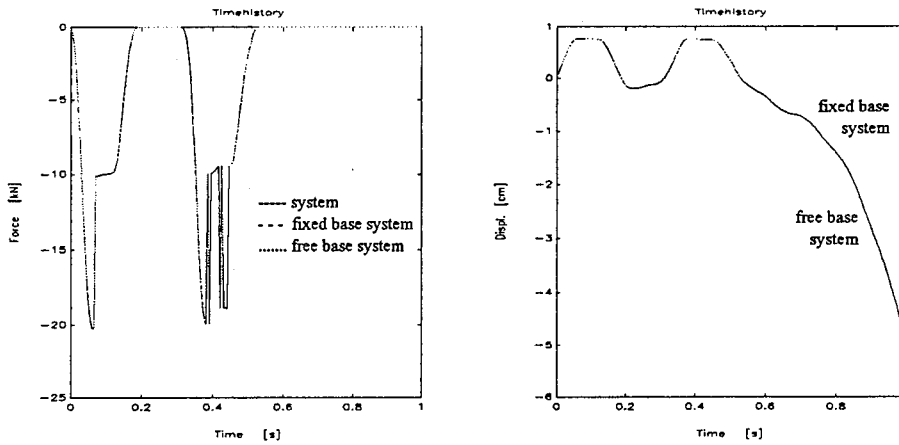


Fig. 4. Impact force and displacement of the particle in contact to the buffer

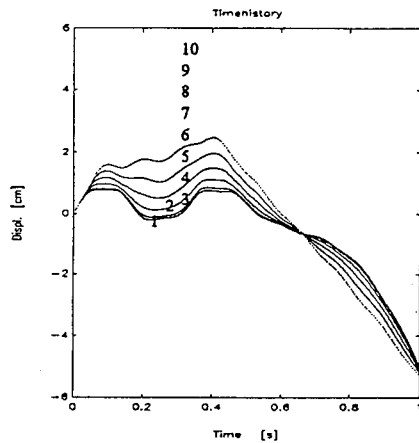


Fig. 5. Displacements of the loading machine under impact (direct response signs)

At the analysis we use linear functions at the buffer spring, too, instead of the parabolic one (Fig. 7).

In this case we can only repeat the results of the comparative test.

Finally we can state that

- using a free system as a base system model of the loading machine with two modal co-ordinates it is applicable for the investigation of the impact. It can replace the multidegree of freedom model of the direct method and
- verify the property of the applied method.

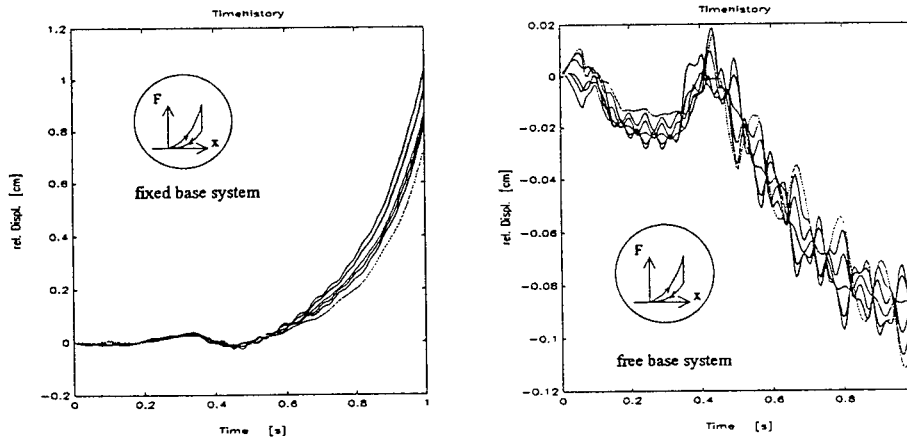


Fig. 6. Deviation (quasi error) functions of the time histories

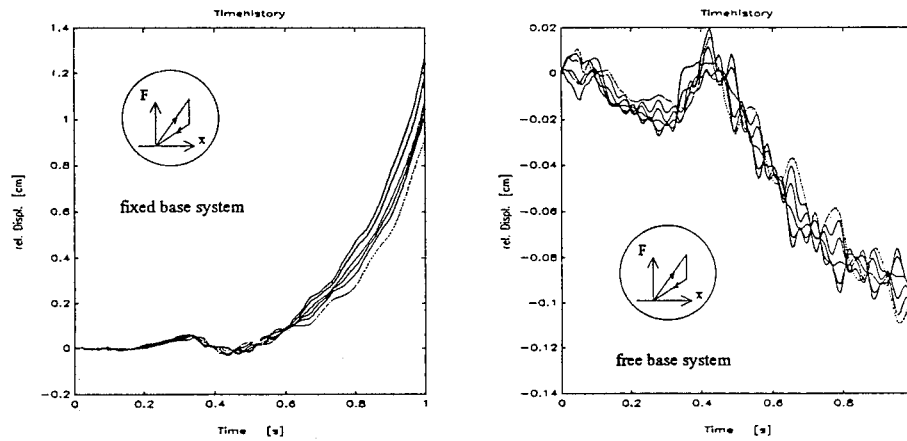


Fig. 7. Deviation (quasi error) functions of the time histories

#### 4. Concluding Remarks

On the basis of the theoretical investigations and numerical simulations, the following conclusion can be drawn:

- the applied method can be used, but further object specific investigations are required (e.g. analysis of vehicles).

#### References

- [1] NATKE (1983): Einführung in die Theorie und Praxis der Zeitreihen, Vieweg Verlag Gmbh, Braunschweig.

## NON-LINEAR DYNAMIC ANALYSIS OF VEHICLES USING LARGE FINITE ELEMENT MODELS

István KUTI

Department of Vehicle Frame and Lightweight Structures  
Technical University of Budapest  
H-1521 Budapest, Hungary

Received: October 31, 1996

### Abstract

In the dynamic analysis and design of vehicles the behaviour of suspensions and tyres beyond the linear range is often interesting. In order to get acceptable responses it is necessary to apply large mechanical models with many degrees of freedom. In this paper a computational method and a computer program, developed for the dynamic analysis of elastic systems containing local non-linearities are presented. The applicability of this method and program is demonstrated by numerical experiments using a 648 degrees of freedom flat-bed truck finite element model.

*Keywords:* nonlinear analysis, vehicle dynamics, modal analysis, modal condensation, transient vibrations

### 1. Introduction

Nowadays, in the design or research of mobile machines and dynamically excited structures, besides experiments, the different numerical computational methods provide efficient tools. However, the solution of most large-scale (non-linear) dynamic structural problems is usually extremely time consuming. Therefore, in latest decades, considerable efforts have been made in the application and development of numerical methods, to increase their accuracy and speed of computation. For this type of problems the modal time history analysis, combined with modal condensation, seems to be as a successful way, where the local non-linearities are considered as pseudo forces [1], [2], [3].

The dynamic behaviour of road and off-road vehicles (cars, buses, trucks, cross country cars, agriculture vehicles, etc.) can be mentioned as typical examples for the previously discussed dynamical problems in case of certain driving conditions. For example, passing over road defects (bulge, hole) or driving on roads of wrong quality. In these cases the non-linear properties of vehicles may not be neglected.

With regard to preliminaries, in this paper, a computational procedure and a computer program is presented, developed for non-linear dynamic analysis of large elastic systems with local non-linearities. As it was

mentioned above, the pseudo force method is applied to the calculation of internal forces that arise from the effects of local non-linearities [4]. From the point of view of practical applications, the elaboration of large mechanical (usually finite element) models can give rise to significant difficulties. Recently the use of commercial finite element programs seems to be the only reasonable way. In order to utilise this advantage of commercial finite element programs, the developed procedure consists of two phases. In the first phase, the linearized and undamped finite element model of the given structure can be elaborated, using any commercial finite element program. Great advantage of this way is that the required natural modes (natural frequencies and vectors) can be determined by these programs. Then, in the second phase, having considered the local non-linearities (springs, dampers, gaps, etc.) the dynamic analysis can be carried out.

To verify the applicability and efficiency of the developed method and computer program, using a flat-bed truck finite element model (with 648 degrees of freedom), numerical experiments are presented. The accuracy of the elaborated computer program in comparison with COSMOS/M finite element program will be demonstrated.

## 2. Mathematical Formulation

Assume that the dynamic equilibrium equation of the studied structure is described by  $n$  pieces of coupled second order ordinary differential equations, as follows,

$$[\mathbf{M}]\{\ddot{\mathbf{x}}\} + [\mathbf{K}]\{\dot{\mathbf{x}}\} = \{\mathbf{F}(t)\} + \{\mathbf{N}(\{\mathbf{x}\}, \{\dot{\mathbf{x}}\}, \{\ddot{\mathbf{x}}\})\}, \quad (1)$$

where:

$[\mathbf{M}]$	=	mass matrix,
$[\mathbf{K}]$	=	stiffness matrix of the linear part of the structure,
$\{\mathbf{F}\}$	=	vector of time varying forces and kinematic excitations applied on the structure,
$\{\mathbf{N}\}$	=	pseudoforce vector of non-linear internal forces,
$\{\mathbf{x}(t)\}$	=	generalized displacement vector,
$\{\dot{\mathbf{x}}(t)\}$	=	generalized velocity vector,
$\{\ddot{\mathbf{x}}(t)\}$	=	generalized acceleration vector,
$t$	=	time.

Mode shapes, for modal time history analysis, are calculated from the left side of Eq. (1) in the next form,

$$(\lambda_i[\mathbf{I}] - [\mathbf{M}]^{-1}[\mathbf{K}])\{\Phi_i\} = \{\mathbf{0}\}, \quad (2)$$



where:

- $[\mathbf{M}]^{-1}$  = inverse of mass matrix,
- $[\mathbf{I}]$  = identity matrix,
- $\{\Phi_i\}$  =  $i$ -th natural vector,
- $\lambda_i$  =  $i$ -th natural value,
- $\{0\}$  = zero vector.

If the natural vectors are normalized to mass matrix, then natural values are the square of the corresponding natural frequency. The natural vectors as column vectors can be arranged, according to the ascending order of natural values, into the matrix  $[\Phi]$ , called the modal matrix. Modal displacement, velocity and acceleration vectors can be defined as,

$$\{x\} = [\Phi]\{q\}, \quad (3-a)$$

$$\{\dot{x}\} = [\Phi]\{\dot{q}\}, \quad (3-b)$$

$$\{\ddot{x}\} = [\Phi]\{\ddot{q}\}, \quad (3-c)$$

where  $\{q\}$ ,  $\{\dot{q}\}$  and  $\{\ddot{q}\}$  are the modal displacement, velocity and acceleration vectors, respectively. Substituting Eqs (3.a – c) into Eq. (1), then premultiplying by  $[\Phi]^T$ , the transpose of  $[\Phi]$ , we get,

$$[\Phi]^T[\mathbf{M}][\Phi]\{\ddot{q}\} + [\Phi]^T[\mathbf{K}][\Phi]\{b\dot{q}\} = [\Phi]^T(\{F\} + \{N\}), \quad (4)$$

where  $[\Phi]^T[\mathbf{M}][\Phi]$  is the  $n \times n$  identity matrix, and matrix  $[\Phi]^T[\mathbf{M}][\Phi]$  is a diagonal one and its diagonal elements are equal to the square of the corresponding natural frequencies. Thus the modal differential equations can be written as,

$$\ddot{q}_i + \omega_i^2 q_i = \sum_{i,j} \Phi_{i,j} (F_i + N_i), \quad i, j = 1, 2, \dots, n, \quad (5)$$

where subscripts  $i$  and  $j$  are the indices of the elements of previously applied matrices and vectors. When only the first  $m$  ( $m \gg n$ ) pieces of modal differential equations are applied for dynamic analysis, the amount of computational time can significantly be reduced into an acceptable practical range (modal condensation). Modal and Rayleigh damping can additionally be included into Eq. (5).

### 3. On the Developed Computer Program

On the basis of previous relationships an algorithm has been elaborated and a computer program, called MODANAL, has been coded in MICROSOFT FORTRAN V.03. This program contains approximately 1200 FORTRAN statements.

As it was mentioned above, the complete, modelling and computational, process is divided into two phases. In the first phase the elaboration of the (undamped) linearized finite element model and its mode shape calculation can be carried out by the use of an appropriate commercial finite element program. Thereafter, in the second phase, having utilized data and results from the first phase and having prepared the additional data, concerning to the description of local non-linearities and external excitations, the non-linear dynamic analysis can be performed by the developed computer program. This program uses six input files, three output files and seven temporary files, detailed below.

Input files,

- file to store control parameters, description of non-linear characteristics and the specification of required output,
- file to store natural frequencies and vectors involving into the non-linear analysis (extracted from the output file of the applied commercial finite element program),
- file to store mass data of the whole model to the calculation of inertial forces (extracted from the input data file of the applied commercial finite element program),
- file to store initial displacements and velocities (initial displacements can be calculated, for example, by static analysis of the linearized finite element model, carried out by the applied commercial finite element program),
- file to store kinematic excitations,
- file to store external forces and moments.

Output files,

- file to store required displacements,
- file to store required velocities,
- file to store required accelerations.

To the numerical step by step solution Hamming's predictor-corrector method is applied. The characteristics of local non-linearities are described by piecewise linear functions, as it is usual in finite element programs.

#### 4. Description of the Applied Truck Model

In order to demonstrate the applicability and effectiveness of the discussed computational procedure and the related computer program, a simple flat-bed truck model has been elaborated, making use of COSMOS/M commercial finite element program (*Fig. 1*). In the suspension sets leaf springs are applied and their elasticity is considered at the extremities of the leaf springs, while the dampers (in suspensions) are positioned at the midpoint

of the rigid spring arms, just above the truck axles. In *Fig. 1*, the damper and springs of the right hand side front suspension are shown up with short thick lines. The elasticity and damping of each tyre is represented by three springs and (viscous) dampers positioned in longitudinal, lateral and vertical directions. Linearized and non-linear suspension spring characteristic are shown in *Fig. 2*, where the non-linear sections of spring characteristic represent the upper and lower bumpers which limit the stroke of suspensions. The non-linear spring characteristic is shifted along the linear one, in accordance with the initial displacements arising from payload and the weight of the truck. Similarly, the linearized and non-linear suspension damper characteristics are represented in *Fig. 3*. The linearization of the non-linear damper is based on manufacturer's data, and both of them absorb the same kinetic energy in case of the prescribed frequency and stroke (1.67 Hz and 100 mm stroke). Anti-roll torsion bar (stabilizer) is built in between the chassis and rear axle.

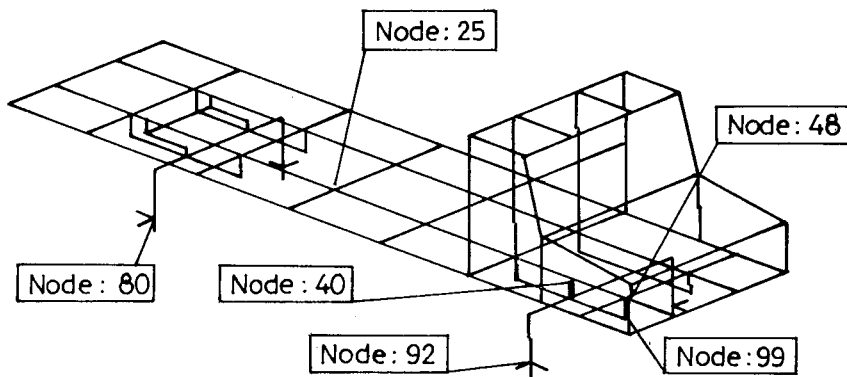


*Fig. 1.* Skeleton structure of the studied truck

Finite element model data:

Total number of nodes:	125
Number of degrees of freedom:	648
Total number of beam elements:	159
Total number of mass elements:	51
Total number of non-linear spring elements:	12
Total number of linear spring elements:	8
Total number of non-linear damper elements:	4
Total number of linear damper elements:	8
Total mass (payload is included):	13751kg

It is necessary to emphasize that this truck model has been developed for vertical excitation (its velocity is assumed to be constant during the analysis), only to demonstrate the applicability and effectiveness of the computational method and computer program presented here. In this truck finite element

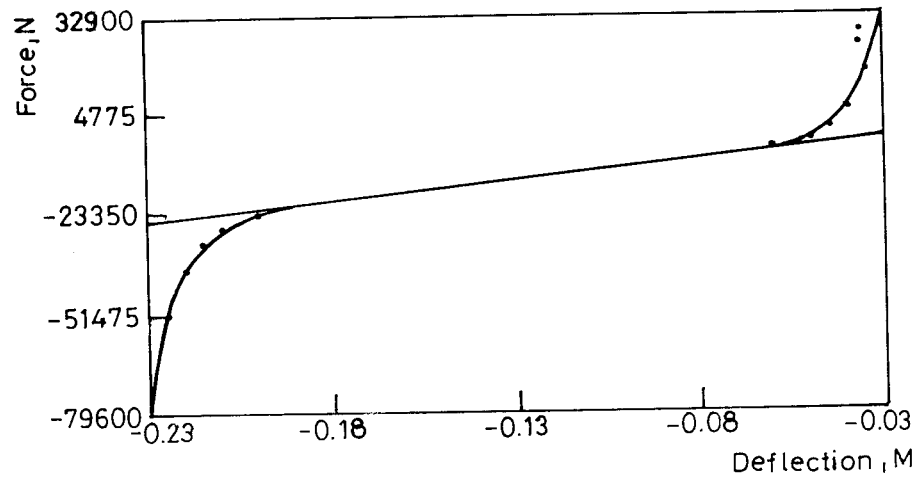


Fig. 2. Spring characteristics (in suspensions)

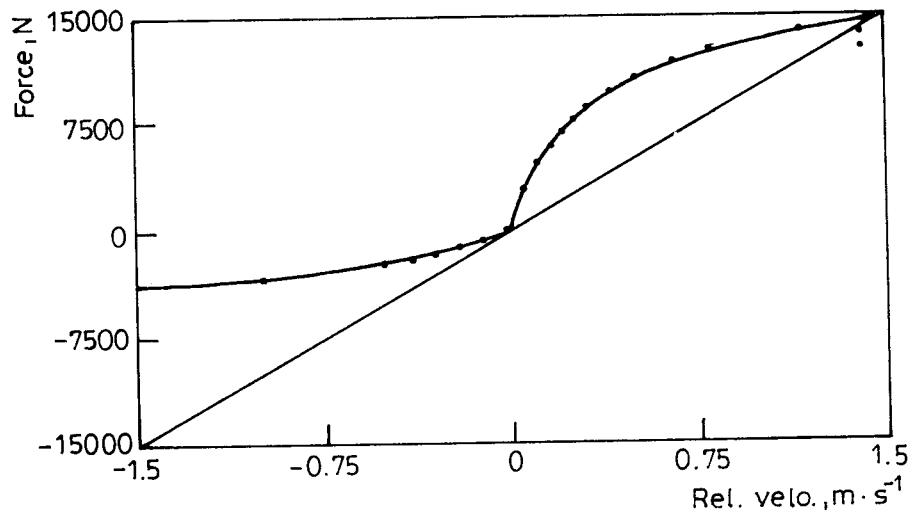


Fig. 3. Damper characteristics (in suspensions)

model, there can be found such kinds of simplifications which practically do not affect disadvantageously on the following demonstrations, however, they may not be applied in most cases in the dynamic analysis of actual structures. For example, the finite element model of the truck is not detailed enough for strength calculation, payload is connected to nodes, structural damping is considered roughly by Rayleigh damping (only to avoid the undesirable fictitious resonance because of the lack of internal damping), etc.

## 5. Verification of the Applied Method

The accuracy of the developed computer program was comprehensively investigated earlier. Herein a comparison is made between the presented computer program and COSMOS/M. For this purpose steady state harmonic force excitations are applied, in vertical direction, at the extremities of the front axle, in case of linearized springs and damper characteristics. Zero initial conditions, and no weight of the truck and payload, are applied. Amplitude of exciting forces is equal to 50000 N and their frequency is equal to 9.5 Hz. Calculation is carried out between 0 and 12.5 seconds in 5000 steps. There can be seen, in *Fig. 4*, the vertical displacement response of node No. 99 calculated by COSMOS/M. The difference, for this node between the responses calculated by COSMOS/M and MODANAL, is shown in *Fig. 5*. It can be seen from *Figs 4 - 5* that the relative difference between the amplitude of these responses is no more than 0.45%, which is an excellent agreement. From computational aspect it is worth to mention that for numerical solution in COSMOS/M Newark's iterative method, while in MODANAL a predictor-corrector method is applied.

Usual principle in vehicle structural dynamics is that it is enough to apply the low natural modes up to 20 Hz. To confirm this principle the same harmonic kinematic excitation is applied on both tyres of front wheels in vertical direction. Its amplitude is 20 mm and its frequency, being proportionate to time, is swept from 0 Hz to 20 Hz. The linearized and non-linear response of node No. 25 (a structural point in chassis), for this sweeping excitation, can be seen in *Figs 6 - 7*, respectively. These figures confirm this reduction of the numbers of natural modes, since the amplitudes of vibration above 6 Hz significantly decrease in the function of frequencies. In correspondence with this principle, in this paper, the first thirty natural modes are applied for dynamic analysis. The magnitude of the highest natural frequency is equal to 21.45 Hz.

## 6. Numerical Experiments

### 6.1. *Passing through a Bulge*

In this example the better damping properties of non-linear dampers, in suspensions, compared to the linearized ones are demonstrated. For this purpose, assume that a small bulge is in the perfectly smooth road surface, positioned in lateral direction and described by a simple cosine function. Its length is 1.5 m and its maximum height, in the middle, is equal to 25 mm. In this case the spring deflections remain in linear range, therefore, the linearized and non-linear dampers can be compared directly. The truck is passing over this bulge with the speed of 72 km/h. Both, left and right,

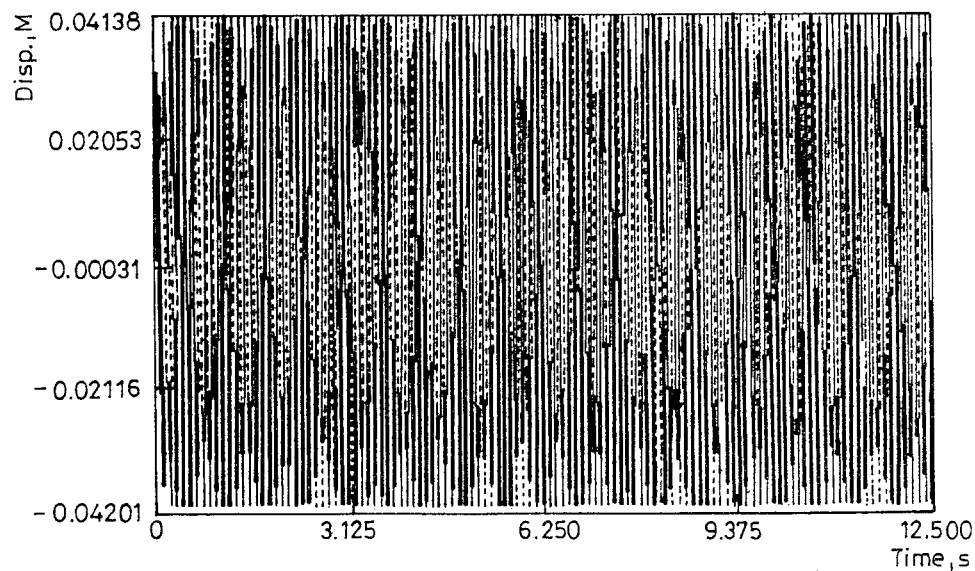


Fig. 4. Response of node No. 99 calculated by COSMOS/M

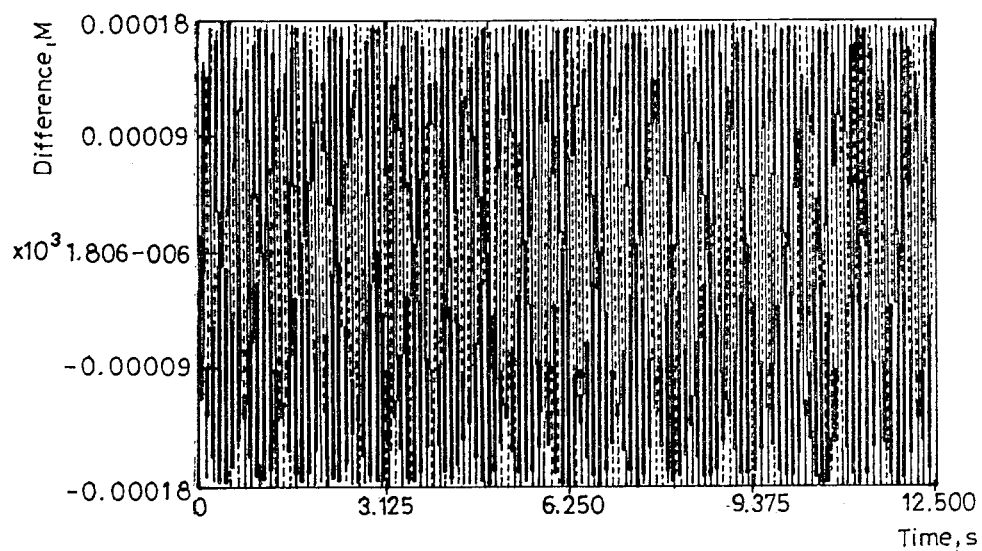


Fig. 5. Difference between responses of COSMOS/M and MODANAL

wheels are passing over it at the same instant. Time delay between the excitations of front and rear wheels is taken into consideration. In relation

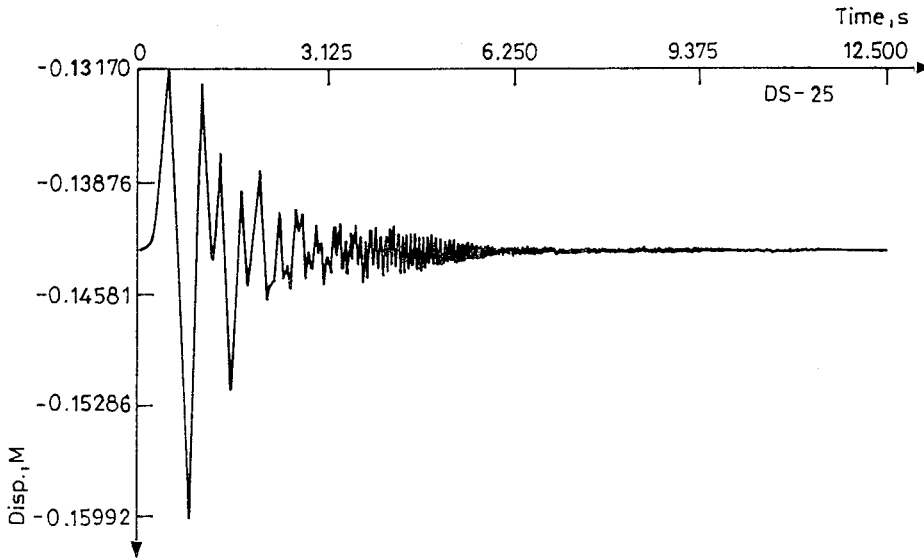


Fig. 6. Linearized response of node No. 25 for sweeping excitation

to this excitation, there can be seen the linearized and non-linear vertical displacement and velocity responses of node No. 40 in *Figs 8 – 9* respectively. Node No. 40 represents the point of attachment of the right hand side front suspension to the chassis (*Fig. 1*).

In *Fig. 8* the thick line shows the linearized, while the thin line shows the nonlinear responses. Similar marking is used for the velocity response in *Fig. 9*. Both figures show that the linearized responses are overestimated and, at the same time, there can be seen the better damping effects of non-linear dampers.

## 6.2. Driving on a Minor Road of Wrong Quality

In case of actual vehicles the stroke of suspensions is limited, which is taken into consideration here by the highly non-linear parts of spring characteristics (*Fig. 2*). When a vehicle is driving on a road of wrong quality, the undercarriages can collide with the body of vehicle at both extreme positions of suspensions. In *Fig. 10* there can be seen road profile realizations, generated from a two dimensional isotropic power spectral density function of road surface roughness [5], [6], [7]. It is assumed that the truck is driving on this road with a speed of 36 km/h. Initial displacements and the total

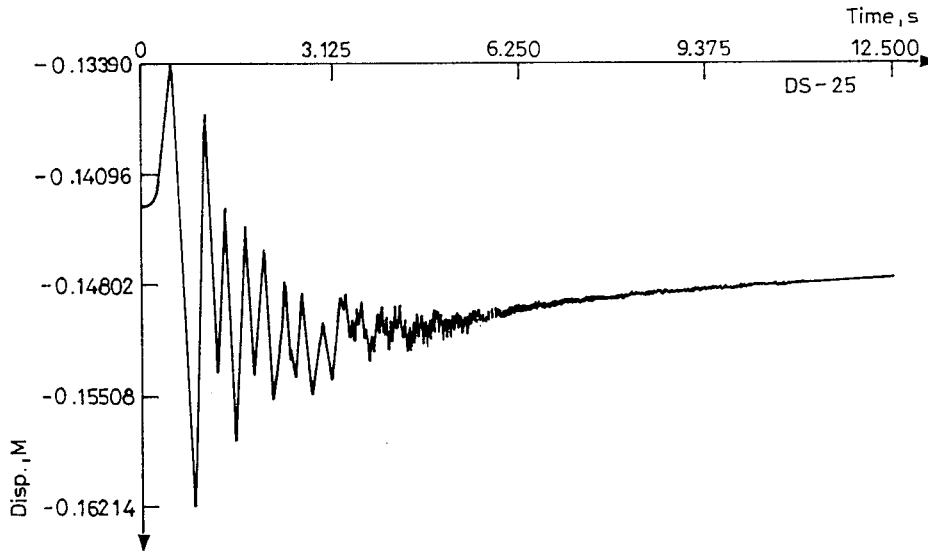


Fig. 7. Non-linear response of node No. 25 for sweeping excitation

weight of the truck are involved into the dynamic analysis. Time delay between the excitations of front and rear wheels is considered. In Fig. 11 there can be seen the linearized and in Fig. 12 the non-linear vertical acceleration of node No. 48 under the action of this excitation. Node No. 48 is the point of attachment of one of the front springs in the right hand side suspension above the front axis. The greater values in non-linear response (greater lower and upper peaks) with respect to the linearized one, are arising from the collisions of the front undercarriage to the chassis of the truck at both extreme positions of this suspension. From Figs 11 - 12 it is clear that, in this case, the linearized response is underestimated.

### 6.3. Demonstration of Wheel Bouncing

In order to illustrate the wheel bouncing, the total mass (sum of the dead mass and payload) of the truck is decreased from 13751 kg into 6696 kg and its velocity is risen to 108 km/h. Total weight of the truck and the initial displacements under the action of total weight are included in the analysis. For the sake of better visualisation the roughness of the road surface is neglected. In Fig. 13, there can be seen the applied ramp. Its upward-slope portion is equal to 15 m and its downward-slope portion is equal to 30 m.



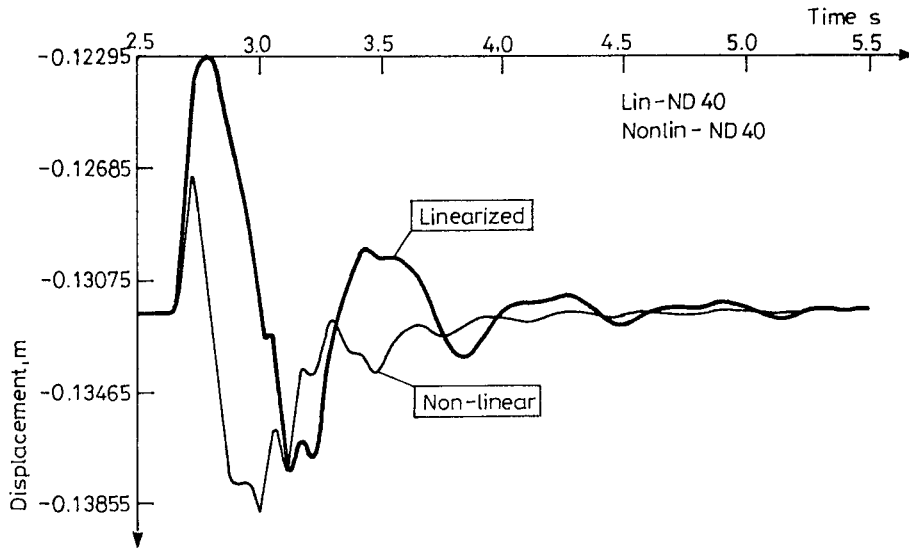


Fig. 8. Linearized and non-linear responses (displacement) of node No. 40

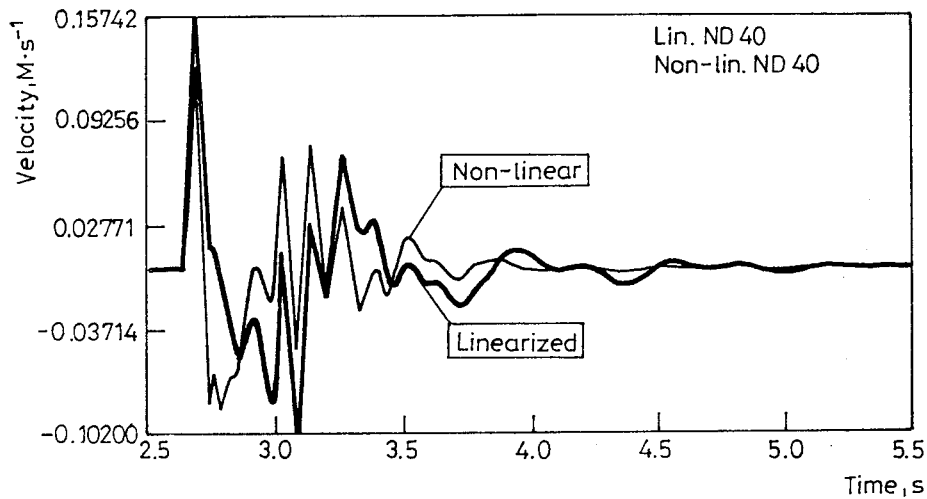


Fig. 9. Linearized and non-linear responses (velocity) of node No. 40.

In the upward-slope portion, the gradient of left track is different from the gradient of the right track. Therefore there are different vertical velocities of the left and right hand side wheels at the top of the ramp, originating a rotation of the truck along its longitudinal axis (rolling motion). Fig. 14

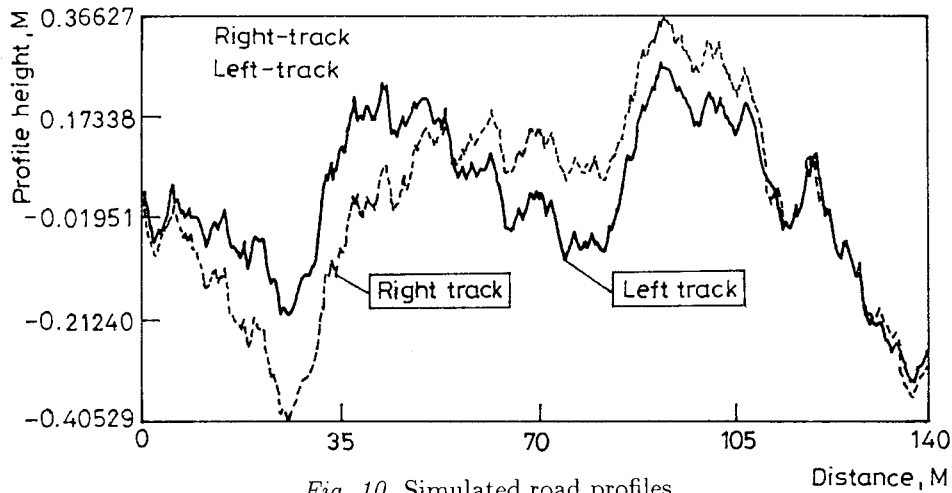


Fig. 10. Simulated road profiles

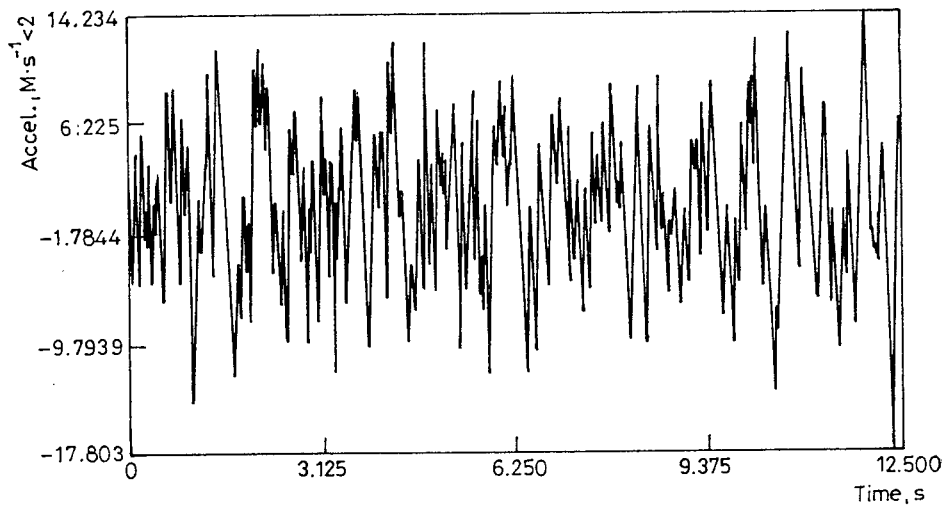


Fig. 11. Linearized response (acceleration) of node No. 48

shows the rotations of front and rear axles in radians. At the same time, because of this rotation, there exists a lateral motion of different elements of the truck. There can be seen in Fig. 15 the lateral motion of the centres of the right hand side wheels.

In Fig. 16 the vertical position of node No. 80, connected to the road surface by springs and dampers, is illustrated. Node No. 80 represents the lowest point of the right hand side rear wheel disc. The thick piecewise linear line in Fig. 16, symbolizes the right track, while the parallel thin one represents the position of node No. 80 when the tyre is assumed to be

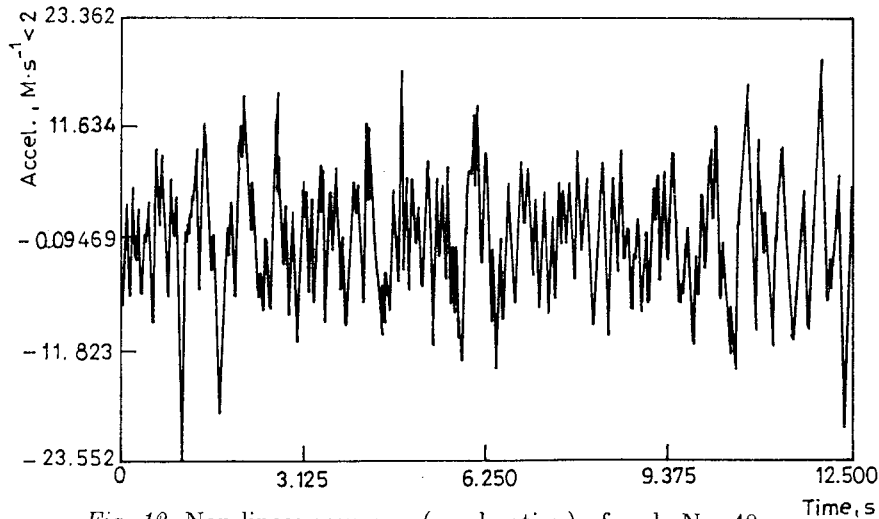


Fig. 12. Non-linear response (acceleration) of node No. 48

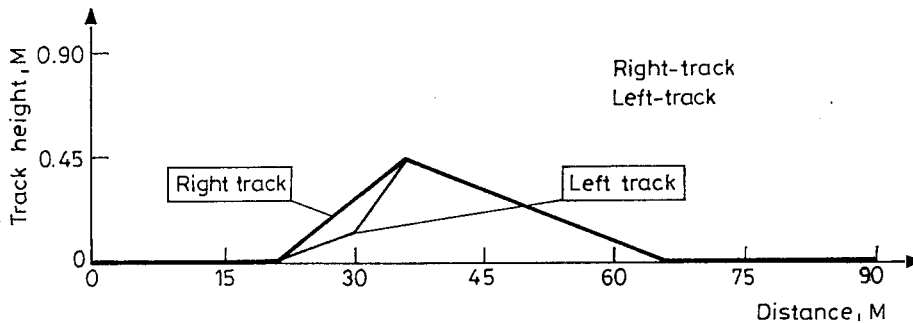


Fig. 13. Ramp to demonstrate wheel bouncing

unloaded. The distance between the two piecewise linear lines illustrates the vertical dimension of the unloaded tyre.

The curved line shows the vertical position of node No. 80 calculated from its excited displacement while the truck is passed over the ramp. When the curved line is below the thin piecewise linear line the wheel is in contact with the surface of the ground (ramp), and when it is above this line the wheel is bouncing. In Fig. 17, similarly to Fig. 16, the vertical position of the lowest point of the left hand side rear wheel disc is shown.

The magnitude of bouncing of a given wheel can be determined if the unloaded position of the lowest point of wheel disk is subtracted from its excited vertical position at each step. When it is greater than zero the wheel is bouncing. The magnitudes of the bounces of rear and front wheels are demonstrated in Figs 18 – 19. In Fig. 18 there can be seen consecutive bounces of the right hand side rear wheel. An interesting thing can be seen

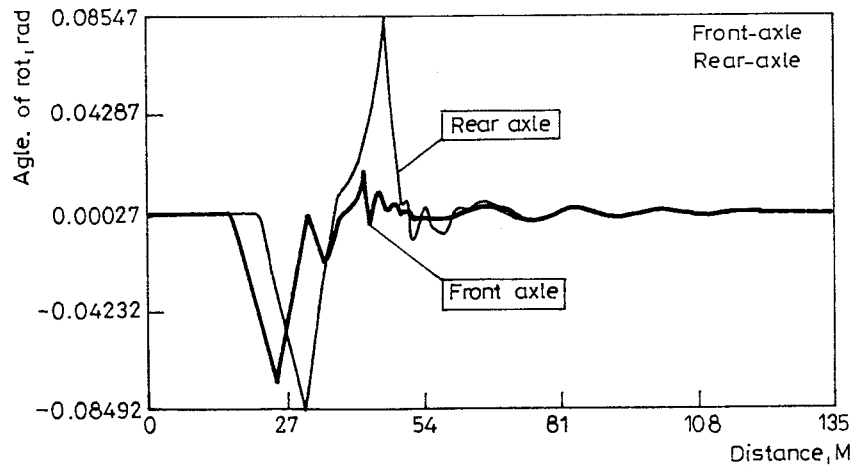


Fig. 14. Rolling motion of front and rear axles



Fig. 15. Lateral motion of the right hand side wheels

in Figs 18 – 19, namely each wheel is bouncing at the same time from 1.209 s to 1.386 s, that is the truck is flying over the ramp 5.31 meters.

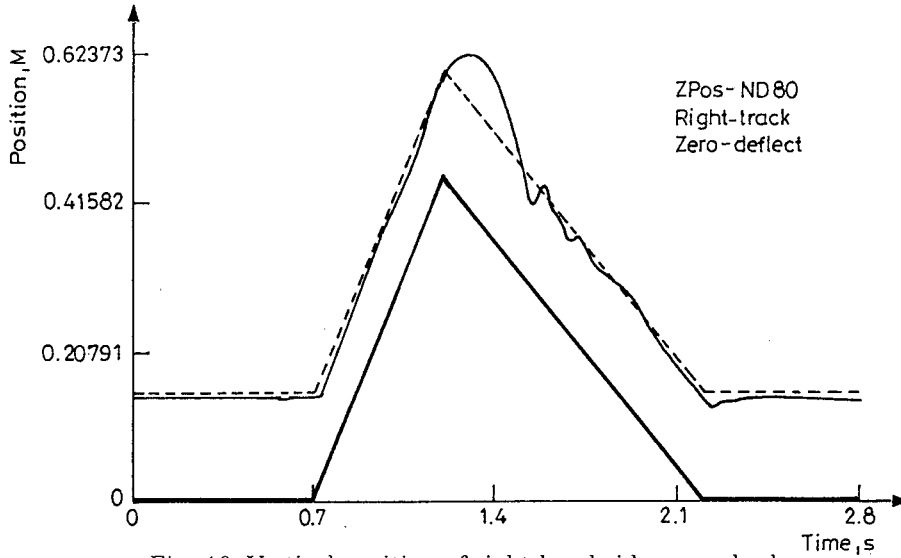


Fig. 16. Vertical position of right hand side rear wheel

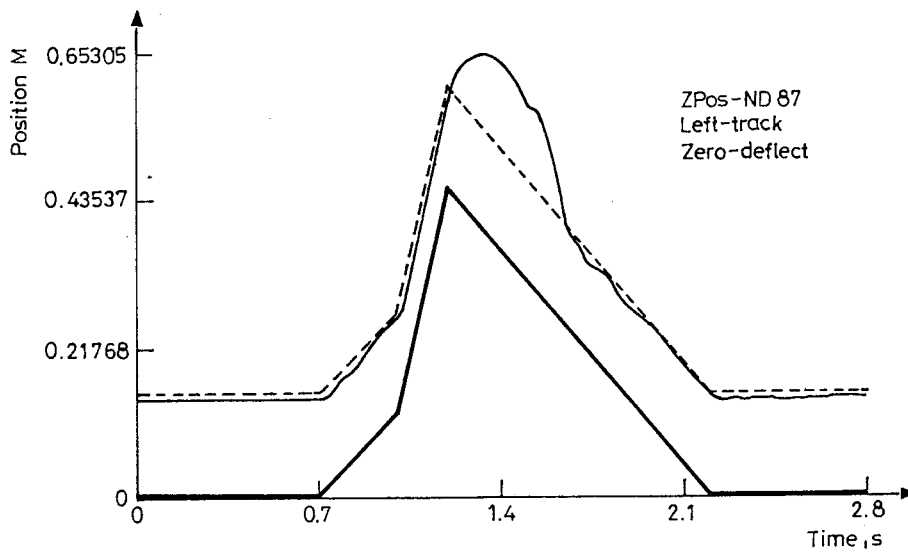


Fig. 17. Vertical position of left hand side rear wheel

## 7. Conclusions and Closing Remarks

The numerical experiments presented herein indicate the accuracy, effectiveness and applicability of the presented computational procedure and computer program, using in non-linear structural dynamic analysis. It is par-

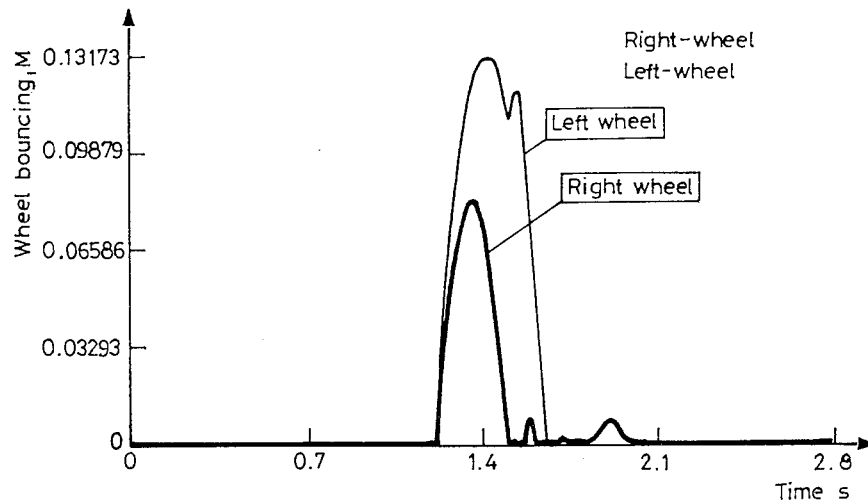


Fig. 18. Magnitude of wheel bouncing of rear wheels

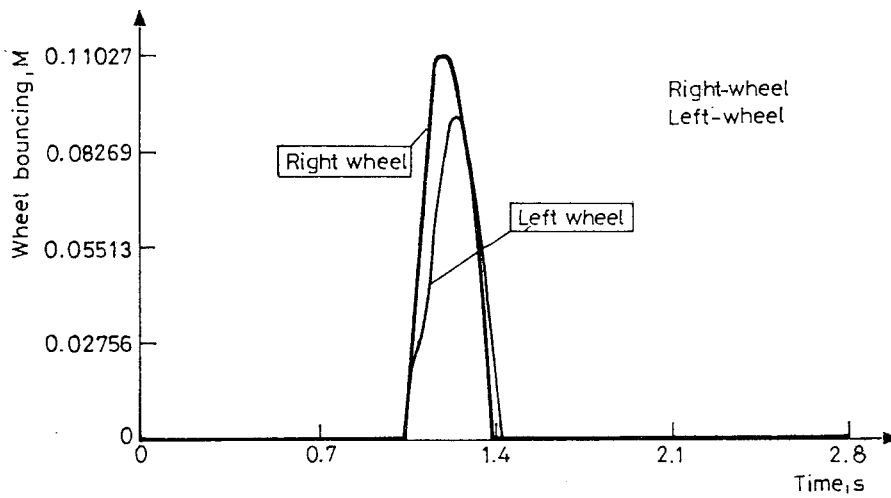


Fig. 19. Magnitude of wheel bouncing of front wheels

ticularly effective when the order of largest stiffness of local non-linearities is not significantly higher than the order of stiffness of the linearized part of the studied structure. Road and off road vehicles (cars, trucks, buses, cross-country cars, agricultural vehicles, etc.) fall within this category. Numerical examples show that the discussed method is especially useful in case of wrong driving conditions, such as, driving vehicles on minor roads of wrong quality, or driving overland cars on terrain containing large irregularities.

The number of degrees of freedom of the applied truck finite element

model, in this paper, is equal to 648 and the lower 30 natural modes were involved into the non-linear dynamic analysis, up to 20 Hz. The time period of numerical solution phase, during 5000 steps, was equal to 123 seconds which contain the time for binary output of modal variables in each step, and the total solution time period was equal to 197 seconds. Since natural modes depend on structural properties rather than the number of degrees of freedom of the applied finite element model, the writer assumes that this method, in vehicle dynamics, can be applied for significantly larger finite element models in case of more thousands degrees of freedom, and probably more than ten thousand ones. To support this assumption, the solution time duration of a similar non-linear dynamic analysis of a bus structure, containing 1848 degrees of freedom, was equal to 162 seconds (the total solution time was 281 seconds). In the analysis the lower 50 natural modes were involved, up to 20 Hz, and the calculation was also carried out in 5000 steps [8].

In this paper, in all the numerical examples only vertical excitations are applied, however, the model description and the directions of excitations are not restricted in this method, consequently, it can also be applied for horizontal dynamics of vehicles. Moreover, additional equations and conditions of different mechanical effects can be attached easily to the modal equations, describing the vehicle motion. This possibility significantly enlarges the fields of application of the method presented in this paper, for example, the equations of breaking processes for simulation and to support the design of brake systems (including optimal ABS (Anti-lock Brake System) control strategies). Other important areas are: the simulation, the behaviour and support the design of optimal active suspension systems, application in the identification of vehicle parameters and, at last, numerical stability analysis of vehicles subjected to complex driving and loading conditions.

A program module for the calculation of internal forces and stresses can be built in the developed finite element program.

### References

- [1] BATHE, K. J. – GRACEWSKI, S. (1981): On Non-linear Dynamic Analysis Using Substructuring and Mode Superposition. *Computers & Structures*, Vol. 13, pp. 699–707.
- [2] CHANG, C. J. (1990): Modal Analysis of Non-linear Systems with Classical and Non-classical Damping. *Computers & Structures*, Vol. 36, No. 6, pp. 1067– 1078.
- [3] LEVEL, P. – GALLO, Y. – TISON, T. – RAVALARD, Y. (1995): On an Extension of Classical Modal Reanalysis Algorithms: the Improvement of Initial Models. *Journal of Sound and Vibration*, Vol. 186, No. 4, pp. 551–560.
- [4] MOLNÁR, A. J. – VASHI, K. M. – GAY, C. W. (1976): Application of Normal Mode Theory and Pseudo Force Methods to Solve Problems with Non-linearities. *Journal of Pressure Vessel Technology*, May, 1976, pp. 151–156.

- [5] PELLEGRINO, E. – TORNAR, U. (1987): A Mathematical Model of Road Excitations. *Proceedings of the Second Workshop on Road-Vehicle-Systems and Related Mathematics*. Torino, pp. 7–26.
- [6] KAMASH, K. M. – ROBSON, J. (1989): The Application of Isotropy in Road Surface Modelling. *Journal of Sound and Vibration*, Vol. 57, No. 1, pp. 89–100.
- [7] SHINOZUKA, M. (1972): Digital Simulation of Random Processes and its Applications. *Journal of Sound and Vibration*, Vol. 1, No. 1, pp. 111–128.
- [8] KUTI, I. (1996): Non-linear Dynamic Analysis of Elastic Systems Containing Non-linear Springs and Dampers. (presentation in Hungarian), *Intern Symp. on Tools and Methods for Concurrent Engineering*, Budapest. May 29–31, 1996.



## ANALYSIS OF DYNAMIC LOADS OF THE LATTICE TYPE MAST STRUCTURE OF A TOWER CRANE USING SIMULATION METHOD

András PRISTYÁK

Department of Building and Materials Handling Machines  
Technical University of Budapest  
H-1521 Budapest, Hungary

### Abstract

The oscillations of the crane, especially the pendulum motion of the lifted load suspended from rope, makes the load positioning operation difficult, endangers the potential stability of the crane and the dynamic forces, due to their oscillating feature, lead to fatigue damage of structure components. On the other hand, it is not possible to perform a fatigue analysis without the knowledge of the so-called *stress-time histories*. All this requires the application of dynamic analysis methods.

This paper is intended – through the analysis of transient motions and loading of a lattice type mast structure of a tower crane – to show the possibilities of computer simulation of dynamic loads and stresses and in promotion of the crane design.

*Keywords:* crane, dynamics, stress-time-histories, simulation.

### 1. Developing of the Dynamic Model

It is known that the tower cranes belong to the group of intermittent duty equipment. It is characteristic for them, too, a tall and slender mast or tower, a long jib, a complicated load lifting, jib holding and luffing rope system, and, furthermore, that they commonly have four autonomous driving systems which can be started independently one by one, and two or three instationary motions can exist at the same time (*Fig. 1*). Under the lifting and crane or trolley travelling motions, combined with slewing motion of the crane, the load is subjected to spatial pendulum motion that has significant influence to the loads of the mast, to support forces and to the potential stability of the crane.

For determination of loads and stresses in the mast structure it is necessary to analyse the cross-section where the maximum effects are expected. For the crane investigated (a KB 160/2 type crane) this cross-section is located in the vicinity of the lower fixation of the mast in the portal: the cross-section *I – I* in *Fig. 1*, or this is the plane of truncation in *Fig. 2*. For this cross-section we can determine a system of 6 loading vectors (*Fig. 2*):

$$\mathbf{F} = f(\mathbf{F}_z, \mathbf{M}_z, \mathbf{F}_x, \mathbf{F}_y, \mathbf{M}_x, \mathbf{M}_y),$$

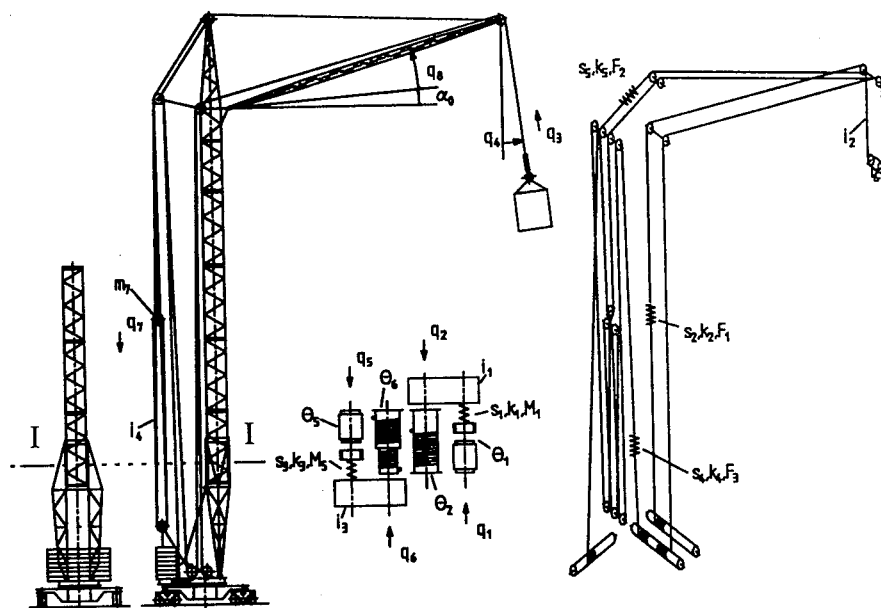


Fig. 1. Tower crane structure

that can be used for load or stress calculation in all the 8 rods 'cut' by that plane of truncation.

Since we need the loads and stresses in structure as the functions of time, this fact requires the application of *dynamic modelling and mathematical simulation methods*.

Description of combined crane motions requires complicated dynamic models and due to coincidence of straight-line and slewing motions it is necessary to count with the developing of centrifugal and Coriolis forces, too, that makes difficult the drafting of equations of motions for such systems.

For investigation of dynamic behaviour of tower cranes we have developed 3 dynamic models: one for analysis of stability [1], [2], [3], one for calculation of support forces [4], [5], and another one for determination of loads and stresses in the mast structure [6], [7], [8].

By the aid of the third model mentioned the effect of simultaneous start and braking of lifting, travelling and slewing motions can be simulated, or the same can be done with some time delay, or so can be simulated the independent start of each of them, the start of lifting motion with slacken rope, or the sudden release (dropping) of the lifted load.

A variation of these dynamic models can be seen in Fig. 3, which was elaborated and is used for studying the effect of combined raising, travelling

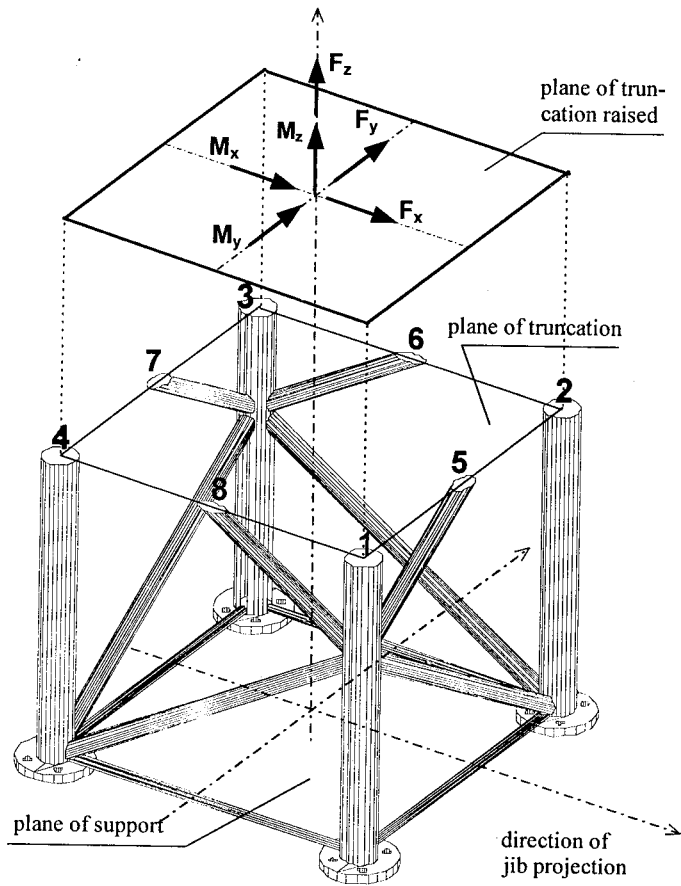


Fig. 2. Forces and moments in the cutting plane

and slewing motions.

Our model, used for investigation of the effect of combined motions on the mast structure, has 14 degrees of freedom, among which the mast itself has 3 degrees: two against bending (in its two main vertical planes) and one against torsional action around its longitudinal axis.

In these models the generalised co-ordinates are:  $q_1, q_8, q_{13}, q_{14}$  – the angular displacements of the axes of driving motors for slewing, lifting, travelling and luffing motions, respectively,  $q_2$  – the angular displacement of rotating table,  $q_3$  – the torsional deformation of the mast around its main (vertical) axis,  $q_6$  and  $q_7$  – the bending deformations of the mast under horizontal forces measured on the level of jib hinge point in the direction of the jib ( $q_6$ ) and perpendicularly to the jib ( $q_7$ ),  $q_{12}$  – the vertical displacement of the moving block of the luffing rope system (behind the mast, and having

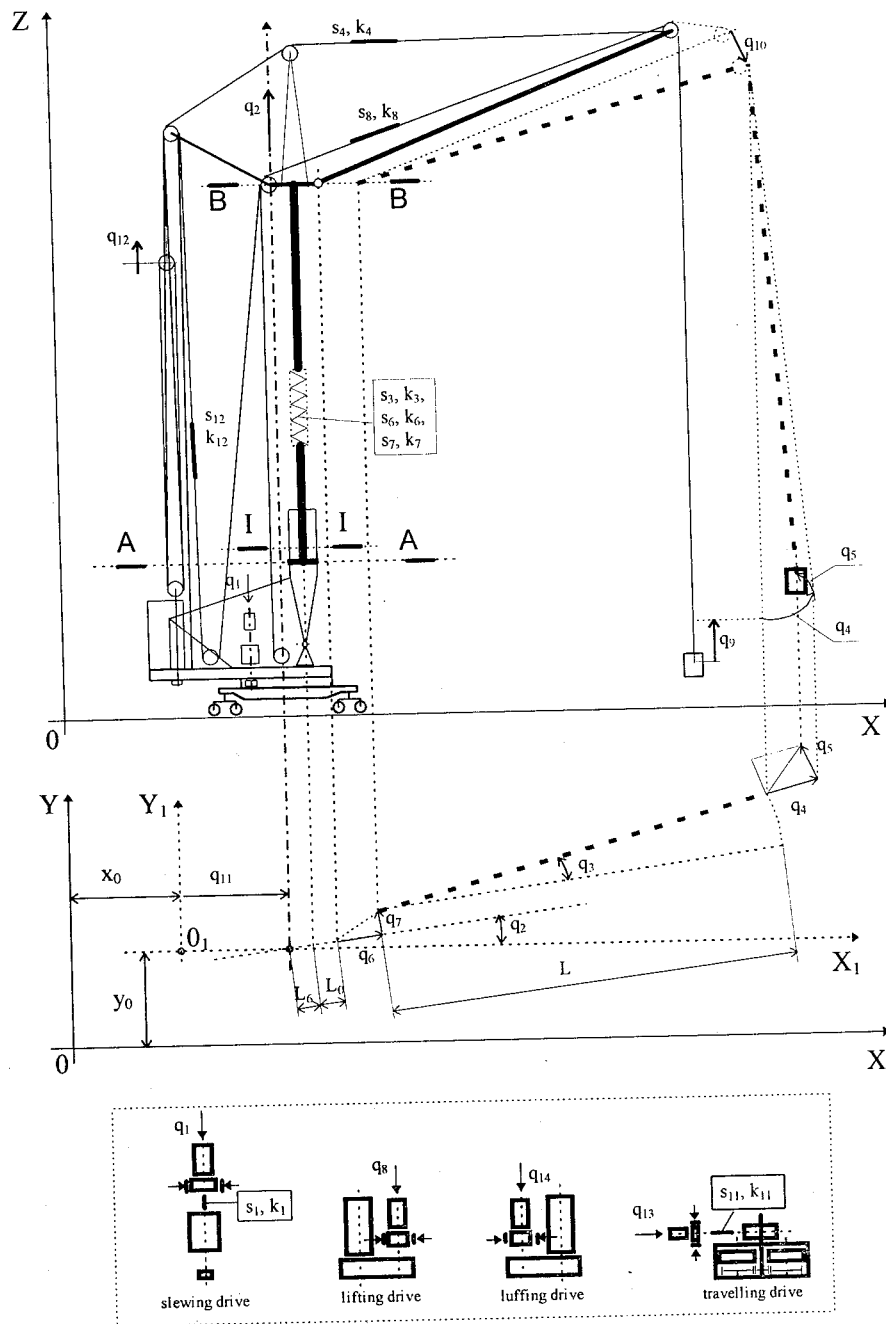


Fig. 3. Dynamic model variations

a mass  $m_1$ ),  $q_{10}$  – the displacement of the jib outside end (due to relative rotation around its hinge point),  $q_{11}$  – the horizontal motion of the whole crane on its track,  $q_4$  and  $q_5$  – the horizontal displacements of the load in the direction of jib projection and perpendicularly to it,  $q_9$  – the displacement of the load in the direction of the lifting rope.

The load lifting, jib holding and luffing rope system (*Fig. 1*), which is considered elastic, plays determining role in the loading of the mast. This system of ropes with different elasticity and the spatial pendulum motion of the load make the dynamic model rather difficult.

For checking of the quality of these models it was necessary to make a complex measuring experiment which was carried out on a real crane in 1995 (*Fig. 4*). Some results will be shown below.

## 2. Experimental Investigation for Elasticity and Damping Parameters

The rigidity of an elastic member is nothing else than the ratio of an action to the deformation caused by this action: N/m or Nm/rad, depending on the kind of action (force or moment) and on the deformation caused (elongation, deflection, torsion, etc.). The rigidity of simple elements can be determined by the equations of basic statics, but the same in case of girders with compound and varying cross-sections require instrumental static measurements. Determination of damping characteristics of structures requires exclusively oscillatory measurements, and the damping constants can be determined from the diagrams of free damped oscillations and on the basis of so-called logarithmic decrement.

It is known by specialists that to carry out an instrumental measurement and to evaluate the registrations is a rather difficult and responsible task, which is definitely true for an equipment with big geometric measures, especially if it is to be experimented at a construction site.

In the field experiment we have measured the quantities listed below:

- the displacements of different points of the structure under different static loads (to determine the deformations), using theodolits,
- the support forces under a whole rotation of the crane, using ring type load cells,
- the 6 loading vectors in the cross-section  $I - I$  of the mast (*Fig. 2*), using a specially developed strain gauge system,
- the force in the lifting rope, using a load cell,
- the oscillations on the load, on the outside end of the jib (in 3 directions), in cross-sections of the mast at different levels (with 4 accelerometers in a cross-section in two horizontal directions to measure the bending and torsional oscillations of the mast),
- the vertical oscillations of the rotating platform and of the bogies.

During this experiment the crane was subjected to the possible most extreme static and dynamic load tests: to sudden pull-up of the load (raising at slacken rope), to raising the load from suspended position, to starting and braking of the raising, travelling and slewing motions at the same time, to action of sudden release of the load rope from pulling force at vertical and inclined directions (imitation of dropping of the load). In the last case the rope inclination was arranged perpendicularly to the jib horizontal projection to cause a mast torsional deformation.

It is not possible in this paper to describe this experiment wholly, nevertheless it will be shown that the dynamic models and their system equations and mathematical algorithms we have elaborated are workable and suitable for solving the problems aimed for the analysis of loads and stresses of the mast.

### 3. Some Experimental and Simulation Results

As it was mentioned above, the loads in the mast cross-section  $I - I$  (Fig. 1 and Fig. 2) were experimented by a system of strain gauges, and the same system of 6 cross-sectional vectors for the same crane were determined by mathematical simulation, too.

The mathematical simulation provides us with the time functions of these vectors that makes it possible to create the *load- or stress-time-histories* for different loading and operating conditions of the crane.

The *simulated stress-time-histories* can be seen in Fig. 5 for the corner bar 4 ( $\sigma_4$ ) and for the lattice bar 6 ( $\sigma_6$ ). The simulation cases are: raising the load ( $R$ ), travelling motion with the jib, standing in the direction of the crane track ( $T$ ), slewing motion ( $S$ ), and the simultaneous raising, travelling and slewing motions ( $R + T + S$ ), all with the nominal load and with the simulation time of 20 seconds in every case. The diagrams are plotted at the same rate (0 ... -85 MPa for  $\sigma_4$  and 90 ... -70 MPa for  $\sigma_6$ ) for different working conditions, that provides an easy visual comparison.

The analysis of these diagrams makes us possible to draw conclusions listed below:

1. In the developing of dynamic forces, in excess of static ones, the slewing motion of the crane plays the determining role. The dynamic effects of lifting and travelling motions can nearly be neglected in the stress analysis.
2. The extreme values of stresses are developing always during the first 3 - 4 seconds following the start of the crane operations, that is important for the duration of simulation time.
3. Three dominant frequencies of oscillations can be observed in the stress-time diagrams. One of them has a relatively long period of time and big amplitude which is clearly determined by the length of load

rope suspended from the jib end (at the length of 40 m  $f_1 = 0.08$  Hz,  $T_1 = 13$  s). The other two components have higher frequencies – one for the corner bars depending on the bending elasticity of the mast ( $f_2 = 0.69$  Hz,  $T_2 = 1.45$  s), and the other one for the lattice bars depending on the torsional elasticity of the same mast ( $f_3 = 0.46$  Hz,  $T_3 = 2.2$  s).

4. With respect to varying of stresses it can be stated that for the corner bars the *pulsation of compressing stresses*, and for the lattice bars the *alternation of stresses* are characteristic. These circumstances are to be taken into consideration in checking the mast structure for the static strength and for the fatigue life, too.

Comparison of simulated and measured results is made on the basis of data in *Table 1* and *Table 2*.

Table 1.

The loading components	Units	Simulated values ( $S$ )	Measured values ( $M$ )	$\delta = \frac{M-T}{T} 100$ (%)
$\Delta F_x$	N	2117	1727	-18.4
$\Delta F_y$	N	3778	3785	0.18
$\Delta F_z$	kN	-387.5	-32.0	-17.4
$\Delta M_x$	kNm	94.6	108.6	14.8
$\Delta M_y$	kNm	118.6	128.4	8.3
$\Delta M_z$	kNm	98.0	105.0	7.14

Table 2.

The loading components	The eigenfrequencies (Hz)		$\delta = \frac{M-S}{S} 100$ (%)
	Simulated ( $S$ )	Measured ( $M$ )	
$\Delta F_x$	0.727	0.746	2.6
$\Delta F_y$	0.441	0.417	-5.4
	1.073	0.977	8.9
$\Delta F_z$	1.980	1.800	9.1
$\Delta M_x$	0.438	0.417	-4.8
	1.073	0.977	-8.9
$\Delta M_y$	0.732	0.708	-3.3
$\Delta M_z$	0.074	0.134	81.1
	0.438	0.422	-3.7

In *Table 1* and *Table 2* are quoted the simulated ( $S$ ) and measured ( $M$ ) quantities of components of the cross-section vector  $\mathbf{F}$ , namely:

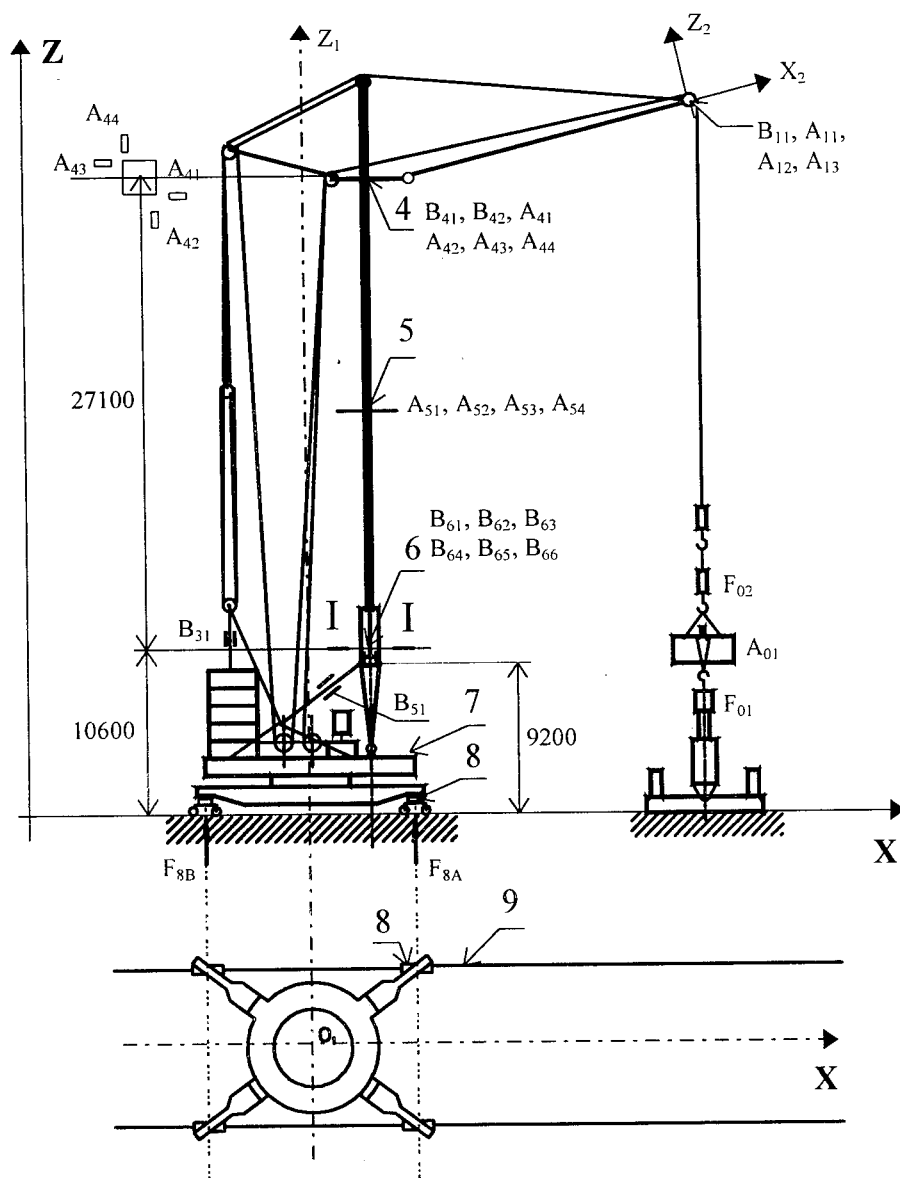


Fig. 4. Experimental crane model



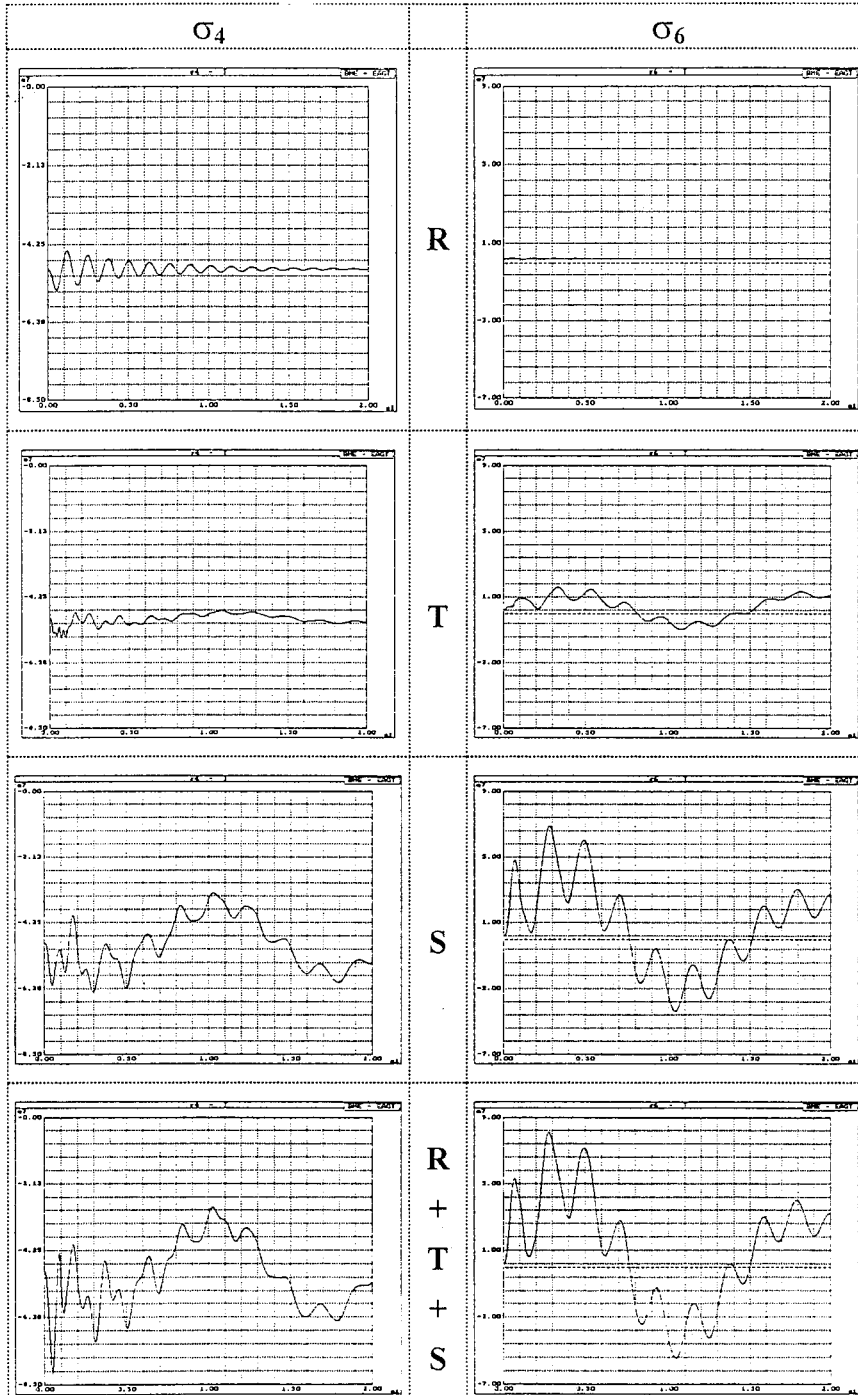


Fig. 5. Simulated stress-time histories

- in *Table 1* – the differences of static quantities ( $\Delta \mathbf{F}_x$ ,  $\Delta \mathbf{F}_y$ , etc.), which are developed in the structure due to the action of inclined prestressing rope force and after releasing of it,
- in *Table 2* – the characteristic frequencies of free oscillations developed in the structure after sudden release of that prestressing force, which were simulated or measured on the same components of cross-section vector  $\mathbf{F}$ .

The prestressing rope forces in both simulations and measurements correspond to the static action of the rated load.

The comparison of these data seems to be convincing on the quality and acceptability of the models and simulation software developed and presented here for the dynamic analysis of the lattice type mast of a tower crane with rotating tower.

#### 4. Conclusions

The dynamic model discussed and the simulation software developed at the Department of Building and Materials Handling Machines of T.U.B. is suitable for revealing the loading and stresses in the mast structure of the tower cranes more precisely than ever before, and the possibility of creation of simulated stress-time-histories opens the way of checking the crane mast structure for fatigue life time.

Furthermore, the dynamic simulation, by giving the displacements, velocities, accelerations and loads of the structure as the functions of time, provides a better understanding and more accurate describing of tasks that are directed to the effective damping of oscillations and to the development of automated driving and braking systems.

The experiences obtained can be transplanted without any difficulties to loading and stress analysis of frame structures of the tower cranes with non-rotating tower or of the portal cranes, too.

#### References

- [1] PRISTYÁK, A.: Gémes daruk állékonyságának elemzése (Analysis of Stability of Jib Type Cranes, in Hungarian). *Gép*, XXXIX: évf. 1987/12, pp. 445–450.
- [2] TRÂN QUANG QUI (1989): Toronydaruk állékonyságának elméleti elemzése. Kandidátusi disszertáció, BME-ÉÁGT, (Theoretical Analysis of Stability of Tower Cranes. PhD dissertation, in Hungarian. T.U. Budapest. Scientific Consultant: A. Pristyák).
- [3] PRISTYÁK, A.: Emelőgépek (munkagépek) állékonyságáról (On the Stability of Lifting Machines, in Hungarian). *Gép*, XLIII. 1991/7–8–9, pp. 236–242.
- [4] PRISTYÁK, A. – VONHAUSER, O.: Gémes forgódaruk támaszerőinek vizsgálata (Analysis of Support Forces of Jib Type Cranes, in Hungarian). *Géptervezők IX. Országos Szemináriuma Előadásai*, Miskolc, 1993. IX. 30 –X. 1., pp. 110–114.

- [5] VONHAUSER, O. (1996): Forgódaruk támaszerőinek dinamikai vizsgálata. Egyetemi doktori disszertáció, BME-ÉÁGT, (Dynamic Analysis of Support Forces of Slewing Cranes. University dissertation, in Hungarian. T.U.Budapest. Scientific consultant: A. Pristyák).
- [6] PRISTYÁK, A. – NGUYEN VAN VINH: Gémes forgódaruk rácsos oszlopszerkezetének feszültségelemzése. (Analysis of Stresses in the Mast Struture of Jib Type Slewing Cranes. In Hungarian.) *Gép*, XLVII. 1996/VII, pp. 20–22.
- [7] PRISTYÁK, A. – NGUYEN VAN VINH: Analysis of Mechanical Oscillations and Stresses in the Mast Structure of a Tower Crane. *The VIII-th Conf. on Mechanical Vibrations*. T. U. Timișoara, 28–30. Nov. 1996. Vol. II, pp. 11–16.
- [8] NGUYEN VAN VINH (1997): Forgóoszlopos toronydaruk oszlopszerkezetének igénybevételi vizsgálata. Kandidátusi disszertáció, BME-ÉÁGT, (Investigation of Loads of the Mast of a Tower Crane. PhD dissertation, in Hungarian. T. U. Budapest. Scientific Consultant: A. Pristyák).



## INDEX

ZOBORY, I. – ZOLLER, V.: Track-vehicle in-plane Dynamical Model Consisting of a Beam and Lumped Parameter Components . . . . .	3
SOUMELIDIS, A. – GÁSPÁR, P. – BOKOR, P.: An Inverted Pendulum Tool for Teaching Linear Optimal and Model Based Control . . . . .	9
CANFES, Ö, E. – UYSAL, A.: Quasi-Recurrent Weyl Spaces . . . . .	21
PAP, G.: On the Transient Behaviour of Controlled Propulsion Plants . . . . .	27
ZOBORY, I. – BÉKEFI, E.: On Simulation of Operation Conditions of Running Gears in the Period of Design . . . . .	45
MÁRIALIGETI, J.: Simulation Study of the Influence of Involute Tip Relief on Gear Dynamic Behaviour . . . . .	59
SZÓKE, D.: Non-linear System and Modal Analysis . . . . .	79
KUTI, I.: Non-Linear Dynamic Analysis of Vehicles Using Large Finite Element Models . . . . .	85
PRISTYÁK, A.: Analysis of Dynamic Loads of the Lattice Type Mast Structure of a Tower Crane Using Simulation Method . . . . .	103



## INFORMATION FOR AUTHORS

**Submitting a Manuscript for Publication.** Submission of a paper to this journal implies that it represents original work previously not published elsewhere, and that it is not being considered elsewhere for publication. If accepted for publication, the copyright is passed to the publisher: the paper must not be published elsewhere in the same form, in any language, without written consent of the executive editor. The first author will receive 50 free reprints.

Manuscripts should be submitted in English in two copies to the editors' office (see inner front cover). Good office duplicated copies of the text are acceptable.

*Periodica Polytechnica* is typeset using the TEX program with the AMSTEX macro package. Therefore, authors are encouraged to submit their contribution after acceptance in this form too, or at least the text of the article in a simple ASCII file (e. g. via email or on a floppy diskette, readable on an IBM compatible PC). By this solution most of the typesetting errors can be avoided, and publishing time can be reduced. An AMSTEX style file with a sample TEX source file is also available upon request.

**Compilation and Typing of Manuscripts.** Contributions should be typed or printed in double spacing (24 pt spacing when using text processors), on A4 paper. One page may contain not more than 10 corrections (prints do not count).

The maximum length of the manuscript is 30 standard pages (25 lines, with 50 characters in a line), including illustrations and tables. When more characters are typed on a page, the allowed page number is reduced accordingly.

When using a text processor, please use a (preferably English) spelling checker before the final printing.

Use one side of the sheet only. Paragraphs are to be indented by 5 spaces and not to be preceded by a blank line.

A correctly compiled manuscript should contain the following items:

- (1) Title page giving: the suggested running header (max. 50 characters) for the odd typeset pages; the title (short, with subheading if necessary); the name(s) of the author(s); affiliation (institution, firm etc.) of the author(s), in English, with mailing address, telefax and phone numbers and email address; grants, scholarships etc. during the research (in a footnote); an informative abstract of not more than 200 words with 3-5 keywords;
- (2) Textual part of the contribution with a list of references;
- (3) A separate sheet listing all figure captions and table headers;
- (4) Illustrations and tables (please put your name on each sheet), at least one set of illustrations in very good quality for reproduction.

**Abstract.** A summary or abstract of about 100-200 words should be provided on the title page. This should be readable without reference to the article or to the list of references, and should indicate the scope of the contribution, including the main conclusions and essential original content.

Keywords are to be given for the purpose of data bases and abstracting; avoid too general keywords which provide no help in literature searching.

**General rules for the text.** Chapters are to be numbered with Arabic numbers in decimal hierarchy.

Wherever possible, mathematical equations should be typewritten, with subscripts and superscripts clearly shown. Metric (SI) units are to be used, other units may be given in parentheses. Equations must be numbered on the right side, in parentheses. Handwritten or rare mathematical, Greek and other symbols should be identified or even explained if necessary in the margin. Letters denoting quantities are to be distinguished by different setting both in the formulae and in the text. Remember the rule that scalar quantities are to be denoted by italics (underline by hand in your manuscript), vectors by lower case bold type letters (underline doubled), and matrices by bold capitals (underline doubled). Dimensions (like cm, Ohm, V etc.) and standard function names (sin, ln, P etc.) are to be typeset in Roman typefaces (not in italics). A few important words may be distinguished by italic setting (underline).

**Illustrations and Tables.** Graphs, charts and other line illustrations should be drawn neatly in Indian ink, or printed by a laser printer. Computer printouts can only be used if they are of excellent quality. Figures should be submitted in an adequate size for camera-ready pages in size 1.2:1. Suggested line thicknesses: 0.18-0.35-0.4 mm or 0.5-0.7-1.14 pt. Letter sizes: 0.4 mm (10 pt). All figures should be numbered with consecutive Arabic numbers, have descriptive captions, and be referred to in the text. Captions should be self-explanatory, not merely labels. Figures must not contain lengthy texts; use captions instead.

Number tables consecutively with Arabic numbers and give each a descriptive caption at the top. If possible avoid vertical rules in tables. Tables should be preferably submitted in camera-ready form.

The earliest acceptable position of figures and tables is to be indicated in the left margin.

**References.** In the text references should be made by the author's surname and year of publication in parentheses, e.g. (Earl et al, 1988) or ...was given by Kiss and Small (1986a). Where more than one publication by an author in one year is referred to, the year should be followed by a suffix letter (1986a, 1986b etc.), the same suffix being given in the reference list. For the style of the reference list, which is to be given in alphabetical order, see the examples below for journal articles, conference papers and books.

Earl, J., Kis, I. and Török, I. (1988): Partial Discharge Measurement in Cables. *Periodica Polytechnica Ser. Electrical Engineering*, Vol. 32, No. 4, pp. 133-138.

Kiss, S. and Small, A. B. (1986a): Roundoff Errors in FFT. *Proc. 5th IEEE Symposium on Signal Processing*, Boston (MA), May 3-5, 1986. New York, NY, IEEE Press, CH0092-2875/86, pp. 3.5-3.9.

Kiss, S. and Small, A. B. (1986b): Ellenállások (Resistances). Budapest, Tankönyvkiadó. pp. 533-535. (in Hungarian)

More detailed guidelines for authors, with hints for the preparation of figures and with a sample page, are available from the editors' office (see inner front cover).

## CONTENTS

ZOBORY, I. – ZOLLER, V.: Track-vehicle in-plane Dynamical Model Consisting of a Beam and Lumped Parameter Components . . . . .	3
SOUHELIDIS, A. – GÁSPÁR, P. – BOKOR, P.: An Inverted Pendulum Tool for Teaching Linear Optimal and Model Based Control . . . . .	9
CANFES, Ö, E. – UYSAL, A.: Quasi-Recurrent Weyl Spaces	21
PAP, G.: On the Transient Behaviour of Controlled Propulsion Plants . . . . .	27
ZOBORY, I. – BÉKEFI, E.: On Simulation of Operation Conditions of Running Gears in the Period of Design	45
MÁRIALIGETI, J.: Simulation Study of the Influence of Involute Tip Relief on Gear Dynamic Behaviour . . . .	59
SZÖKE, D.: Non-linear System and Modal Analysis . . . .	79
KUTI, I.: Non-Linear Dynamic Analysis of Vehicles Using Large Finite Element Models . . . . .	85
PRISTYÁK, A.: Analysis of Dynamic Loads of the Lattice Type Mast Structure of a Tower Crane Using Simulation Method . . . . .	103